Development of Directional Detector System for Localisation in Mixed Field Environments

George Luke Randall

A dissertation submitted in partial fulfillment

of the requirements for the degree of

Doctor of Philosophy

of

University College London.

Department of Medical Physics and Biomedical Engineering

University College London

April 25, 2017

I, George Luke Randall, confirm that the work presented in this thesis is my own. Where information has been derived from other sources, I confirm that this has been indicated in the work.

Abstract

Active interrogation is a method of detecting fissionable materials by directing radiation, normally high energy photons or neutrons, at a volume of interest. The resulting fission events can produce a unique signature in the form of delayed neutrons and gammas that can be used to identify a material. A common application of this technique is in the detection of special nuclear materials (SNMs) such as ^{235}U. A requirement has been identified to provide a directional detector for use in one of these high flux active interrogation environments.

Many detectors of ionising radiation exist but few are capable of directionality. Those that are tend to be heavy and inefficient. A novel method for providing directionality for radiation detection, previously developed by the author, is to be used - the RadICAL detector [1]. The idea is based upon the fact that detector response depends upon the radiation pathlength and area presented to a particle flux. Thus a rotating slab of detector gives a characteristic temporal response that can be used to identify the direction of the photon flux. This concept is to be used to locate fast neutrons produced by a material of interest within an active interrogation scenario.

The first objective of this study was to model a RadICAL detector. The original model was built using a simple ray tracing method and this was followed by the construction of a more complicated Geant4 Monte-Carlo model. The results of this modelling were used to inform decisions made in the building of a prototype detector. Further modelling was conducted to investigate the optical properties of the detector.

The second objective was to design and build a number of these detectors based on this modelling. These detectors were then tested by exposing them to a number of different sources under a variety of different conditions and evaluating the response.

The third objective was to develop a detector capable of determining the direction of an active interrogation source. This involved a variation on the RadICAL method,

the RadICAL Stack, whereby counts from a stack of stationary detectors were fitted to a standard response curve in order to determine the direction of the source. The detectors were built from Eljen EJ299-33 so that the localisation technique could be combined with pulse shape discrimination techniques to separately determine the location of gamma and neutron sources.

Both the RadICAL and the RadICAL Stack detection methods were shown to be effective at determining the direction of a gamma source. A four element detector was built and shown to achieve an angular resolution of approximately $4.4 \pm 0.3^\circ$ when detecting a 3.7 MBq ^{137}Cs source at distances up to 2.1m. The same detector was shown to achieve an angular resolution of approximately $2.95 \pm 0.32^\circ$ when detecting discriminated neutrons from a 150 MBq ^{252}Cf source at distances of up to 4m.

Acknowledgements

I would like to thank everyone who has made this possible. Firstly I would like to thank my supervisor Prof. Robert Speller not just for all of the support, guidance and encouragement throughout the course of my PhD but also for the infectious enthusiasm, friendship and faith that I've been shown that has made such a difference to my life since I first arrived at UCL. Special thanks also go to Nick Calvert for all of the time spent helping me get to grips with Geant4 coding.

I'd like to thank AWE plc for their contribution and support and everybody involved in the collaboration including Kirk Duroe, Mark Ellis, Mark Owen and Neil Gaspar at AWE, Prof. Malcolm Joyce and Ashley Jones at Lancaster University, Prof. Paul Sellin and Chris Payne at Surrey University and Lee Packer at CCFE. I'd also like to thank David Thomas for all of the help with our experiments at NPL. Also Laura Harkness-Brennan at the University of Liverpool and Kirk Atkinson at the Defence Academy deserve a special mention for all of the support and patience in recent months.

Having so many good friends at UCL has meant that I looked forward to coming to work every day and added so much to my experience throughout the course of my PhD. I've made so many lasting friendships and been offered so much practical support from such a wide range of people at UCL that I'm reluctant to include names for fear of missing somebody. A few people deserve a special mention though:

- Tom Millard - Not just for giving up your Sunday to help me with LabVIEW but for agreeing to go along with all of my stupid ideas. From weekly runs and numerous caving trips and a successful attempt at the Three Peaks Challenge to less successful attempts at walking around the Capital Ring and the Isle of Wight in 24 hours. I'm looking forward to the next one!

- Dan O'Flynn - For laughing at the jokes that nobody else does and for constantly surprising me with pictures of Marky Mark and Crocodile Dundee.

- Yi Zheng - For being a constant ray of sunshine from the first day of my MSc until the end of my time at UCL and beyond.

- Nik Vassiljev - For leading me astray with numerous beers and games of pool and for dealing with tough times with inspiring bullishness and positivity. Keep fighting Nik - I'm looking forward to you showing me around St Petersburg!

I'd also specially like to thank Claire Marinier for all of the support, patience and understanding over the last year. I think you may be the one person looking forward to me submitting this more than I am!

Finally I'd like to thank my Family. My parents for their unwavering encouragement and support throughout my whole life and especially over the last few years. To Will, Raphi and little Dorothy and to Emily for being an excellent flatmate throughout my PhD and for encouraging me, more than anyone, to have the faith in myself to quit a miserable job and try something new. Maybe bossy big sisters aren't so bad after all!

Contents

List of Figures

List of Tables

Chapter 1

Introduction

1.1 Introduction

This thesis presents work undertaken to develop new methods of detection of Special Nuclear Materials (SNMs). This work is sponsored by AWE and is based on a key project objective to provide a neutron/gamma detection system that is optimised for use in very high flux active interrogation experiments and is a collaboration between University College London, The University of Surrey and Lancaster University.

An urgent need has been identified to improve the reliability of screening cargo containers for illicit nuclear material that may be hidden there for terrorist purposes [2]. Radiation portal monitors and other passive detection devices have been used successfully for many years [3] to screen for gamma, and neutron emitting sources but are limited by the available passive emissions from SNMs such as ^{235}U, ^{233}U or ^{239}Pu which generally produce low energy decay products. In the case of ^{235}U the main, detectable, decay product is 186 keV photons that can be easily shielded by any reasonably high Z materials [4]. This represents one of the greatest current obstacles within the field of SNM interdiction [5].

The collaborative project, proposed by AWE, was to develop a neutron/gamma discriminating detector and readout system optimised for high flux active interrogation. The detector to be used was EJ299, a polyvinyltoluene (PVT) based scintillator [6] developed by Los Alamos for neutron discrimination. The detector was to function in a very high flux mixed field environment and so a gating system was proposed, incorporating a fast silicon PIN diode as a trigger detector, in which the EJ299 detector could be 'blanked' during the intense interrogation pulse and prompt response and then

reactivated during the subsequent delayed response. The time and duration of this 'blank' phase was to be dynamically sensed by the trigger detector. Finally the detector should have 'imaging' capability and be able to locate a source of fission products to a single, 30cm^3, voxel within an interrogation volume.

Within this collaboration the University of Surrey were primarily responsible for determining the optimum detector geometry, as well as acquiring and cutting the plastic scintillator and coupling it to the photomultipliers. UCL were responsible for developing the imaging techniques and incorporating these into the detector design. Lancaster University were responsible for developing the gating system.

1.2 Nuclear Material Security

Since the discovery of nuclear energy, steps have been taken to protect people, both workers and the general public, from the effects of dangerous radiation. Concerns about non-proliferation have been ongoing since the first use of nuclear weapons and throughout the subsequent arms race.

Since the terrorist attacks in the United States on the 11th of September 2001 and similar events in London, Madrid and Paris, fears were increased that nuclear material could be used for malicious purposes in the form of a nuclear weapon or a radioactive dispersal device, a 'dirty bomb' [7].

1.2.1 Nuclear Materials of Concern

The materials of concern, as defined by the Unites States Nuclear Regulatory Commission, can be divided into three main categories: [8]

1.2.1.1 Source Material

Source material is defined as uranium, thorium, or any ores containing sufficient concentration to be of concern (more than 0.05 percent of uranium or thorium, or any combination thereof) [9] [10]. This definition includes depleted uranium left over from enrichment [8]. Whilst this material is not usable in weapons it may be transmuted by neutron irradiation and the products separated chemically or enriched to create material suitable for weapons [11]. Due to the large quantities of source material, technology, time and expertise required for these processes this material is considered less of a concern and so less stringent safeguards are applied.

1.2.1.2 Special Nuclear Material

The Nuclear Regulatory Commission of the United States defines special nuclear material, in the Atomic Energy Act of 1954, as plutonium or uranium enriched in the isotope 233 (to more than 12%) or the isotope 235 (to more than 20%). The definition also includes any other material capable of releasing substantial amounts of atomic energy, not including source material, deemed to be important by the Commission [9]. Under proper conditions these materials can undergo a self sustaining fission reaction with the release of considerable energy. The World Nuclear Association defines Weapons Grade Uranium as relatively pure Highly Enriched Uranium ($>$90% ^{235}U) and Weapons Grade Plutonium as ^{239}Pu containing relatively small amounts of other plutonium isotopes ($<$8% ^{240}Pu) [12]. In practice it is possible to make a nuclear weapon using less pure nuclear material, although this would require a much higher level of technical skill [11]. Due to the catastrophic human and economic ramifications of a nuclear attack these materials are of the greatest concern from a safeguards point of view [13].

1.2.1.3 Byproduct Material

Byproduct material refers to any radioactive material (except special nuclear material) that is produced, or made radioactive, in a nuclear reactor. It can also include the waste produced by extracting or concentrating uranium or thorium from an ore processed primarily for its source material content [9].

These materials are, in general, highly radioactive and any malevolent use would be in the form of a radiation dispersal device [14]. Likely sources that could be used for this purpose are: cobalt-60, strontium-90, caesium-137, iridium-192, radium-226, plutonium-238, americium-241, and californium-252 [14]. Material of this type include spent nuclear fuel, medical sources, industrial radiography and gauging devices, food sterilisers and sources used in research laboratories [14]. Sources of this type are always packaged, transported and processed in heavily shielded containers and this, combined with the danger of handling such substances and the stringent safeguards applied, make their acquisition by potential adversaries difficult[11].

1.2.2 Production of Special Nuclear Material

1.2.2.1 Uranium-235

^{235}U is the only fissile nuclide that is found in any significant quantity in nature [15]. It is part of 'natural uranium' along with a number of different isotopes. Natural uranium occurs relatively commonly in nature but only a small proportion of this is ^{235}U and so it needs to be enriched before it can be of any practical use or of concern for nuclear safeguards [16].

Uranium is mined and milled to produce uranium-oxide concentrate with a proportion of around 0.7% ^{235}U, traces of ^{234}U and a proportion of ^{238}U. This uranium oxide is then converted, using a series of chemical processes to a gas UF_6. This gas can then be separated by isotope in a centrifuge or by passing it through a microscopic membrane. Both of these processes are inefficient and require many passes for substantial enrichment. The enriched gas is then converted to UO_2 which can subsequently be used to form fuel elements [17].

Table 1.1 [18]shows a summary of the nuclear enrichment facilities currently in operation worldwide. These include a combination of centrifuge and diffusion plants. The capacity of each plant is given in Metric Ton Separative Work Units (MTSWU = 1000SWU) which describes the amount of separation done by the enrichment process. This is a complex unit that depends upon both the percentage of ^{235}U that is desired in the enriched stream and how much of the ^{235}U in the feed material ends up in the depleted uranium stream [19]. This data is based on voluntary reports from IAEA (International Atomic Energy Agency) member states and so can not be considered to be an exhaustive list of enrichment facilities [18].

^{235}U is a component of most commonly used nuclear fuel and has been used in many nuclear weapons including 'Little Boy', which was dropped on Hiroshima in 1945 [20].

1.2.2.2 Uranium-233

^{233}U does not occur in any significant quantities in nature but can be bred from ^{232}Th as part of the thorium fuel cycle. Thorium is naturally occurring but, unlike Uranium, it contains only one isotope ^{232}Th. This can be used to produce ^{233}U by the absorption of a neutron and subsequent disintegration. Neutron capture in ^{232}Th results in short

lived ^{233}Th which decays rapidly to ^{233}Pa and subsequently to ^{233}U.

^{233}U based fuel is less commonly used but has a number of potential advantages including: increasing resources, reducing enrichment requirements and decreasing production of plutonium and other transuranic elements [21].

Country	Facility Name	Scale	Design Capacity (MTSWU/year)
Argentina	Pilcaniyeu Enrichment Facility	Pilot plant	20
Brazil	Aerospace Technical Center	Laboratory	0
Brazil	BRF Enrichment	Pilot plant	4
Brazil	BRN Enrichment	Laboratory	5
China	Lanzhou 2	Commercial	500
China	Shaanxi Uranium Enrichment Plant	Commercial	1000
France	Georges Besse II	Commercial	7500
Germany	Enrichment Technology Company Ltd.	Laboratory	0
Germany	Urenco Germany GmbH	Commercial	4500
Japan	Rokkasho Uranium Enrichment Plant	Commercial	1050
Netherlands	Urenco Nederland	Commercial	4500
Pakistan	Kahuta	Commercial	5
Russia	Angarsk	Commercial	1000
Russia	Ekaterinburg (Sverdlovsk-44)	Commercial	0
Russia	Krasnoyarsk	Commercial	0
Russia	Siberian Chemical Combine (Seversk)	Commercial	4000
UK	Urenco UK Ltd	Commercial	4000
USA	Paducah Gaseous Diffusion	Commercial	11300
USA	Urenco USA	Commercial	3000

Table 1.1: Uranium Enrichment Facilities Currently in Operation Worldwide ©IEEE 2012.

1.2.2.3 Plutonium

Plutonium only occurs in extremely minute quantities in nature - in uranium ores as a result of the capture, in U^{238}, of neutrons from spontaneous fission and alpha-neutron reactions. All significant quantities of plutonium are produced as a result of neutron capture in ^{238}U, and successive beta decays, within a nuclear reactor. Isotopes of ^{238}Pu, ^{239}Pu, ^{240}Pu, ^{241}Pu, ^{242}Pu and ^{243}Pu are all formed due to a combination of these reactions. The ratio of production of these isotopes varies greatly depending on the cross section of the various plutonium isotopes over the different neutron spectra. In a fast reactor the plutonium predominantly produced is ^{239}Pu so because of this, and due to its long half life of 24,360 years, ^{239}Pu is the most abundant isotope of plutonium [22].

Plutonium is widely used in nuclear weapons, such as the 'Fat Man' bomb dropped on Nagasaki in 1945 [20]. It is also used for power generation by mixing with uranium to form mixed-oxide fuel (MOX) [23].

1.2.3 Security of Special Nuclear Material

Illicit trafficking and smuggling of SNM occurs worldwide and reported incidents have increased in the years since the breakup of the Soviet Union. Particular concern has been paid to the threat that weapons usable material from former soviet countries, particularly Russia, could be stolen and fall into the hands of terrorists [24].

1.2.3.1 SNM Stockpiles by Type

A summary of existing stockpiles of SNM is given below and on the next page. This consists of voluntary information supplied to the IAEA by member states. Notable non signatories of the Nuclear Non-Proliferation Treaty (NPT) who are thought to possess nuclear weapons include: India, Pakistan, Israel and North Korea [25]. Data on SNM stockpiles is not available for these countries.

Uranium-235 Highly Enriched Uranium (HEU) forms the bulk of the worldwide stockpile of SNM. The military stockpile, held by acknowledged nuclear weapon states, consists of approximately 1331 tonnes of HEU. Most of this is held by Russia (712 tonnes) and the United States (544 tonnes). Smaller quantities are held by the United Kingdom, France and China. These exist in weapons, military reactors, production reactors, reserves and excesses [26].

Large civil stocks of HEU are also spread between the Nuclear Weapon States (NWS) and Non-Nuclear Weapons States (NNWS). An estimated 134 tonnes of HEU was present in civil stocks at the end of 2014. 118 tonnes of this is held by NWS and is mostly former military stock that has been rededicated. As of 2015 a total of 26 countries hold HEU stocks [27].

Uranium-233 Thorium based reactors have been built in the United States, Canada, Germany the United Kingdom and India but have not been used for large scale power generation or weapons. As a result ^{233}U stockpiles are small compared to those of ^{235}U or plutonium [28].

About 2 tons of ^{233}U was produced by the United States, mostly in the 60s and 70s as part of its civilian and military nuclear programs. Specific estimates of the amount

of this material currently in storage vary widely [29]. This suggests that current control of this material requires attention and that up to 96kg of ^{233}U may be unaccounted for [29].

Plutonium An estimated 238 tonnes of plutonium is currently held by acknowledged nuclear weapon states. As with HEU most of this is held by the United States and Russia, with smaller quantities held by China, France and the United Kingdom. Of this total approximately 127 tonnes is military stock and the remaining 111 tonnes is declared excess [26].

Civil stocks of plutonium exist in irradiated and un-irradiated forms. Of these forms, the un-irradiated plutonium is considered to be of most concern from a proliferation standpoint [30]. A total of approximately 275 tonnes of this material is currently held in civil stocks. The United Kingdom, France and Russia currently hold the greatest proportions of the civil stock of this material with further stocks held by Germany, India, Belgium, China, Japan, The Netherlands and Switzerland [30].

1.2.3.2 Illicit Trafficking and Smuggling Incidents

The IAEA Incident and Trafficking Database (IATB) was established in 1995 to record and analyse incidents of illicit trafficking in nuclear and other radioactive material. Reporting to the IATB is voluntary and is made by 131 current member states. Between 1993 and the end of 2014 a total of 2734 confirmed incidents were made by participating states. These include 442 cases of unauthorised possession, 714 cases of theft or loss and 1526 incidents involving other unauthorised activities or events [31].

A small proportion of these incidents involved quantities of SNM. These include 0.4kg of plutonium seized by undercover police from a suitcase at Munich Airport in August 1994 and in December of the same year 2.7kg of stolen HEU from an individual in Prague [32]. A further 18 similar incidents, involving weapons usable materials, were reported between 1992 and 2001 [24].

1.2.3.3 Nuclear Safeguards

The IAEA implements a comprehensive program aimed at stemming the threat of nuclear terrorism. This consists of: physical protection and regulation of nuclear materials, detection and interdiction of illicit trafficking in nuclear and radioactive materials, coordination of nuclear safety, security and safeguards systems and preparing responses

to likely emergencies [33].

A similar approach is implemented by the U.S. government with its first priority being to ensure that SNMs never fall into the hands of terrorists. Since the early 90s the United States have been working closely with the Russian government to help it secure the vast quantities of nuclear materials acquired under the Soviet Regime during the Cold War. Although the Soviet regime maintained good control over their nuclear weapons the wide distribution of materials has meant that keeping track of everything has been impossible. Given these difficulties a second line of defence has been implemented. This involves setting up detection measures at various points at border crossings in former Soviet countries and certain other Mediterranean and European nations [32]. Further measures include the 'Megaports Initiative', a US led collaboration to provide radiation detection systems to 100 different major ports, worldwide, by 2016 [34].

1.3 Passive Methods of Special Nuclear Material Detection

Radiation detection instrumentation is increasingly being deployed around the world to interdict the illegal shipment of radioactive materials at land, rail, air and sea ports of entry. A number of different detection methods are in current use, with further techniques under investigation [35].

Passive detection involves directly detecting the radiation signature of a threat object. These techniques are relatively simple and safer than active detection but are limited by the passive emission of the materials of interest [36].

1.3.1 Radiation Portal Monitors

Radiation portal monitoring (RPM) systems have existed for many years as a method of intercepting nuclear weapons, special nuclear materials and radiation dispersal device materials that could be used for the purpose of terrorism [3]. Since the attacks of September 11th 2001 the concern about such an attack has increased and the demand for these RPMs, and similar technology, has grown greatly [37]. These RPMs generally consist of panels of detectors that are positioned around an area of interest through which a person, vehicle or item of cargo is passed to screen for gamma, and neutron

emissions that can be used to identify materials of interest [36]. For gamma screening the commonly used detector materials are PVT based plastic scintillator and inorganic scintillator such as NaI(Tl) [36]. Plastic scintillator is the most commonly used detector for this purpose due to its low cost, and hence the ability to manufacture large panels, its durability and reduced sensitivity to radiation damage or gain drifts from radiation damage [3]. NaI detectors are more expensive than PVT but have energy resolution of around 6-7% [38] that enables isotopic identification and the rejection of false detections [3]. Semiconductors such as high purity germanium (HPGe) have also been investigated for the same purpose due to their high energy resolution but the cost, long measuring time and the practical problems associated with cooling the detectors make this an unusual choice [3]. Neutron detection is also desirable when passively screening for SNMs, particularly ^{240}Pu due to its high neutron emission rate [35]. Neutron detection has traditionally been conducted using ^3He but this has become problematic in recent years because of the dwindling supply of this material. This is partly due to a drastically increased demand for ^3He to be deployed in neutron detectors and other systems but it is also because of the way that it is produced. ^3He is a byproduct from the beta decay of tritium. The production of ^3He has declined with the reduction of the nuclear weapons stockpile and so investigations are being carried out into alternative methods of neutron detection [36] [39].

1.3.2 Cosmic Ray Muon Scattering Tomography

A further passive method of detection of SNM that has been investigated in recent years involves the detection of cosmic-ray muons. These are highly penetrating elementary charged particles produced naturally, and in large numbers, by the interactions of high energy cosmic ray nucleons with gases high in the atmosphere.

By tracking the scattering angles of individual particles it is possible to detect material with high atomic number, such as uranium, within a volume of less dense material. This method provides a relatively safe and inexpensive radiography technique for detecting dense materials [40].

More recently this technique has been combined with the knowledge that cosmic ray muons can interact with fissile material to produce detectable quantities of neutrons. By detecting these neutrons at the same time as tracking the muon paths it has been

shown that it is possible to verify the presence of fissile material within a volume [41].

1.4 Active Interrogation Methods for Detection of Special Nuclear Material

Active interrogation is a method of detecting specific materials of interest by directing nuclear radiation, normally high energy photons or neutrons, at a volume of interest. When bombarded by specific radiation various materials of interest may undergo fission events that will produce a unique signature in the form of prompt and delayed neutrons and gammas [42]. A common application of this technique is in the detection of special nuclear materials (SNMs) such as highly enriched uranium (^{235}U) [43]. The main benefit of this method of interrogation, compared to passive interrogation systems, is that the fission products are often high energy, up to around 6 MeV, and are therefore more effective at penetrating shielding materials than normal gamma emissions [5].

A large number of investigations [5][44][45][46][47] have been conducted into the relative benefits of different active interrogation sources and these were investigated for a number of detection scenarios using experimental and modelling techniques. A summary of the proposed source types, and reactions, is detailed below.

1.4.1 Detection Scenarios

Some of the most commonly investigated active interrogation methods involve passing a volume of interest, commonly a shipping container, through a portal similar to the RPMs described earlier. An interrogation source, in many cases in the form of a fan beam, is positioned either to the side of, or below the portal [2]. The type, and number, of detectors used in each case is determined by a number of factors including: the interrogation source, geometry of the setup, acquisition time and any specific imaging requirements.

Further scenarios [48][49][35] that have been investigated involve employing active interrogation techniques on-board ships whilst still at sea. This could potentially greatly reduce the time required to scan individual containers as they enter port and reduce the shielding requirements. It would also greatly reduce the danger to major population centres as well as economic and psychological damage incurred by the discovery of SNM by interdicting the material before it reaches port. Suggested techniques

involve portable equipment that could be used for a boarded search of a container vessel [49]. Further techniques investigated involve the scanning of entire small to medium vessels using ship mounted interrogation equipment [48].

1.4.2 Interrogation Sources

A number of different interrogation sources have been suggested and tested in order to produce a range of prompt and delayed photon and neutron signatures.

Direct comparison of performance characteristics for each system is difficult. This is due to the difficulty of transporting each, often large and complicated, system combined with the limited availability of the kilogram quantities of HEU needed for testing [50].

Each of these sources are described below and a summary is shown in Table 1.2.

Table 1.2: Summary of Active Interrogation Sources

Source		Energy (MeV)	Advantages	Disadvantages	Example Reference
Photon	Bremsstrahlung	2 - 20	High Output	High Background,	[42]
	Characteristic	6 - 18	Monoenergetic, Low Background,	Low Output, Poor Penetration of High Z Shielding	[45]
Neutron	Bremsstrahlung	0 - 10	Monoenergetic, High Output, Good Penetration of High Z Shielding	High Gamma Background, Poor Penetration of Hydrogenous Shielding	[41]
	Charged Particle Induced	0 - 5	Monoenergetic, Low background, High Output, Good Penetration of High Z Shielding	Poor Penetration of Hydrogenous shielding	[54]

1.4.2.1 Bremsstrahlung Photon Source

The ideal active interrogation photon source would involve sufficiently high energies to produce relatively high photofission signals but low enough to avoid the photoneutron threshold for common cargo materials that may cause unwanted background signal. These ideal energies would typically be between approximately 6 and 18 MeV [51].

The most commonly used source of highly energetic photons involves using a

high energy accelerator to direct electrons at an x-ray conversion target. The target is generally made of a high-Z material such as tungsten or tantalum and this process is known as bremsstrahlung. A continuous spectrum of photon energies are produced as the electron scatters, and loses energy, in the target [5].

A number of different energies and delivery methods have been considered. Flash systems, capable of delivering intense (<100 ns), pulses [45] have been investigated, as were non-flash repetitively pulsed [52] [50] or continuous wave sources [53]. The maximum photofission cross section (380 mb) for ^{235}U occurs at approximately 13.8 MeV [50] and so photon energies ranging up to around this value have been investigated for ^{235}U. Higher energies, up to 20 MeV, have been investigated for interrogating other fissile materials [54].

For each setup a response is measured in terms of prompt and delayed fission neutron and gamma products. A bremsstrahlung photon source has been shown to provide a high active interrogation output, relative to other methods [44]. The continuous spread of energies does result in a significant proportion of the interrogation flux being of insufficient energy for photofission and so can represent unwanted background flux. Current cargo screening regulations, such as 21 CFR 179.21, limits the energy of any interrogation source to below 10 MeV. This applies to the interrogation of any cargo containers that may contain food products.

1.4.2.2 Characteristic Gamma Source

Utilising an appropriate monoenergetic source means that any photons that are insufficiently energetic for photofission and would represent unnecessary background signal at the detector are excluded.

A number of experiments have been conducted using characteristic gamma sources produced using beam target interactions such as ^{11}B(p,γ)^{12}C, ^{19}F(p,$\alpha\gamma$)^{16}O and ^{7}Li(p,γ)^{8}Be to produce mono-energetic photons between 6 and 18 MeV [51].

Sources of this type involve causing fission events by accelerating protons towards a solid target to induce nuclear reactions that generate monochromatic photons [55]. These targets can be crystalline, such as CaF_2 and MgF_2, or gas, such as SF_6, and produce characteristic photons as well as alpha particles when bombarded with high energy protons from an accelerator [56].

Figure 1.1 shows the photofission cross sections for each SNM [57]. It can be seen that most fission occurs at photon energies of 5 - 20 MeV. This suggests that sources of this kind would be appropriate as all emitted photons occur within this range. Whilst the high energy, monoenergetic, photons produced in these reaction are desirable the lower output represents a major drawback for many potential active interrogation scenarios [44].

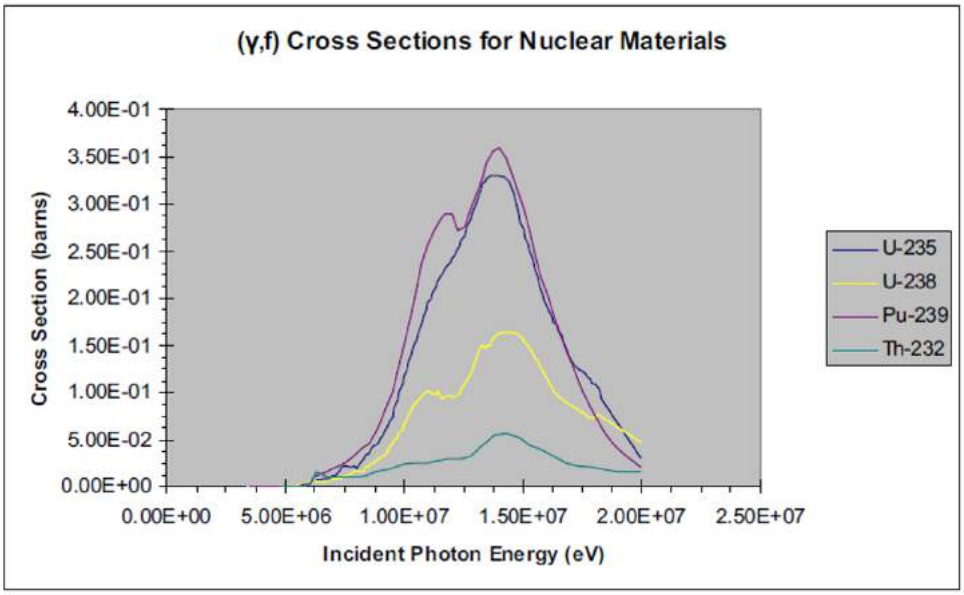

Figure 1.1: Photofission cross section in nuclear materials of interest ©IEEE 2007 (Blackburn)

1.4.2.3 Accelerator Based Photoneutron Sources

A potential source of high energy neutrons for active interrogation involves using bremsstrahlung radiation to produce neutrons from an appropriate target. These targets are generally materials with the smallest binding energy, D_2O or ^{9}Be [58]. These reactions can be written:

$$^9_4Be + h\nu \rightarrow ^8_4Be + ^1_0n \qquad Q = -1.665MeV \tag{1.1}$$

$$^2_1D + h\nu \rightarrow ^1_1H + ^1_0n \qquad Q = -2.225MeV \tag{1.2}$$

High-Z targets capable of withstanding a high energy such as lithium deuteride (LiD), depleted uranium, or natural Pb can also be used [59]. Figure 1.2 [57] shows yields, plotted against neutron energy, for a selection of similar targets exposed to 9 MeV endpoint bremsstrahlung photons [57].

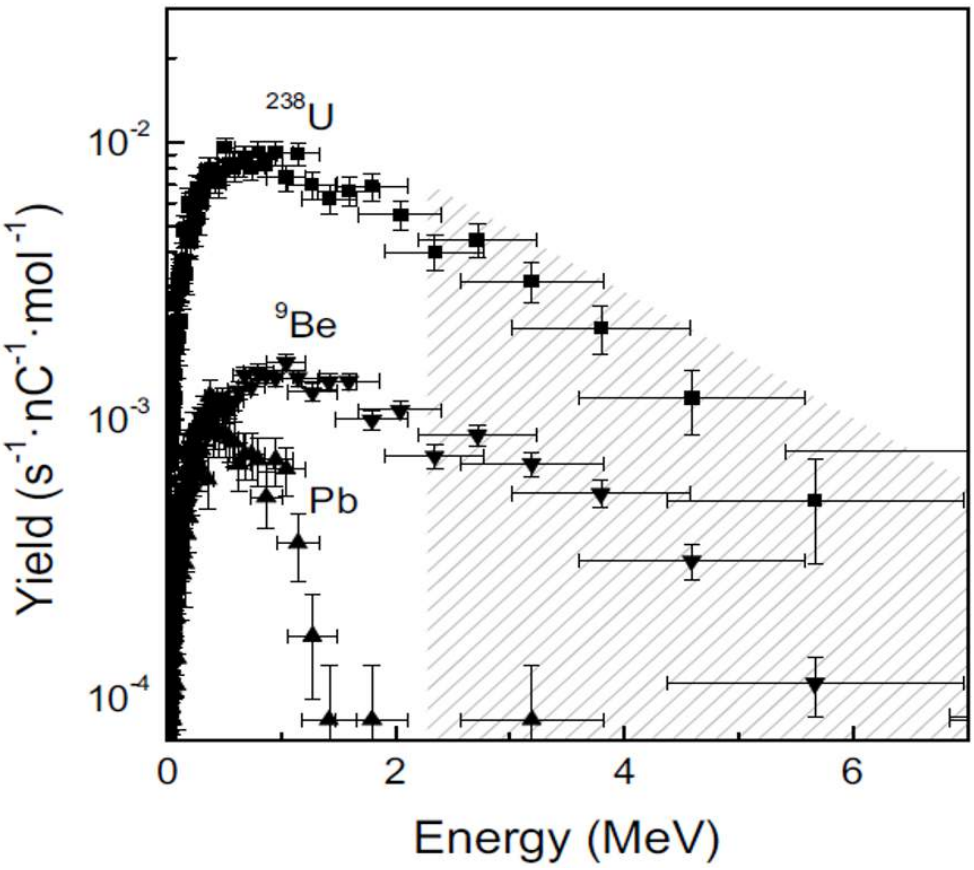

Figure 1.2: Energy spectra of neutrons emitted from the U-238, Pb and Be-9 targets irradiated by a 9 MeV bremsstrahlung beam. ©IEEE 2007 (Blackburn)

The advantage of photoneutron sources is that a mono-energetic photon source can be used to achieve nearly mono-energetic neutrons. A slight spread in neutron energy results from neutron scattering within the source and the different direction of neutrons from that of the incident photon. Major disadvantages associated with the use of this type of source in active interrogation scenarios is the high gamma flux required and the fact that the incident photons are never completely stopped in the target meaning there is always a high residual photon background [60]. This high gamma flux introduces significant shielding, detection and processing challenges [5]. Separate investigations by AWE [44] and LANL [52] using a 10 MeV bremsstrahlung spectrum and D_2O and beryllium targets respectively have been shown to have a relatively low output, compared to other neutron sources.

1.4.2.4 Neutrons from Charged Particle Induced Reactions

Although alphas are the only low Z heavy charged particles easily available from radioisotopes, and the flux from these sources is too low for active interrogation, it is

possible to artificially accelerate protons, deuterons etc. towards a suitable target in order to produce neutrons. This is done by accelerating the particles to a sufficient energy to overcome the coulomb barrier. For a light target nucleus, such as in those shown in the equations below, this energy does not have to be very high.

$$The\ D-D\ reaction \qquad {}^{2}_{1}H\ +\ {}^{2}_{1}H\ \rightarrow\ {}^{3}_{2}He\ +\ {}^{1}_{0}n \qquad Q = +3.26MeV \tag{1.3}$$

$$The\ D-T\ reaction \qquad {}^{2}_{1}H\ +\ {}^{3}_{1}H\ \rightarrow\ {}^{4}_{2}He\ +\ {}^{1}_{0}n \qquad Q = +17.6MeV \tag{1.4}$$

A heavier target and high energy incident particles can be used to produce more energetic neutrons. Large accelerator facilities, such as cyclotrons or Van der Graaf accelerators, are required to produce sufficiently energetic incident charged particles to generate high energy neutrons from heavier targets [38]. The most frequently used of these involve the ^{7}Li(p,n), ^{7}Li(d,n), ^{9}Be(p,n) and the ^{9}Be(d,n) reactions [5].

This method has been used to generate low energy neutrons (<1 MeV) that can be used in active interrogation via the ^{7}Li(p, n)^{7}Be reaction [47]. Neutron energies as low as 60 keV can penetrate most cargo effectively and can be used to induce fission in SNM with very little background [61].

1.4.2.5 Further Interrogation Sources

Further interrogation sources have been proposed including protons and muons. Due to the charge on these particles they require a significantly higher energies (1 approx. GeV) to probe into a material and so remain in a pre-conceptual state of development [5].

1.4.3 Detection Signatures

For each interrogation scenario that was investigated the fission signature could be detected as a combination of prompt and delayed photons and neutrons. These events provides a signature, in terms of yield, energy and time profile, that is unique and can be used to identify SNM.

1.4.3.1 Prompt Signatures

Prompt emissions are those that occur immediately after fission. Measuring prompt gammas in the presence of an interrogation source presents a major challenge due to

the difficulty of separating these events from the original pulse.

Counting prompt neutrons would provide a highly efficient measurement technique as they yield approximately 2 orders of magnitude more than their delayed counterparts [62]. Although possibilities still exist for investigating this method [53] nobody has, to date and to the best knowledge of the author, succeeded in making use of these prompt neutrons due largely to the intensity of the interrogation beam [63].

1.4.3.2 Delayed Signatures

Delayed signatures consist of neutrons and gammas that originate from the beta decay of fission products and their daughters [5]. The detection of high energy (>2.5 MeV) delayed gammas has been used to identify SNM after initial interrogation bremsstrahlung pulse [54]. A majority of successful investigations have involved detecting delayed neutrons, or a combination of these and delayed gammas [5]. These include those generated by each of the discussed interrogation techniques [44], [52].

1.5 The AWE Scenario

This project forms part of the high flux neutron/gamma detector development project. The work is supported and sponsored by AWE plc and concerns the active interrogation of shipping containers for SNM. The proposed detection scenario involves a high flux, dynamic, mixed field active interrogation environment.

The detection system in the current project was designed to function in the presence of an interrogation beam that results in an extremely intense initial photon flux which is then followed by a decaying field of photons and neutrons.

1.5.1 Interrogation Profile

A number of potential machines capable of providing active interrogation source beams include flash machines, such as the Inductive Voltage Adder (IVA), or linear accelerators. Various targets can be used to generate a range of beam properties such as energy and particle type. For the purposes of this project AWE suggested a working interrogation pulse length of 100ns. Depending on the cargo the useful signal following interrogation could persist for anything from microseconds to seconds.

An illustration of the anticipated time profile of these events is shown in Figure 1.3 [57]. The interrogation pulse is marked as ‘Illumination Time’. During this period

the high intensity causes a large proportion of dead time in which it is not possible to distinguish individual pulses. This period of dead time is marked on the plot up to t_d. A gating system was to be developed by the University of Lancaster, as part of this collaboration, to ensure that the detector is only turned on after this initial interrogation pulse has finished and the response has died away to a level at which a pulse counting detector system could function correctly by distinguishing individual events.

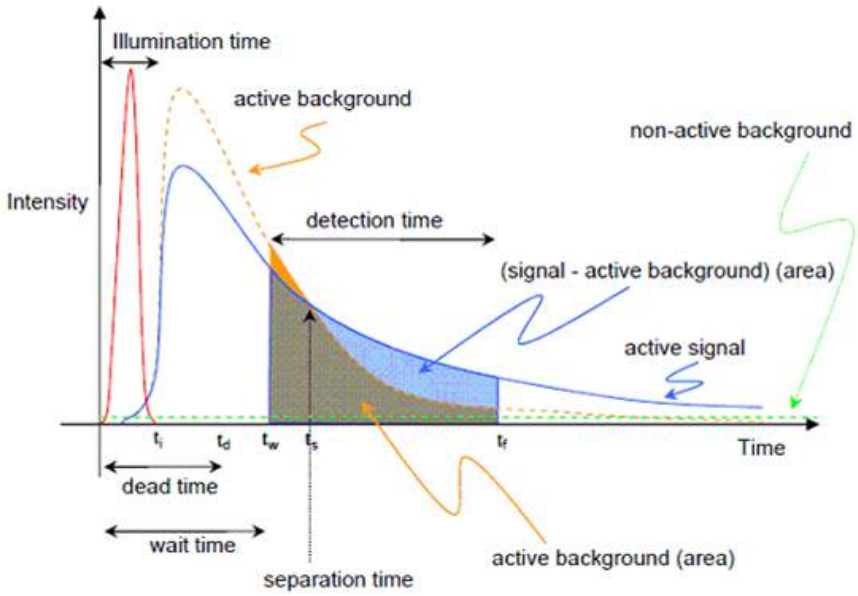

Figure 1.3: Schematic time profile of radiation flux after the initial interrogation pulse (Communication from AWE, 2015).

The 'Active Background' refers to events that occur as a result of interactions between the interrogation pulse and any non-SNM materials that may be present. The time at which the signal is shown to be above the active background is marked by t_s. The region of interest is indicated between t_w and t_f and represents the time in which the detector is to be switched on and events detected.

1.5.2 Detector Requirements

The key requirements of the proposed detection system are as follows:

- The ability to simultaneously detect separate neutron and gamma events. This is to be achieved using Pulse Shape Discrimination (PSD) in the new Eljen EJ-299 plastic scintillator.
- Sensitive detection over a photon energy range of 0.25-3 MeV, and a fast neutron energy range 0.8-5 MeV.

- A high gamma rejection ratio, based on PSD and energy sensitivity information.
- The ability to function in the presence of a very intense initial photon flux. This will be achieved by using an electronic gating circuit to 'blank' the the detector during the initial intense pulse. This is to be controlled using a trigger signal that is synchronised to the primary radiation pulse and a secondary radiation detector and that will switch the detector on for normal operation once the incident photon flux has dropped to a user-set level.
- A secondary imaging system is to be developed that is suitable for localising the SNM source to a region measuring 0.8m x 0.8m x 0.8m when the detector is 2.5m from the source. This corresponds to an angular resolution of approximately 18°.

1.5.3 Proposed Localisation Setup

The proposed detection system involved interrogating a volume of interest the size of a standard shipping container. As well as identifying the presence of SNM an additional design requirement was the ability to localise it to the nearest 80*cm* fixed voxel within the volume. This is a major requirement of this project, as specified by AWE.

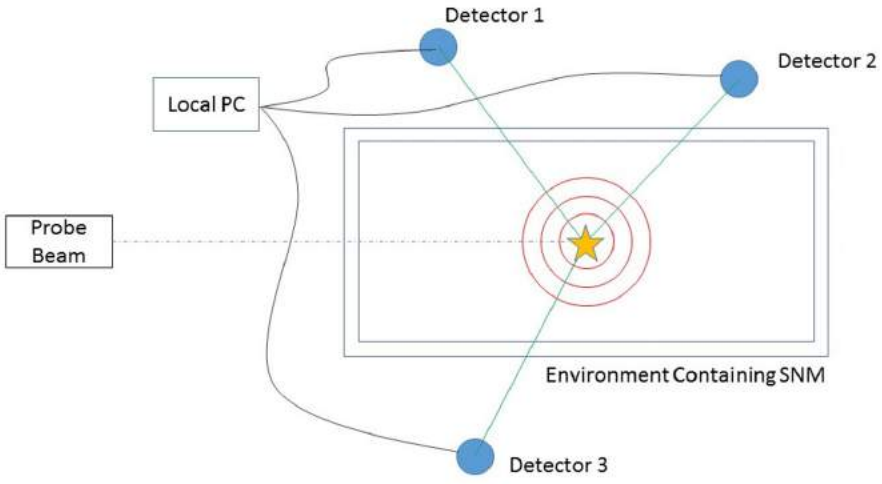

Figure 1.4: A Diagram of the Proposed Setup of the Detector System.

The proposed system involved using individual detectors capable of determining the direction of a source whilst also performing n/gamma discrimination. By placing multiple detectors around the volume of interest, as shown in Figure 1.4, the direction of a source from each position can be determined. It would then be possible to determine the position of the SNM, within a volume, by finding the point at which these directions

intersect. A more complete description of the specific flux conditions to be investigated, and the detector setup, is detailed in Chapter 4.

1.6 The RadICAL Detector System

In order to fulfil the imaging requirements a variation of the RadICAL (Radiation Imaging Cylinder Activity Locator) concept [64] was proposed.

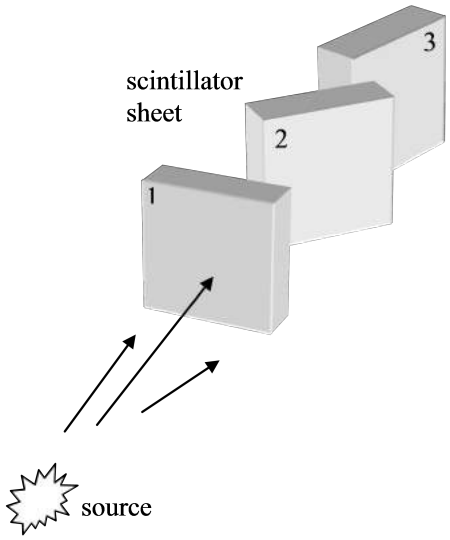

Figure 1.5: The RadICAL concept.

1.6.1 The RadICAL Concept

RadICAL uses an active detection element whose general shape is that of a thin sheet (see Figure 1.5). When the sheet is presented to the source face-on the area of the detector is at its largest. When the sheet is turned so that only the edge is presented the area is at its smallest. Thus if the sheet is continually rotated the solid angle subtended by the detector varies as it is rotated in the radiation field. However, to derive the signal created by such a rotating detector sheet it is necessary to consider the energy deposited by incoming radiation. If the flux of particles is a photon beam then the probability of interaction and hence the deposition of energy in the detector depends upon the radiation pathlength presented to the source. Thus the combination of area and pathlength determines the total energy deposited and hence the detector output at any point in its rotation. If the detector is arranged to rotate on an axis the detector output will vary with angle and the direction of the source location in the plane perpendicular to the axis of rotation can be found [64].

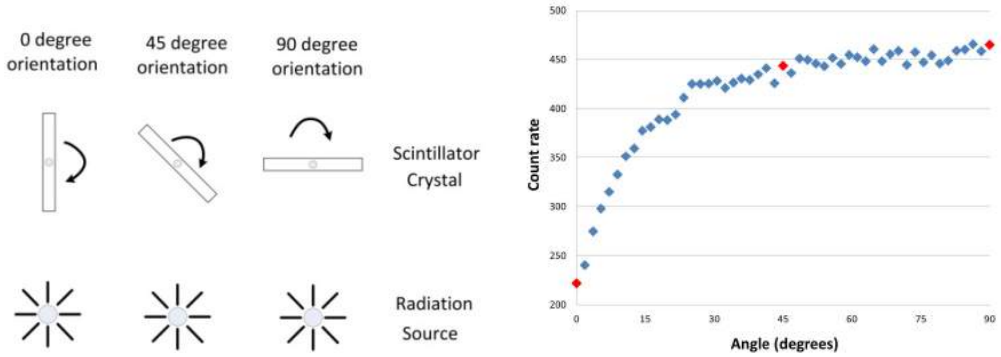

(a) Detector orientation **(b)** corresponding counts

Figure 1.6: Detector response to different orientations

In the example shown in Figure 1.6a the slab of detector is shown to have three orientations, with respect to the source of the radiation, these give rise to the response shown in red. When the slab is rotated through a full 360° degrees the full response curve is mapped out by the blue points. The response curve reaches a minimum when the thin edge of the detector faces the source. When this minimum point is reached the corresponding position of the scintillator can be observed and the source can be assumed to be in the direction defined by the plane that bisects the narrow faces of the detector as shown in Figure 1.6. Operating more than one such detector allows more precise determination of either the location or direction of location. If operated with their axes of rotation at right angles to each other the direction of location will be found in both 'longitude' and 'latitude'. If operated with their axes parallel to each other then triangulation allows the location of the source rather than just its direction to be found in one plane. This option is shown in Figure 1.7.

A full investigation into this concept has been conducted and is detailed in chapters 2 and 3 of this thesis.

1.6.2 The RadICAL Stack Concept

There is an intrinsic drawback to the system described in Section 1.6.1 that is due to the time required to rotate the scintillator and determine the direction of a source. Even a large detector exposed to a large flux will still need to be rotated at least 180° before any directional information can be achieved. In a dynamic field, such as those investigated during active interrogation, the time required to rotate between positions would invalidate the concept. In the proposed active interrogation environment all events of

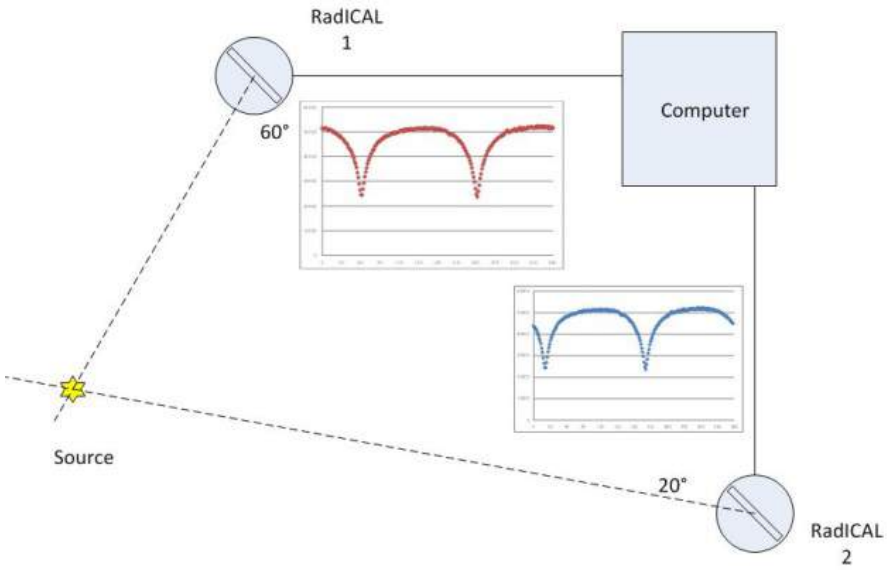

Figure 1.7: 2 RadICAL detectors used together to locate source in 2 dimensional plane.

interest occur with a constantly decaying probability over a period shown as 'detector time' in Figure 1.3.

A proposed variation on the RadICAL concept provides a potential solution to this problem and involves replacing the single rotating detector with a stack of identical scintillators directly coupled to photodetectors and separated at fixed angles around the central axis of each slab of scintillator as shown in figure 1.8.

By rotating the stack of detectors, in relation to a source, the flux that is incident upon each detector changes as shown in Figure 1.6a. By plotting the count rate against the angle of each detector, relative to the source, a fluctuating curve, known as the Standard Response Curve (SRC), can be plotted for each detector element, as shown in 1.6b, in the same manner as when using a single detector. The SRC from each detector element should be identical and so these can be combined, or a single one can be chosen, as the calibration Standard Response Curve (cSRC).

Once a cSRC is determined the stationary detector can then be used to determine the direction of a source. This is done by simultaneously acquiring counts with each detector element. By plotting each of these count rates, at their respective angles, on top of the cSRC the direction of the source can be determined using a least squares fit.

The number of detector elements necessary to locate a source depends on the flux conditions, detector size, field of view and angular resolution required.

A full investigation into this concept has been conducted and is detailed in chapters

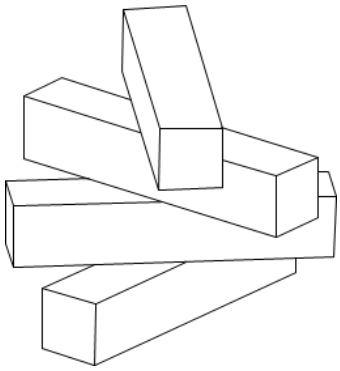

Figure 1.8: The proposed stack detector geometry.

3 and 4 of this thesis.

1.6.3 Pulse Shape Discrimination

When using scintillation detectors to detect neutrons it is usually necessary to distinguish neutrons from a larger gamma field. This is normally done by observing the different shaped pulses of electric current from the photodetector which correspond to neutrons or gammas interacting in the scintillator. This process is known as Pulse Shape Discrimination (PSD).

In most scintillators nearly all of the light produced by scintillation is promptly emitted and can be described by a short decay time component. In some materials, notably Stilbene and various oxygen-free liquid scintillators, a sizeable longer time component is also present. The composite yield curve can often be described adequately by the sum of the two exponential decays, represented by each of these components [38].

The prompt component results from the direct radiative de-excitation of singlet states. In this process an electron, which forms a singlet pair with a ground state electron with opposite spin, is excited to a higher energy level by incident radiation and then immediately de-excites with the emission of light.

The slower component results from a triplet exciton diffusion process followed by triplet-triplet annihilation. A triplet state is formed when an excited electron forms a pair with a ground state electron with the same spin. This leads to the excitation of additional singlet states that decay with the same spectral distribution, but over a longer time period [6]. The slow component is LET (linear energy transfer or dE/dx) dependent and so becomes pronounced by particles with denser tracks such as alpha particles or fast neutrons [65].

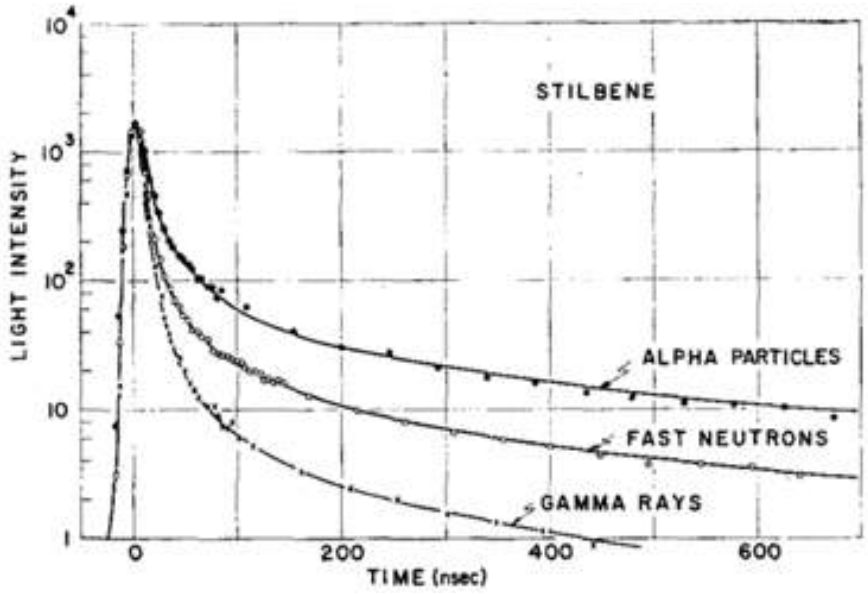

Figure 1.9: Time dependence of scintillation pulses in stilbene, normalized to equal heights at time zero, when excited by radiations of different LET. The curve labelled neutrons represents the protons generated by (n, p) interactions. (Bollinger, 1961)

The effect of these time constants on the pulses can be observed by a measurable difference between the trailing edges of each pulse, relative to their height [66]. Figure 1.9 [67] shows examples of pulse shapes produced by different interactions in Stilbene. One problem which can arise from this method is pulse pile-up, which is when a high flux can make it difficult to distinguish between individual events.

Liquid organic scintillators have been used for this process for several decades. As well as their good PSD abilities they are also known for their good efficiency and fast timing properties. A number of potential problems limit the use of these materials due to the risk of inflammability [68]. A new PVT based plastic scintillator, EJ299, has been developed to deliver PSD in a similar manner to established liquid scintillators. This offers neutron detection properties without the handling problems associated with liquid organic scintillators. Initial tests have suggested that the material functions as expected, although there are some indications of an additional component with a very long lifetime [69].

An investigation has recently been conducted into the possibility of discriminating between the pulses by looking at the rising edge, instead of the falling edge [70]. The advantage of this method is that the rising edge has a steeper gradient than the falling edge and so, in theory, it should be easier to discriminate over short time period and

should be less susceptible to pulse pile up. Work on this technique is ongoing but would offer a significant advantage, particularly in high flux environments.

1.7 Photon Interactions

In order to understand how radiation is detected it is important to know how it interacts, and deposits energy, within the detector or any other material. Photons can interact by one of four major processes: coherent scattering, photoelectric effect, Compton scattering and pair production [60]. The probability of each is determined by the atomic number and density of the material and on the energy of the photon [38]. As photons pass through a material they are attenuated by a combination of these processes which causes an exponential decrease in photons/unit area. This can be described by equation 1.5 where N/N_o is the proportion of incident photons traversing thickness x of a medium and μ is the linear attenuation coefficient. A further factor to consider is that the intensity of photons decreases as a source is moved further away according to the inverse square law [60].

$$N/N_o = e^{-\mu(E)x} \tag{1.5}$$

Figure 1.10 [71] shows the attenuation coefficient for caesium iodide, a commonly used inorganic scintillator, over a range of photon energies from 1 keV to 100 MeV. The plot is broken down between the different interactions. It can be seen that the photoelectric effect dominates at lower energies and pair production begins to dominate at very high energies. Compton scattering occurs throughout a large range of energies and dominates between around 0.3 and 6 MeV [71].

1.7.1 Coherent Scattering

Coherent (Rayleigh) scattering occurs with atomic electrons whose binding energy is much higher than that of the incoming photons [60]. Because the photon energy is insufficient to dislodge the tightly bound electron the whole atom recoils and the photon is scattered elastically without a significant change in energy or therefore wavelength [60]. Coherent scattering is most likely at low energies or in high-Z materials. Because only a negligible amount of energy is deposited in this process its direct importance to radiation detection is limited [60].

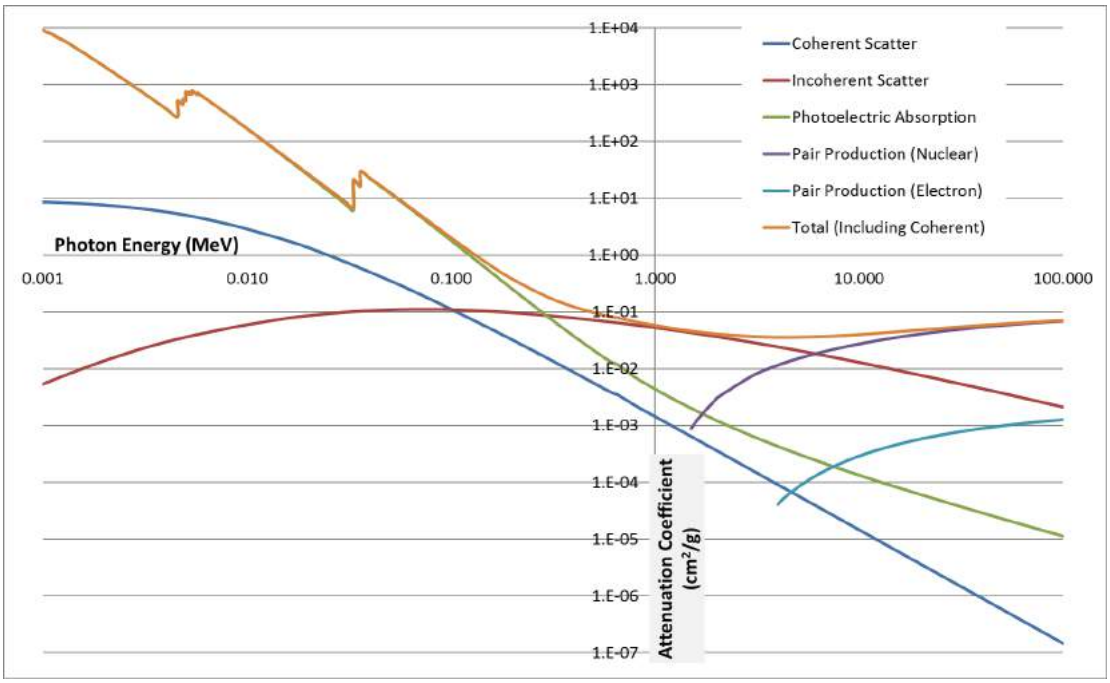

Figure 1.10: Attenuation coefficients by interaction for Caesium Iodide

1.7.2 Photoelectric Effect

Photoelectric absorption occurs when an incident photon interacts with a bound electron, overcome its binding energy and ejects it from the atom giving up all of its energy in the process. Any remaining energy is passed to the electron as kinetic energy. The ejected electron will leave a vacancy in the K- (or L-, M-..) shell which will result in the de-excitation of the atomic system, either by characteristic X-ray or Auger-electron emission. The probability of this interaction occurring is strongly dependent on the energy of the incoming photon and the Z value of the material and is described by the atomic cross-section $a^{\tau}(cm^2/atom)$ [60].

1.7.3 Compton Scattering

Incoherent, or Compton, scatter occurs when an incoming photon interacts with an electron, whose binding energy is negligible compared to that of the photon, imparting the electron with some of its energy and causing both to scatter [38]. The photon undergoes a change in energy and direction, these are described by:

$$hv' = \frac{m_o c^2}{(1 - cos\theta) + \frac{m_o c^2}{hv}} \tag{1.6}$$

where hv' is the energy of the scattered photon (Planck's constant x frequency),

hv is the energy of the incident photon, $m_o c^2$ is rest mass energy of an electron (511 keV) and θ is the scatter angle of the photon from its original path of travel [60].

1.7.4 Pair Production

At incident photon energies above 1.022 MeV a further interaction becomes increasingly important - pair production. In this interaction the incident photon is completely absorbed within the field of a charged particle - mostly in the strong Coulomb field of the nucleus, although it can also occur at high energies in the field of an electron [60]. The photon is replaced with an electron and positron pair. The threshold energy of 1.022 MeV corresponds to the sum of the rest mass energies of the two electrons [38].

1.8 Neutron Interactions

Neutrons carry no charge and therefore do not interact with matter by means of the coulomb force, which is the dominant interaction for electrons and other charged particles. Hence the neutron can pass through many centimetres of matter without interaction and when it does interact it is with the nucleus of a material. As a result of the interaction the neutron can either scatter, resulting in a change in energy and direction, or be absorbed by the material which results in secondary radiation or fission fragments. Most neutron detectors utilise these secondary charged particles for detection. The probability of each interaction occurring depends on the energy of the neutron and nucleus it strikes and the neutron cross-section of the material with which it interacts [72]. Figure 1.11 shows the elastic scattering and absorption cross-section for neutrons in hydrogen plotted against energy.

1.8.1 Neutron Scattering

At low energies (1 eV - 20 MeV) slow and thermal neutrons are most likely to undergo elastic scattering. Because of the small kinetic energy of these neutrons very little energy is transferred and so, despite their high probability, these interactions are not ones that neutron detection can be based upon [38].

At higher energies the probability of interaction begins to reduce but the (fast) neutrons can impart more energy through elastic scattering. This normally results in the scatter of secondary charged particles that can then be used for detection. As energy is increased fast neutrons can also undergo inelastic scattering in which energy is

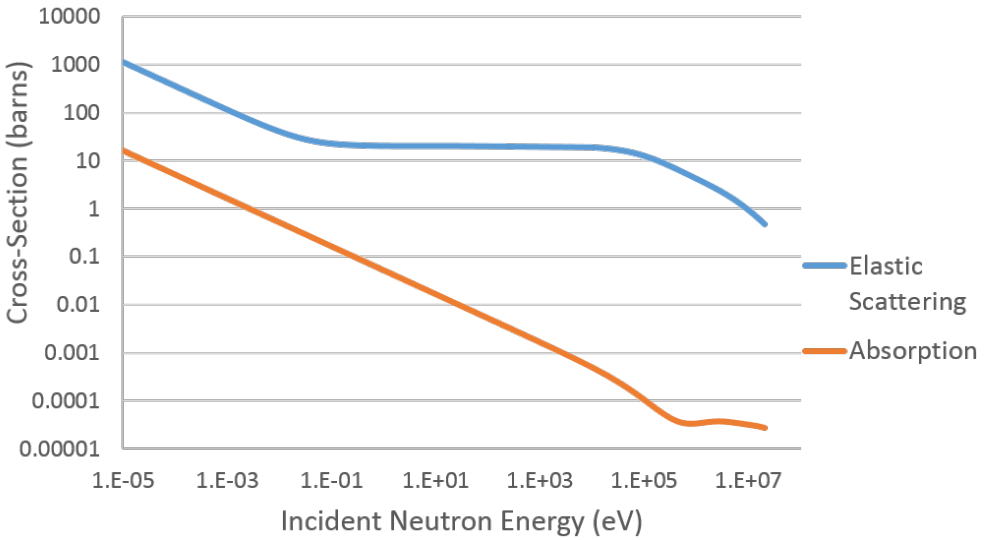

Figure 1.11: Microscopic neutron cross-sections for elastic scattering and absorption for H-1 (from https://www-nds.iaea.org/exfor/endf.htm)

deposited by elevating the recoil nucleus to one of its excited states during a collision. As the nucleus de-excites a gamma ray is emitted and the neutron loses a greater fraction of its energy than it would in an equivalent elastic collision. This process plays an important role in the shielding of high energy neutrons but the secondary gamma rays cause unwanted complications in the response of fast neutron detectors [38].

1.8.2 Neutron Absorption

When a neutron is absorbed, or captured, by a nucleus a wide range of radiations can be emitted or fission can be induced. A variety of emissions can follow including photons, protons, alpha particles or more neutrons. The emission of only one neutron is indistinguishable from a scattering event. The direct detection of neutrons is difficult due to their lack of charge but the detection of charged particles, that are emitted following the absorption of a neutron, is a commonly used method of neutron detection.

At higher energies the absorption of a neutron, within a nucleus, can cause a fission event, leading to two or more products. For the EJ-299 plastic scintillator, described in section 1.6.3 of this report, the most common interaction with a fast neutron is its elastic scattering by a constituent hydrogen nucleus and the subsequent production of energetic recoil protons at a range of energies from zero to the maximum energy deposited by the scattered neutron. These protons deposit energy in the scintillator which results in a similar light response that can be detected [73].

1.9 Scintillators

Scintillators are materials that produce a small flash of light when a nuclear particle or radiation deposits energy within them. By coupling the scintillator material to a photodetector these light pulses can be converted to electric current that can be analysed and counted to process information about the incident radiation. Energy is absorbed by different processes, depending on the scintillator material, and is then emitted as scintillation light through fluorescence or phosphorescence [74]. Fluorescence refers to light production through the prompt de-excitation of an excited singlet state and results in a fast response and relatively short wavelengths. Phosphorescence refers to longer wavelength light with a characteristically slow response time and occurs when some excited singlet states are converted to triplet states through a transition known as intersystem crossing. Light is produced by the de-excitation of these states but these transitions are statistically less likely and so this can explain the longer response time associated with phosphorescence [38].

A large variety of different scintillator materials are available. Each material has a variety of different properties which are of varying levels of importance, depending on the application. Tables 1.3 [38] and 1.4 [38] detail the properties of several of the more commonly used inorganic and organic scintillators. Desirable scintillator properties include:

- High density and scintillation efficiency so that the majority of incident photons will be converted into optical photons in a way which is proportional to the energy deposited.
- Transparent to the wavelength of its own emission so that the optical photons generated pass unimpeded to the photodetector.
- Good optical quality and have a refractive index close to that of glass and air so that the optical photons generated can travel efficiently to the photodetector.
- High energy resolution when installed in a detector system. This is related to the light yield, as well as various other material properties of the detector.
- A solid structure and the ability to be effectively machined or shaped into the chosen geometry.

- Decay time of induced luminescence should be short so that individual pulses are easily separated and processed.
- Scintillators vary greatly in price. This is a practical consideration. In large volumes plastic scintillator slabs may be the only option.
- Wavelength of emission should match sensitivity of chosen photodetector.
- Some scintillators are more durable than others. This may be a factor in some applications.
- Some scintillators have hygroscopic properties and can degrade on contact with moisture in the air. Materials of this nature must be kept within an airtight container.

1.9.1 Inorganic Scintillators

Inorganic scintillators refer to materials that form crystalline structures and therefore possess long range order. When radiation deposits energy within the scintillator an electron is excited from the valence band to the conduction band. If the deposited energy is greater than the band gap energy then a mobile electron is produced and its less mobile hole is left behind in the valence band. These can diffuse independently through the material. For lower energies the coupled electron-hole system can transport excitation energy, but not charge through the material. Trapping centres exist within the scintillator in the form of either natural impurities that exist within the material or activators that are added to an otherwise perfect crystal (e.g. caesium iodide that has been doped with sodium). These trapping centres create electronic levels within the band gap. It is the capture of the electron-hole pairs within these band-gaps, followed by their de-excitation, through photon emission, that results in the production of light that is used for radiation detection. Inorganic scintillators have good energy resolution, poor timing resolution, high density and a high atomic number, compared to other scintillators [60].

1.9.2 Organic Scintillators

Organic scintillators are aromatic hydrocarbon compounds that contain benzene ring structures. They exist as pure crystals but are normally dissolved in liquid or suspended

	Specific Gravity	Wavelength of Max. Emission (nm)	Refractive Index	Decay Time (s)	Absolute Light Yield in Photons/MeV	Relative Pulse Height Using Bialkali PMT
Alkali Halides						
NaI(Tl)	3.67	415	1.85	0.23	38000	1
CsI(Tl)	4.51	540	1.8	0.68(64%), 3.34(36%)	65000	0.49
CsI(Na)	4.51	420	1.84	0.46, 4.18	39000	1.1
Li(Eu)	4.08	470	1.96	1.4	11000	0.23
Other Slow Inorganics						
BGO	7.13	480	2.15	0.3	8200	0.13
CdWO4	7.9	470	2.3	1.1(40%), 14.5(60%)	15000	0.4
ZnS(Ag) (polycrystalline)	4.09	450	2.36	0.2		1.3
CaF2(Eu)	3.19	435	1.47	0.9	24000	0.5
Unactivated Fast Inorganics						
BaF2(fast component)	4.89	220		0.0006	1400	na
BaF2(slow component)	4.89	310	1.56	0.63	9500	0.2
CsI(fast component)	4.51	305		0.002(35%), 0.02(65%)	2000	0.05
CsI(slow component)	4.51	450	1.8	multiple, up to several μs	varies	varies
CeF3	6.16	310,340	1.68	0.005, 0.027	4400	0.04 to 0.05
Cerium-Activated Fast Inorganics						
GSO	6.71	440	1.85	0.056(90%), 0.4(10%)	9000	0.2
YAP	5.37	370	1.95	0.027	8000	0.45
YAG	4.56	550	1.82	0.088(72%), 0.302(28%)	17000	0.5
LSO	7.4	420	1.82	0.047	25000	0.75
LuAP	8.4	365	1.94	0.017	17000	0.3
Glass Scintillators						
Ce activated Li glass	2.64	400	1.59	0.05 to 0.1	3500	0.09
Tb activated glass	3.03	550	1.5	3000 to 5000	50000	na

Table 1.3: Inorganic Scintillators (Knoll, 2000)

in a polymer structure and so do not normally possess long-range order [74]. The light production mechanism involves transitions between electronic, vibrational and rotational states, as shown in Figure 1.12 [60]. When energy is deposited in an organic scintillator its molecular system is excited to one of several electronic states. When the energy deposited is high enough to populate a higher electronic state there is rapid decay, by radiation-less transitions through vibrational and rotational states to the first excited electron state. The decay of the first excited electronic state can take place to the various vibrational states of the ground electronic state with the emission of fluorescent light [60].

Compared to other materials organic scintillators have low density and atomic number, good timing resolution and poor energy resolution. They are usually cheaper

	Light Output Anthracene (%)	Wavelength of Max Emission (nm)	Decay Constant (ns)	Attenuation Length (cm)	Refractive Index	H/C Ratio	Density (g/cm^3)	Softening or Flash Point (C)	Uses
Crystal									
Anthracene	100	447	30		1.62	0.715	1.25	217	
Stilbene	50	410	4.5		1.626	0.858	1.16	125	
Plastic									
EJ212	65	423	2.4	250	1.581	1.103	1.032	70	General Purpose
EJ264	68	408	7.8	160	1.58	1.107	1.032	70	Fast Counting
EJ200	64	425	2.1	380	1.58	1.104	1.032	70	TOF counters, large area
EJ208	60	434	3.3	400	1.58	1.104	1.032	70	General Purpose, large area, long strips
EJ232	55	370	1.4	5	1.58	1.102	1.032	70	Very fast timing, small sizes
EJ248	60	425	2.2	350	1.59	0.995	1.049	100	General purpose
EJ240	41	428	285	180	1.58	1.109	1.032	70	Phoswich detectors for dE/dx studies.
EJ256	32	424	2.1	150	1.58	1.134	1.08	60	X-ray dosimetry (100 keV)
EJ252	46	423	2.4	200	1.58	1.098	1.037	65	Dosimetry
EJ299	56	420				1.08			Pulse Shape Discrimination

Table 1.4: Organic Scintillators (Knoll, 2000)

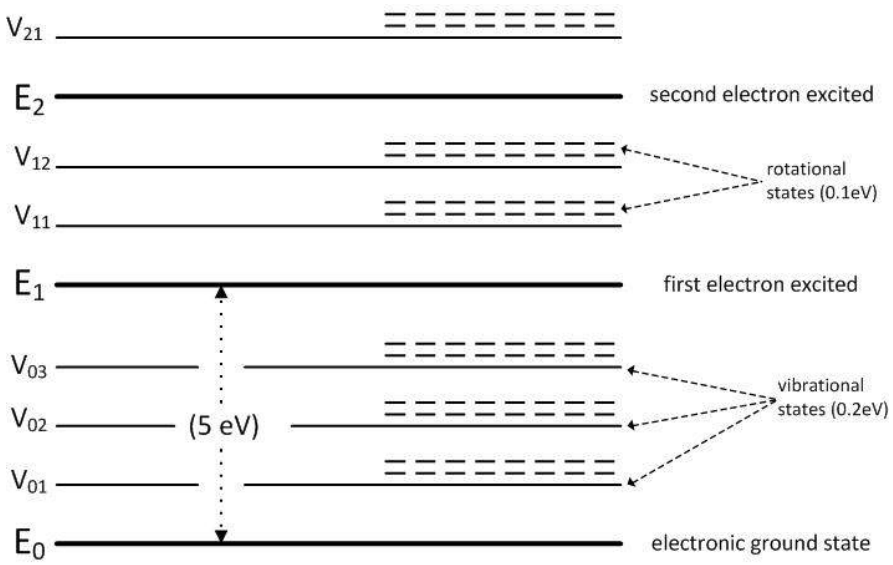

Figure 1.12: Light production mechanism in organic scintillator.

to produce in large quantities than inorganic scintillators.

1.9.3 Neutron/Gamma Discriminating Scintillators

A variety of different scintillators are available that can be used for the development of an n/gamma imaging system. This technology has been around for decades and has traditionally been conducted using liquid based organic scintillator detectors. EJ-299 is

a polyvinyltoluene (PVT) polymer loaded with a scintillating dye, 2.5-diphenyloxazole (PPO) that has PSD properties and has been recommended for use with the final imaging system [6]. Studies have shown that this material provides efficient PSD but has been shown to be less effective than an equivalent geometry of commonly used EJ-309 liquid scintillator. Great advantages are introduced for field applications due to the risk of leaks or inflammability of liquid scintillators and the ease of machining EJ-299 [68].

1.10 Photodetectors

An important component of any scintillation detector system is a sensitive photodetector capable of converting the very low light output of a scintillator into a corresponding electric signal. A number of different options are available

- Photomultiplier Tube: This remains the most well established and widely used device for this purpose. In a PMT incident photons pass through the window and strike the photocathode, producing electrons as a consequence of the photoelectric effect. These electrons are accelerated towards a series of dynodes of increasing voltage. As these electrons strike each dynode more electrons are emitted through secondary emission causing an avalanche effect. PMTs are available in a variety of different diameters from 10 to 200mm and are sensitive to various EM wavelengths from UV visible to near infra-red. A major drawback associated with PMTs is the relatively large cost. They are also extremely fragile and sensitive to sudden changes of HV as well as changing atmospheric conditions, particularly heat.

- Photodiode: This is a form of PIN (Positive|Intrinsic|Negative) detector optimised for sensitivity to visible light. They are solid state so are more robust than PMTs but can only be made in small sizes due to noise considerations. They vary greatly in cost but, in general, are considerably cheaper than PMTs. Their response is usually noisier than that of a PMT and they have no gain.

- Avalanche Photodiode: These are similar to the conventional photodiode but with a high voltage to multiply electrons in a manner similar to the avalanche effect within a PMT. They are more expensive than conventional photodiodes and generally very small but possess similar quantum efficiency and show a current gain

effect. They are generally less noisy than conventional photodiodes but more noisy than PMTs [38].

- Silicon Photomultiplier: These are a new detector type consisting of an array of pixels made of avalanche photodiodes on a common silicon substrate and working on a common load. They offer properties that rival those of conventional PMTs but are only available in small sizes at this time [75].

1.11 Directional and Imaging Detectors

The presence of ionizing radiation can be detected in a variety of ways. Generation of charge pairs in solids or gasses and the conversion of X or gamma-ray energy into optical photons that are subsequently recorded using a photo-detector are two of the most common. In both these cases the probability of detection depends upon the energy of the incoming radiation and the radiation pathlength within the active volume of the detector. There are many detectors of ionising radiation but few combine directionality with detection.

Directional detectors are designed to determine the direction of a radioactive source and are suitable for use when the position of an individual source is to be found. Imaging detectors are generally more complicated and are used to investigate a distribution of sources, such as in nuclear medicine investigations. A selection of the commonly used directional, and imaging, detectors are described below.

1.11.1 Gamma Cameras

One of the most commonly used imaging detectors is called the Gamma Camera and is used within the field of nuclear medicine [76]. These systems use a slab of scintillator crystal to convert incident gamma ray photons into optical photons. These optical photons can then be detected using an array of photomultiplier tubes, as shown in Figure 1.13 [77], to build up an image of the incident gamma photons. A mechanical collimator, normally consisting of a lead sheet with many parallel holes, is placed between the source and the scintillator slab and is necessary to restrict detection of only those gamma rays that travel from the source to the detector and build an image that can be treated as an accurate distribution of the emitting isotope. A major drawback of this system is that the lead collimator is large, heavy and inefficient [78]. A more efficient

version of mechanical collimation uses a coded aperture but this does little to reduce the overall weight of the detection system and makes operation of the system more complex [77].

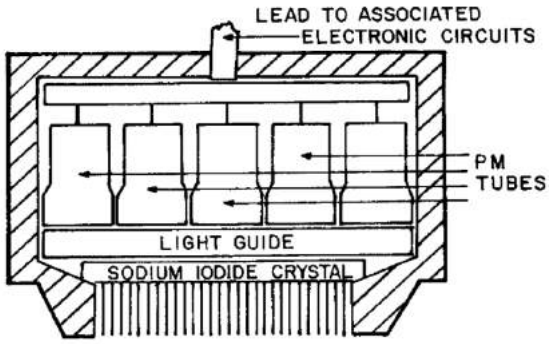

Figure 1.13: Detector assembly of a Gamma Camera (Hendee, 2002)

1.11.2 Electronic Collimation or Compton Cameras

The Compton camera has similar applications to the gamma camera but uses two separate detector planes, usually made of a semiconductor or scintillator material, instead of a lead collimator [79]. The first detector plane is a scattering plane and is made of a material in which the incident photons of interest are most likely to undergo Compton scattering and detects the energy deposited and in which position this happens. The second plane is made of material in which the scattered photons are likely to undergo photoelectric absorption and, again, detects the position and the energy deposited. Every event is recorded so that each absorption can be linked to its corresponding scattering event and the combination of these two positions can be used to find the angle that the scattered photon travelled between the detectors, as shown in Figure 1.14 [80]. The scattering angle of each Compton event can be calculated from the energy deposited in the scattering plane using the Compton equation (1.6). The trajectory of the scattered photon and the angle at which it has scattered can be used to reconstruct the path of the original photon to within the outer edge of a cone shape. By combining several of these cones to find a common intersection it becomes relatively straightforward to determine the position of the source. This method of detection dispenses with the heavy collimator and also offers several other advantages over the Gamma Camera such as increased sensitivity, spatial resolution and field of view. Disadvantages include the need for complex electronics to function and difficulties in reconstructing complex dis-

tributions of isotopes. As well as nuclear medicine applications the Compton Camera can also be used in homeland security and nuclear decommissioning [80].

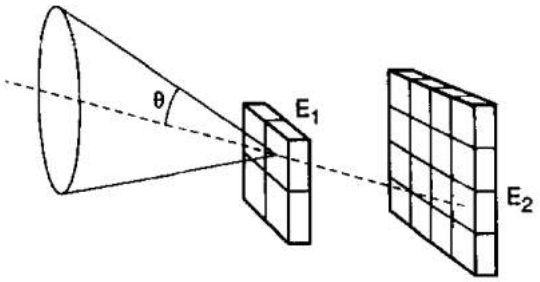

Figure 1.14: Illustration of Compton Camera concept (Phillips, 1995)

1.11.3 Directional Detectors Used in the Nuclear Power Industry

Further requirements for gamma detection are found within the nuclear power industry. Radiation monitoring posts are used as standard in areas around nuclear sites worldwide, as well as for general environmental radiation monitoring. The Euratom Treaty requires each Member State to establish the facilities necessary to carry out continuous monitoring of the level of radioactivity in the air, water and soil and to ensure compliance with basic standards [81]. These normally consist of ion chambers or Geiger-Muller probes that don't provide any directional information [82]. A directional detector would be beneficial in these situations as it would provide information that would help locate any excessive flux that may be caused by release of nuclear material. One

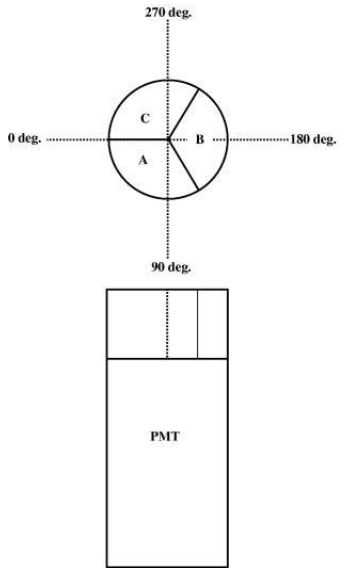

Figure 1.15: 3 Element Detector (Shirakawa 2007)

solution suggested for this application consists of a solid disc of scintillator coupled directly to the window of a photomultiplier tube. This scintillator consists of 3 segments of identical geometry, as shown in Figure 1.15 [83], but each made of different material (BGO, CsI(Tl) and NaI(Tl)). Because each of these scintillators exhibit different material properties and emit light at slightly different wavelength, the photopeak from a single source can be found in different energy channels for each. As a source is moved around the detector the pathlengths through each material changes. As a result the relative amount of energy deposited in each of these scintillators changes and this can be observed in the ratio of the different photopeaks and used to determine the position of the source [83]. A variation on this method involves 3 identical scintillators in the same configuration as described above but each individually coupled to its own photodetector. This involves additional photodetectors but results in response curves that can be easily compared and used to find positional information, regardless of the energy of the source [84].

In decommissioning it is necessary to locate and characterise surface radiation so that it can be disposed of safely and correctly. A variation on the gamma camera has been developed, particularly for this use. The CARTOGAM (Figure 1.16a [85]) consists of a double cone collimator, a scintillator, an image intensifier and a CCD camera and works in a similar manner to a gamma camera but with the added advantage of an optical camera that creates a conventional photograph over which the gamma flux information can be laid [85]. The Radscan (Figure 1.16b) series of devices have been developed by BNFL and are also used in nuclear decommissioning. They are similar to the CARTOGAM and consist of a NaI crystal housed within a tungsten collimator and coupled directly to a silicon photodiode and preamplifier. These components are combined with a CCD camera and an infra-red laser range finder to form a detector head. This detector head is mounted on a mechanical structure that can be controlled remotely to rotate and tilt the detector to form a composite image of the surrounding area [86].

A further method proposed for locating Gamma Ray Bursts from a satellite involves 3 identical thin slabs of scintillator placed perpendicular to each other, as shown in Figure 1.17 [87]. The flux that is incident upon each of these detectors will vary depending upon the relative position of the source. The different flux on each scintil-

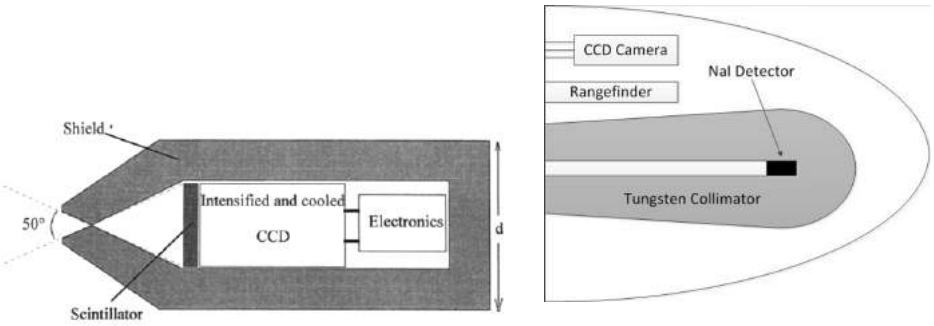

(a) CARTOGAM Detector Head (Gal1997) **(b)** Radscan detector head

Figure 1.16: Schematic cross sections of CARTOGAM and Radscan detector heads.

lator means that the ratio of the counts detected by each can be used to determine the direction of the source [87].

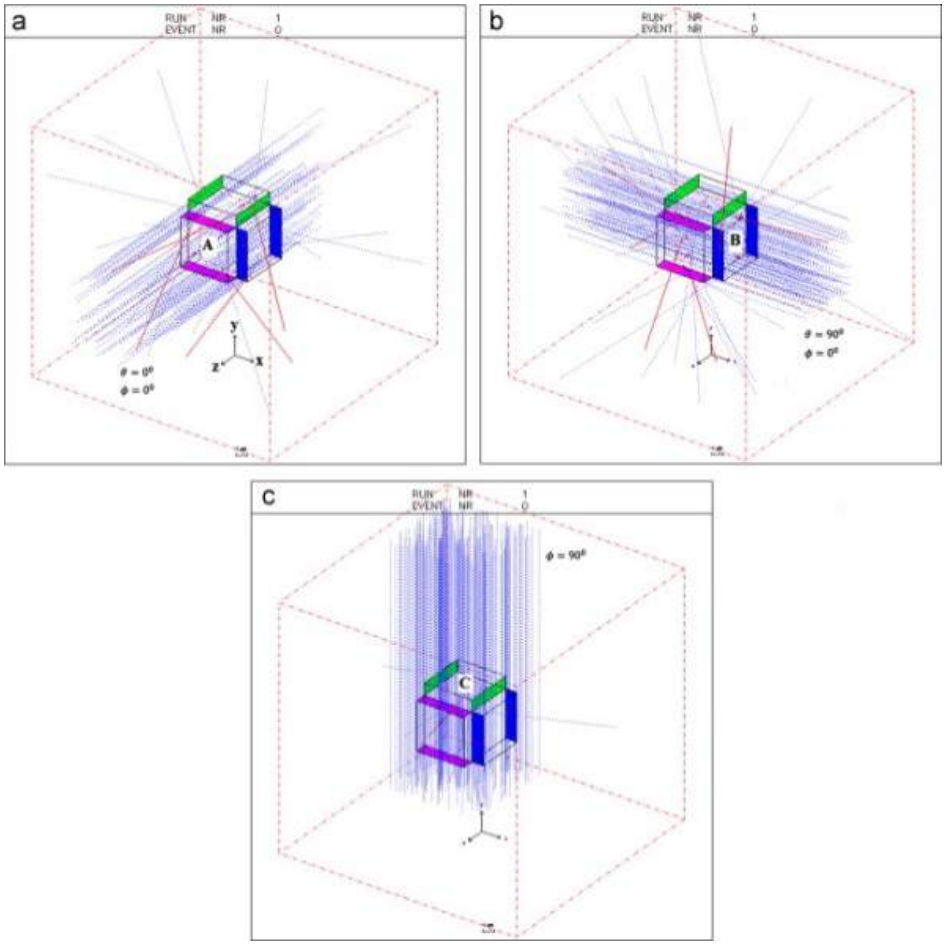

Figure 1.17: Satellite Mounted Slab Detector

1.12 Summary

The problem of interdicting illicit SNM that could be used for a terrorist attack has been introduced. The difficulty of detecting this material, particularly HEU, when transported through major shipping routes has been discussed. Active interrogation is an area of research that offers a viable solution to this problem.

The AWE sponsored high flux neutron/gamma detection project has been introduced. This is a collaboration between UCL, Surrey and Lancaster universities in which UCL is responsible for developing a method of localising any detected SNM to a 0.8m x 0.8m x 0.8m voxel within a volume of interest whilst discrimination neutron from gamma events. A variation on the RadICAL detector concept was proposed as a solution to this problem. The proceeding chapters discuss the work done to investigate this concept.

Chapter 2

RadICAL System Modelling

This chapter describes the work undertaken to develop a RadICAL detector based around the use of a sheet of scintillator. This work was based on the modelling of different detector materials and geometries and investigates the deposition of photon energy in the scintillator as well the transport of optical photons created in the scintillation process. This was approached in both a ray tracing model as well as Monte-Carlo simulations.

2.1 Simple Model

A simple ray tracing model has been developed to evaluate the important parameters to be considered whilst designing a detector based upon the RadICAL concept, described in Chapter 1.6. The model is depicted in Figure 2.1. The source emits photons that interact with the detector. The assumed shape of the detector is a flat slab of width, a, length, b and thickness, c. The incident flux is assumed to be a uniform, parallel beam and is split into a series of raypaths passing through the detector.

As shown in Figure 2.1 the pathlength within the detector takes on a fixed value, l_f or a length that varies l_c within the corners of the slab. The proportion of incident photons that are attenuated (N/N_o) along each of these pathlengths is found from:

$$\frac{N}{No} = 1 - e^{-\int \mu_{en}(E).x(\theta).dx} \tag{2.1}$$

where x takes on the values of either l_f or l_c for angle θ and $\mu_{en}(E)$ is the energy absorption coefficient that corresponds to the energy of the photon and the material of the detector. The energy from each attenuated photon is assumed to be deposited

and converted to optical photons. Summing these raypaths over the whole area of the detector, that is presented to the incident photons at each angle, allows the total signal to be estimated for a given incident flux. The total energy deposited can be determined by multiplying this value by the energy of the incident photons and the number of optical photons generated can be estimated by multiplying the energy deposited by the photon yield of the scintillator. Repeating these calculations for all values of the angle θ gives the response of the scintillator as it rotates in the radiation field. Assuming that the fraction of energy converted to optical photons, the fraction that escapes the scintillator and the fraction detected by the photomultiplier does not depend upon the energy of the incident gamma rays means that scintillator performance can be studied. Several parameters that alter the response function of the detector system have been investigated. The most significant ones are the shape of the active component in the detector, the energy of the incident radiation and the detector material.

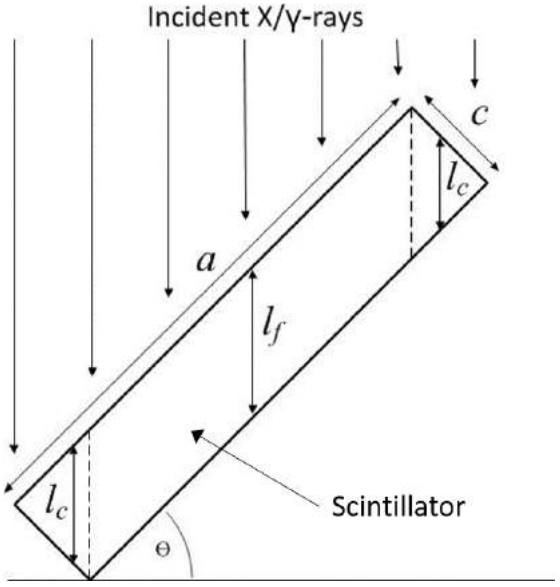

Figure 2.1: Labelled scintillator slab detailing dimensions used in model.

2.1.1 Scintillator Geometry

All model dimensions were defined according to Figure 2.1. The aspect ratio is the ratio of the long and short sides of the scintillator, a:c. This determines the shape of the response curve along with the energy of the incident radiation and the absorption coefficient of the scintillator.

Figure 2.2 shows the expected detector response, from the model, when differ-

ent scintillator geometries are used. In each case the angle of the detector θ, from 0° to 180° is plotted against the count rate. The results shown were based on 600 keV photons incident upon a Caesium Iodide crystal of varying dimensions. At this energy the mass energy-absorption coefficient, μ_{en}/ρ is $0.03657 cm^2/g$ which, when multiplied by the density of the crystal of $4.51 g/cm^3$, results in an attenuation coefficient of $0.1649 cm^{-1}$. In each case the width, a, of the crystal was kept consistent and the thickness, c, was changed to achieve the different aspect ratios shown. The length of the crystal,b (the remaining dimension not shown in Figure 2.1), was also changed in each case to maintain a consistent overall volume and output. As the aspect ratio is increased the width of the characteristic downward peak in the output narrows and its depth increases. This suggests that the angular resolution of the detector will increase as the aspect ratio increases. The signal from the detector is a summation of all the energy deposited in the scintillator and this relates directly to the integration of all the raypaths through the scintillator at a given orientation. When the aspect ratio is low then the change in the integral of all the raypaths through the scintillator as it is rotated goes through a cyclic pattern as shown in Figure 2.2. This pattern changes as the aspect ratio changes.

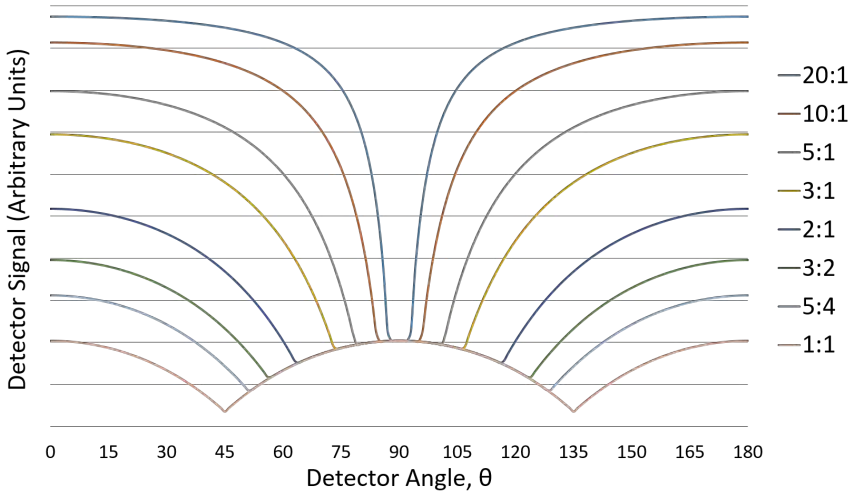

Figure 2.2: Normalised, modelled results of different detectors with different aspect ratios (a:c as shown in Figure 2.1).

2.1.2 Photon Energy

Although the dominant factor governing the changing count rate, that gives the characteristic signal, is the changing area upon which the source is incident the energy of the

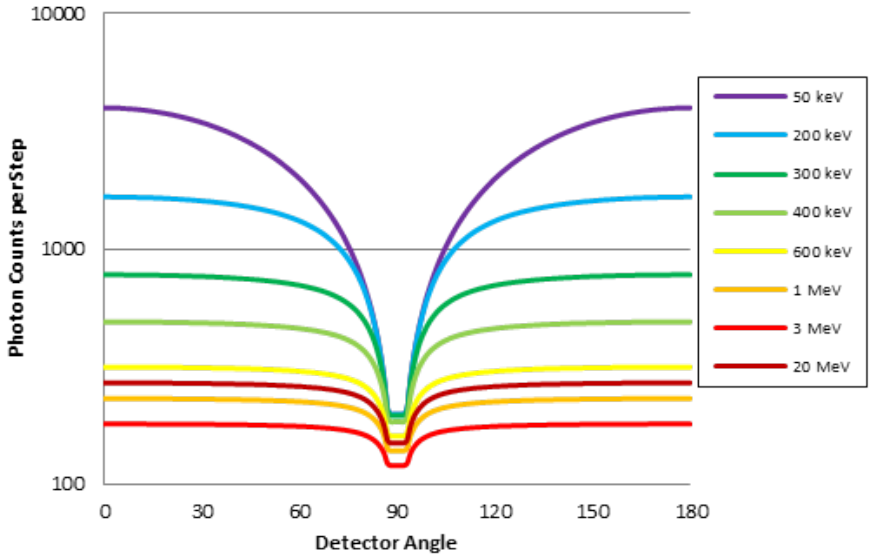

Figure 2.3: Modelled photon counts from rotating 5x100x100mm CsI crystal response to fixed flux of 2000 photons/cm^2 at varying energies.

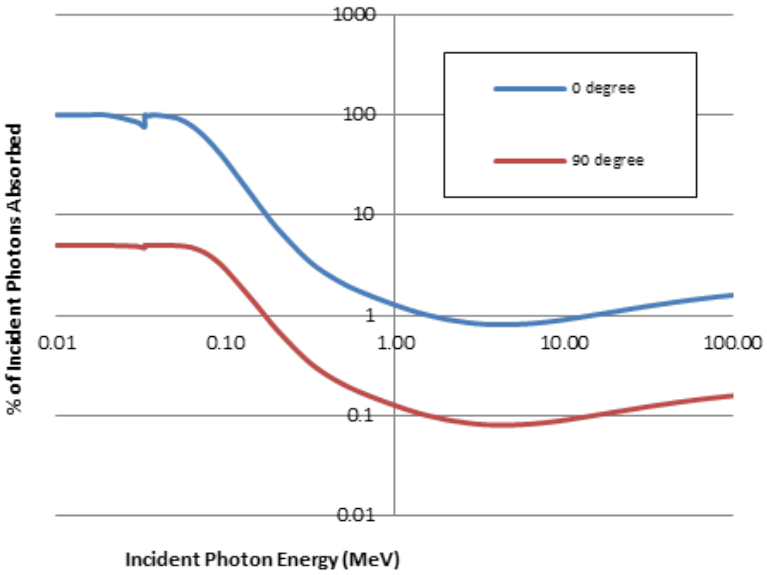

Figure 2.4: Percentage of photons absorbed at different energies at 0 and 90 degree positions for modelled rotating 5x100x100mm CsI crystal exposed to flux of 2000 photons/cm^2.

source also has a significant effect on the shape of the response curve. As the energy of the incident photons increase the probability that an incident photon will be absorbed by the scintillator decreases. Therefore, for a given flux, the proportion of photons that interact with the scintillator decreases as the energy is raised. This is true up until the point at which pair-production becomes a dominant interaction, around 3 MeV for CsI,

and raising the energy above this value results in a slight increase in total interactions. A 5mm x 100mm x 100mm CsI crystal was modelled for the same flux environment detailed in section 2.1.1. The response curves, based on overall photon counts per step, for this model at different energies are shown in Figure 2.3 and the overall count rates in the 0 degree and 90 degree positions at a range of energies are shown in Figure 2.4.

The equivalent plots showing the total energy deposited per step are shown in Figures 2.5 and 2.6. Peaks are shown in figure 2.6 on the 0 degree plot at 60 keV and on the 90 degree plot at 80 keV. These correspond with the highest energy at which most of the photons, over 80% of the incident energy, can be considered to have been deposited in the crystal.

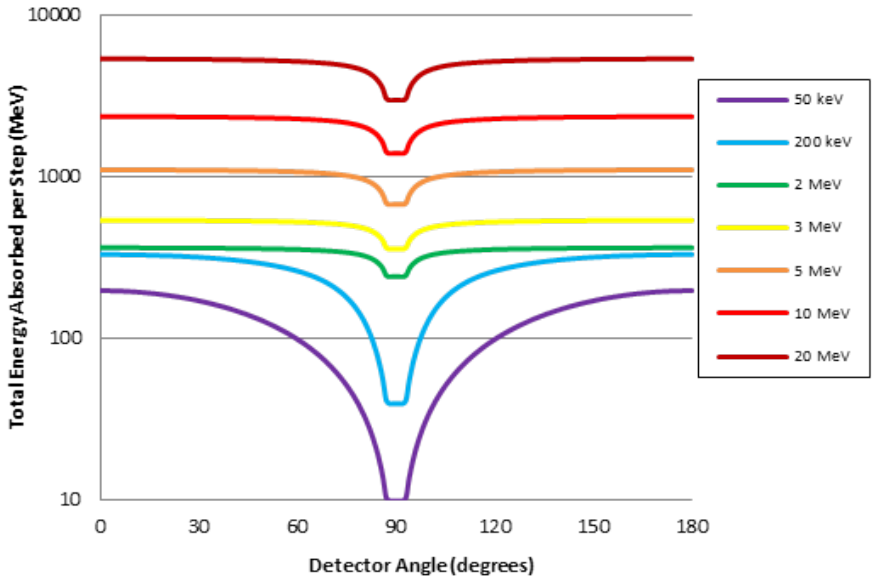

Figure 2.5: Modelled energy absorbed in rotating 5x100x100mm CsI crystal exposed to fixed flux of 2000 photons/cm^2 at varying energies.

Figure 2.7 shows the same modelled data normalised between maximum and minimum count rates. It can be seen that the general shape of this normalised response curve changes with the energy of the incident photons. At low energies (when $e^{-\mu x}$ is close to zero) a large proportion of the incident photons are stopped by the detector, even when the depth of crystal is small. As a result the dominant factor determining the shape of the curve is the surface area upon which the source is incident. The resulting curve shape displays a gradual decline towards the minimum point. For the model shown this convergence occurs below energies of around 60 keV. At high incident photon energies the attenuation coefficient fluctuates a relatively small amount

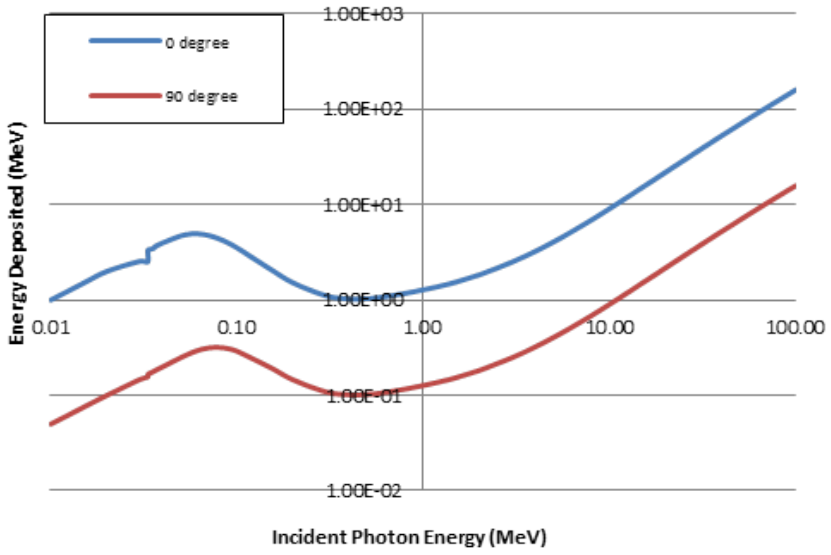

Figure 2.6: Total energy absorbed at 0 and 90 degree positions for modelled rotating 5x100x100mm CsI crystal exposed to flux of 2000 photons/cm^2 at different energies.

as the energy changes. As a result the proportion of photon energy that is absorbed in each position becomes consistent as the energy is raised and the normalised curve shapes converge to a shape that displays a sharp decline towards the minimum point. For the model shown this convergence occurs above energies of around 1 MeV. For intermediate energies the normalised curve displays a variety of different shapes between the two extremes that depend on the specific energy of the photons.

2.1.3 Detector Material

The final major factor governing the shape of the response curve that can be investigated by this simple model is the scintillator material type. Whilst there are a wide range of properties to be considered when choosing a scintillator, as described in Chapter 1.9, a major issue to be considered is the attenuation coefficient of the material. This is intrinsically linked with the energy of the incident photons and results in the same range of response curves as shown previously in Figure 2.7. The scintillator material dictates the energy at which each of these shapes occurs.

For this work two different detector materials were investigated. The first was an inorganic scintillator, Caesium Iodide, which was initially used to build the original RadICAL detector [1] prior to the start of this project. This material was chosen for

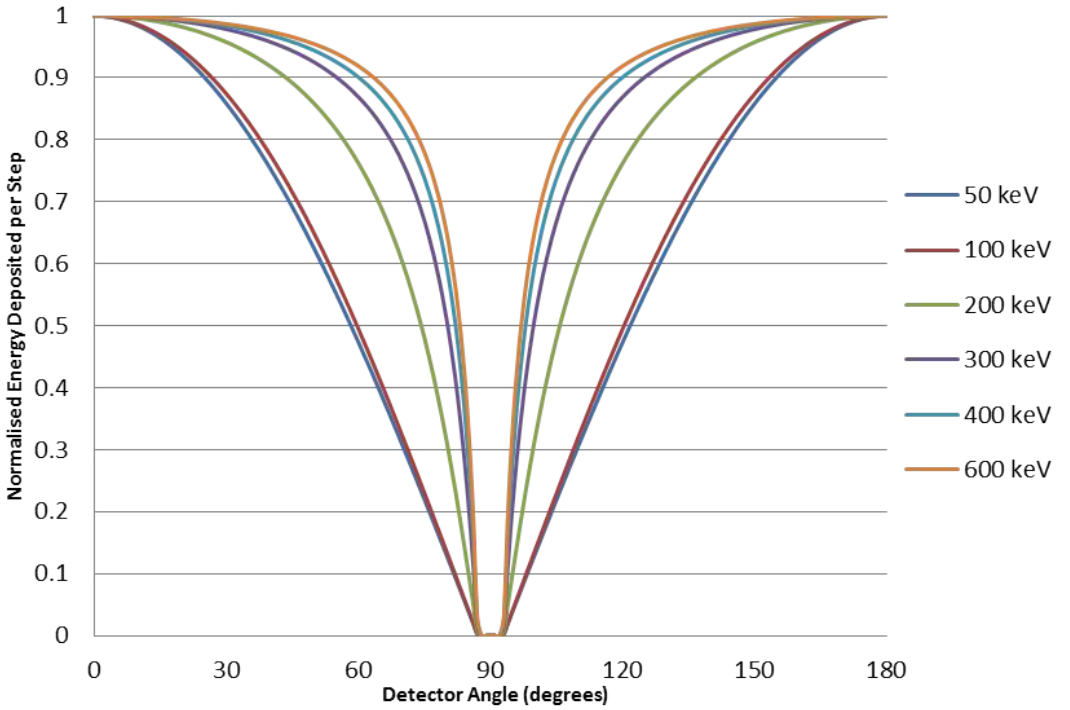

Figure 2.7: Deposited energy, per step, at 0 degree and 90 degree detector position plotted against the variety of different energy incident photons.

a variety of reasons including its high attenuation coefficient and energy resolution. The second was Eljen-EJ299-33, a PVT based organic scintillator which was chosen specifically for its pulse shape discrimination properties.

The linear gamma attenuation coefficients for CsI and for Eljen EJ200, a commonly used PVT based scintillator similar to EJ299, are compared in Figure 2.8 [88] [89]. It can be seen that CsI demonstrates a much higher attenuation coefficient than EJ200. In the plastic scintillator photoelectric interactions dominate at photon energies below 21 keV and the dominant interaction above this energy is Compton scattering. In the CsI this threshold is at 293 keV. In both cases pair production only begins to occur at photon energies of greater than 1.022 MeV and so is left off the plot. One factor not considered in this model is multiple scatter. These effects are more probable in plastic scintillators where Compton scattering is the dominant interaction. As a result the CsI model is likely to be a more accurate representation of actual detector behaviour.

Rotating a 5mm x 100mm x 100mm slab of EJ200 results in a similar spread of response curve shapes to those shown for the same geometry of CsI in Figure 2.7. Figure 2.9 illustrates the spread of energies for each material which result in this range of response curve shapes. For EJ200 the curve shapes converge below 40 keV. Below

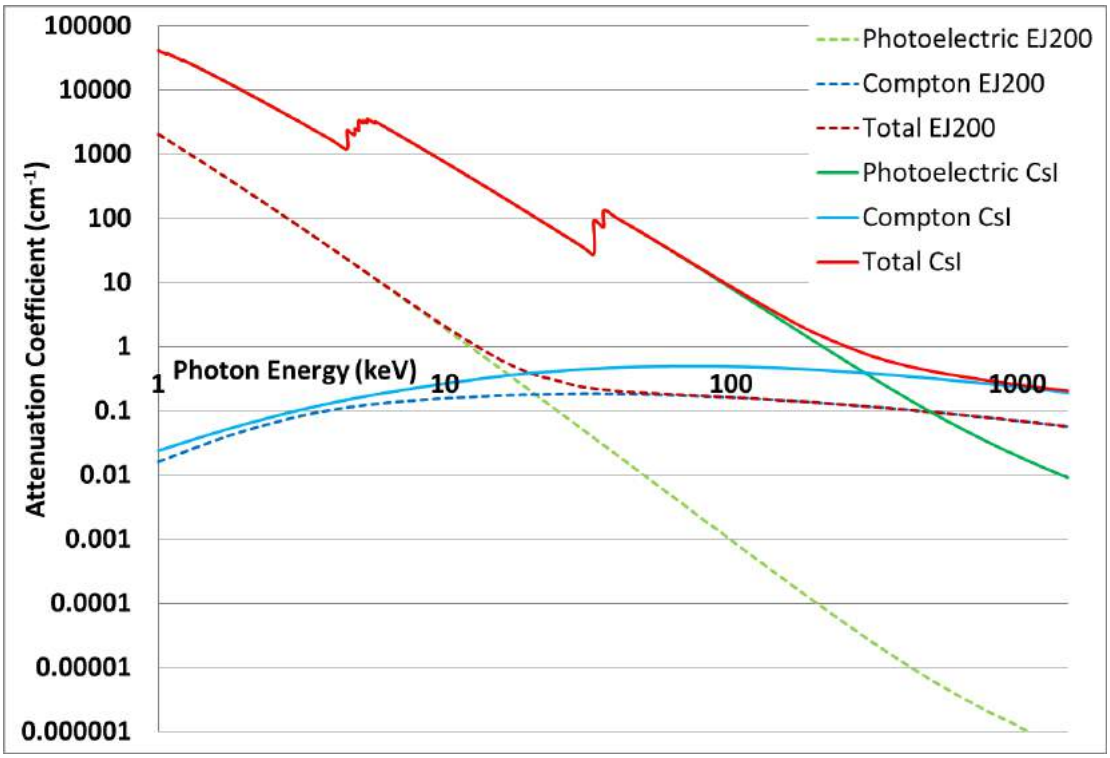

Figure 2.8: Gamma attenuation coefficients for CsI and EJ200 (NIST/Eljen).

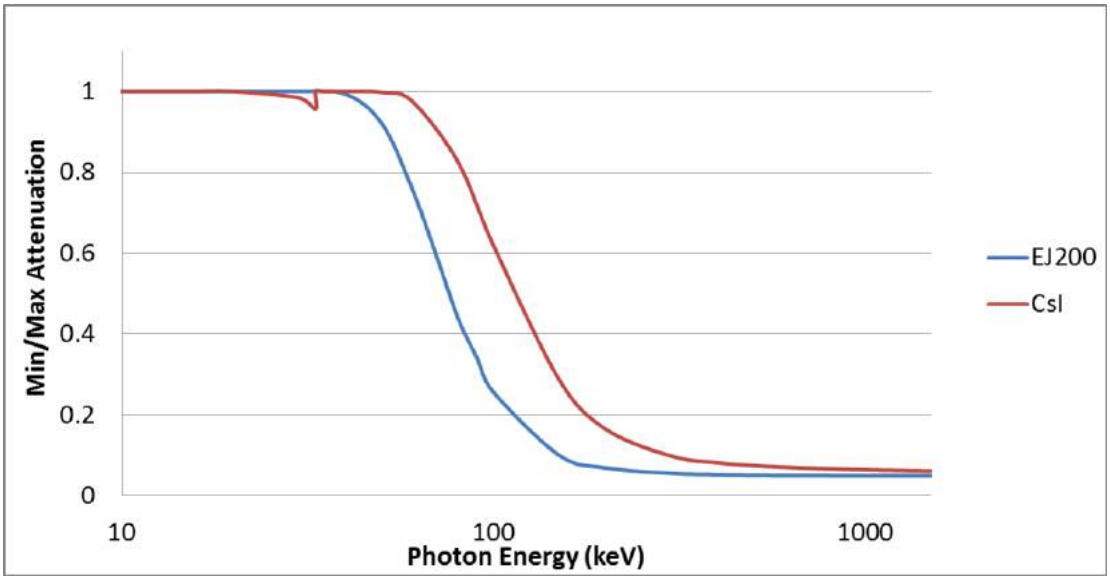

Figure 2.9: The ratio of attenuated photons for 0.5mmx100mmx100mm EJ200 and CsI scintillators in max. and min. positions, plotted against energy.

this energy all of the photons that are incident upon the detector are absorbed within the minimum, 5mm, thickness and reducing the energy further does not alter the proportion of events detected. As the incident energy is increased a greater proportion of photons pass directly through the detector at both the minimum, 5mm, and maximum, 100mm, thickness. This results in the proportion of events attenuated reaching a constant level,

and the shape of the response curves converging, above approximately 200 keV. A similar range is observed for CsI at slightly higher energies.

2.1.4 Errors Associated with Simple Model

The simple model, described above, simulates energy deposition within a single slab of homogeneous material rotating within a uniform parallel beam of monoenergetic photons.

This model provides an approximation of some of the major considerations to be made when designing a RadICAL detector. A number of other factors that are not covered by this model and may effect the performance are listed below:

- Multiple Scatter - The simple model assumes that all energy deposition occurs as the result of each photon depositing energy through an absorption or a single scattering event due to the use of a narrow beam attenuation coefficient. At lower energies, when photoelectric absorption is dominant, this approximation holds but as the energy is raised Compton scattering becomes more dominant and so the potential for each photon to interact multiple times within the detector becomes more significant and may effect the shape of the response curves. Compton scattering becomes the dominant photon interaction above approximately 20 keV for EJ200 plastic scintillator and above approximately 300 keV for CsI.

- Scintillation Light Collection - A major factor to be considered when mounting a photodetector to the surface of a scintillator is the exact position. In many traditional scintillator detection applications the detector is cut specifically to match the photodetector window in order to maximise light collection. For the geometry required by RadICAL this is not possible. A number of coupling techniques considered include coupling the photodetector directly to various positions on each detector face, using a light guide or mounting the photodetector away from the detector surface and reflecting scintillation light within a sealed enclosure. The relative merits of each of these techniques are not considered by the simple model.

- Scatter and Attenuation Effects - As well as depositing energy within the scintillator incident radiation will also inevitably be absorbed and/or scattered in the

detector housing and in any other materials introduced to the detection area as part of the system. These effects are difficult to model and could be significant , particularly for high-Z or complex detector housings.

- PSD Effects - There is evidence to suggest that the ability to discriminate neutron and gamma events, using Pulse Shape Discrimination, degrades as detector volume increases or its geometry moves away from that of a right cylinder [90]. This behaviour is not currently fully understood but may be due a large spread of optical photon pathlengths between their creation in an irregularly shaped scintillator to the photodetector. The geometry of the detector and the location of the photodetector should be investigated to minimise this effect when designing detectors for PSD.

- Background radiation - An inevitable factor to consider when designing detectors is the effect of various forms of background radiation. Fluctuations in background counts were assumed to be negligible for the purposes of this work and were not included in the model.

2.2 Monte-Carlo Simulations

In addition to the simple modelling, detailed in the previous section, a series of Monte-Carlo simulations were performed in order to investigate a wide variety of different factors, relevant to the final system design. These include complex geometry, multiple scatter and the production and transport of optical photons between the scintillator and the photodetector. All simulations of this type were conducted using Geant4 [91].

2.2.1 RadICAL Simulation

A basic simulation was initially conducted to compare the Geant4 code with the simple model described in Section 2.1. This involved modelling a parallel, uniform flux of 600 keV photons targeted at a 5mm x 100mm x 100mm CsI crystal. The crystal was rotated in uniform 3.6 degree steps as the photon beam covered the scintillator at an intensity of 600 photons per cm^2 per detector step. A visualisation of the simulation is shown in Figure 2.10 with incident gamma photons shown in green and photoelectrons shown in red. The Caesium Iodide properties were taken from the standard Geant4 material database. This defines the relative proportions of caesium and iodine ions within

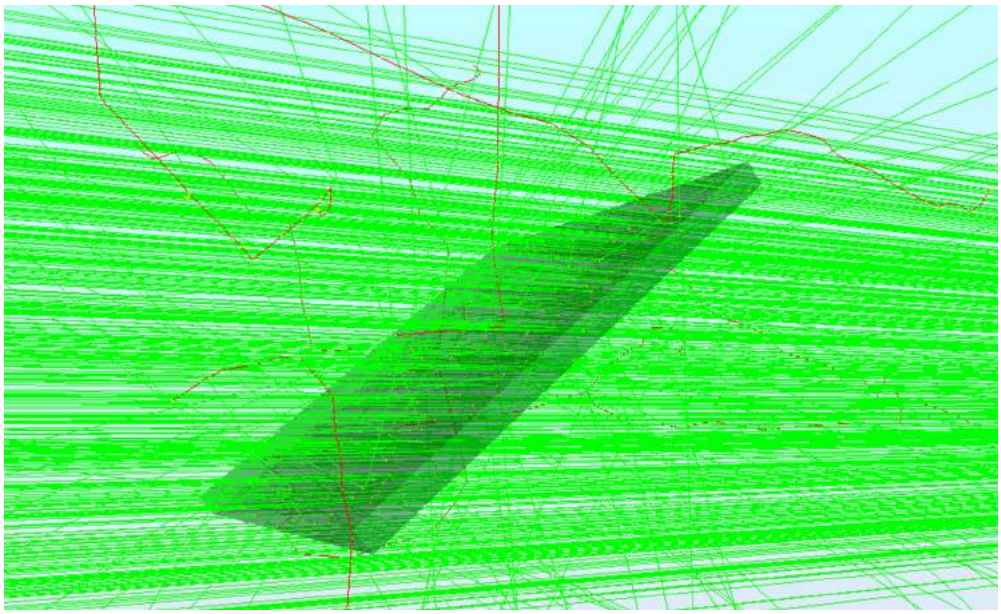

Figure 2.10: Visualisation of Geant4 simulation of CsI slab rotating in 600 keV photon beam.

the compound as well as its overall density and mean excitation potential. The basic 'G4EmStandardPhysics' physics list was used to define the interactions that occurred within the model.

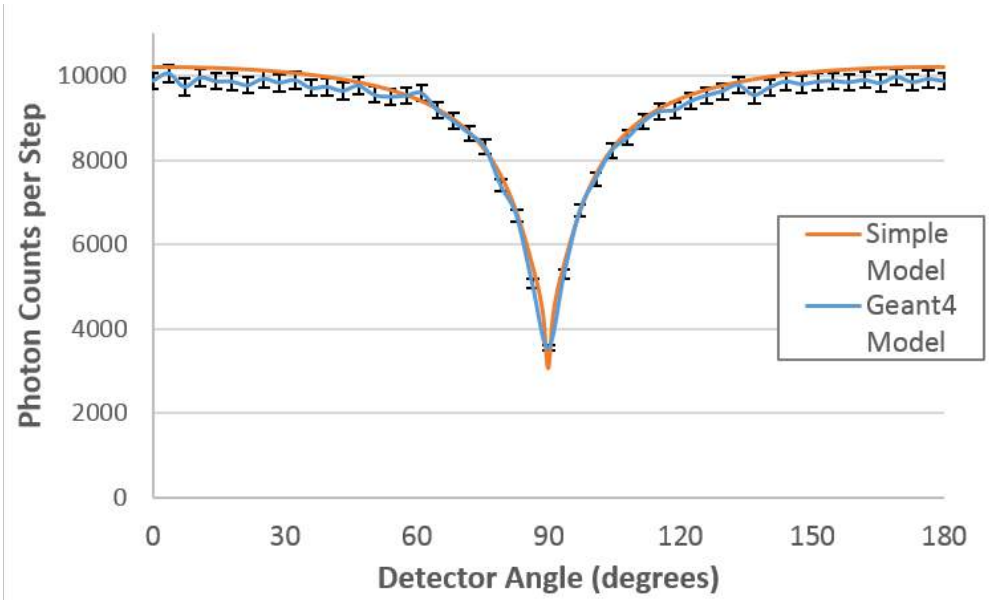

Figure 2.11: Comparison of simple and Geant4 model of rotating CsI slab exposed to 600 keV photons.

Each photon interaction, and the energy it deposited, was recorded. The total counts per step were plotted against the detector angle. These results were compared directly with those from the simple model and are plotted in Figure 2.11. It can be

seen that simple model and Geant4 simulation match closely. Poisson noise is shown for the Geant4 model results. The simple model overestimates the count rate slightly in the maximum (0 degree) position and underestimates the count rate slightly in the minimum (90 degree) position compared to the simulation. This difference may be due to multiple scatter.

2.2.2 Source proximity Investigation

The simple model described in Section 2.1 and the initial Geant4 simulation described in Section 2.2.1 both involved the attenuation of a parallel, homogeneous, beam of photons by the detector. This model could be assumed to be an accurate representation of a single photon source when the distance between the source and the detector is significantly greater than any of the scintillator dimensions. When the detector is positioned close to a point source two additional factors become increasingly important:

- As the detector rotates the distance between its nearest face and the source changes. The source is incident upon the same detector area but the flux decreases as $1/r^2$ and the solid angle increases as shown in Figure 2.12.

- The photon raypaths become increasingly divergent and pass across the surface of the detector and through the scintillator at angles different to those described in the simple model. This has the potential to alter the shape of response curve in a manner which could be problematic for source localisation.

These effects are more complicated to simulate using simple mathematical techniques so a Geant4 model was implemented to investigate this problem and determine a practical minimum distance at which a RadICAL detector could be effectively used.

Within the model a 5mm x 100mm x 100mm Cesium Iodide slab was again used as the detector and rotated, in discrete steps, around a central axis. The same material properties and physics lists were used as in the previous example. Photons of 600 keV were again used as the source but, in this case, they were directed isotropically from a single point. The photon source was positioned at a variety of different distances, from 50mm to 2m, from the axis of rotation and aligned vertically with the centre of the detector. In each position the detector was rotated 360 degrees and an acquisition was taken at each 2.5 degree step. A visualisation of this set up is shown in Figure 2.13.

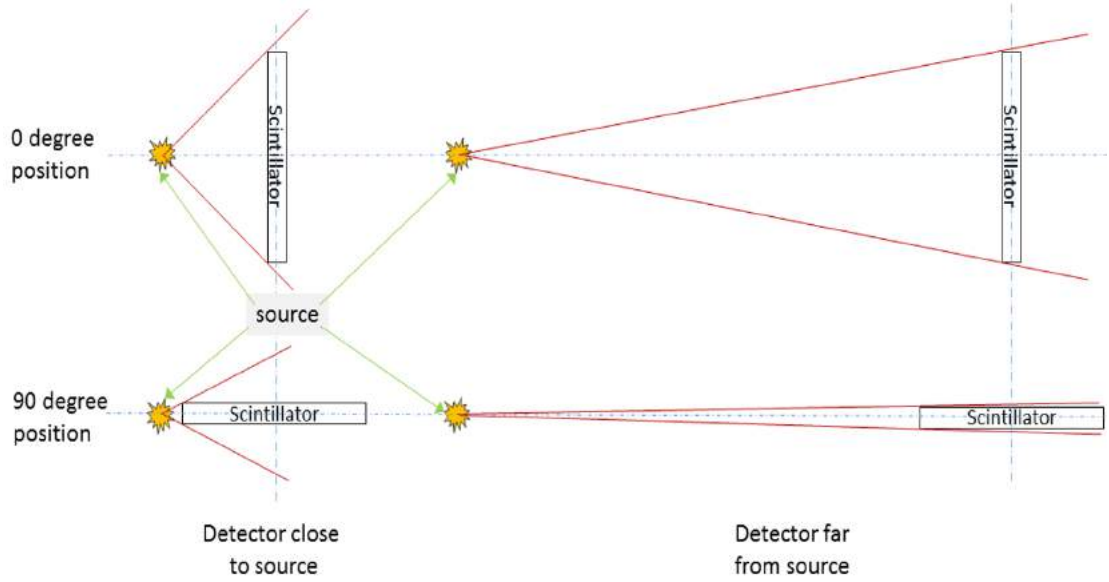

Figure 2.12: Difference in solid angle, marked in red, for detectors in 0 and 90 degree positions near, and close, to a point source.

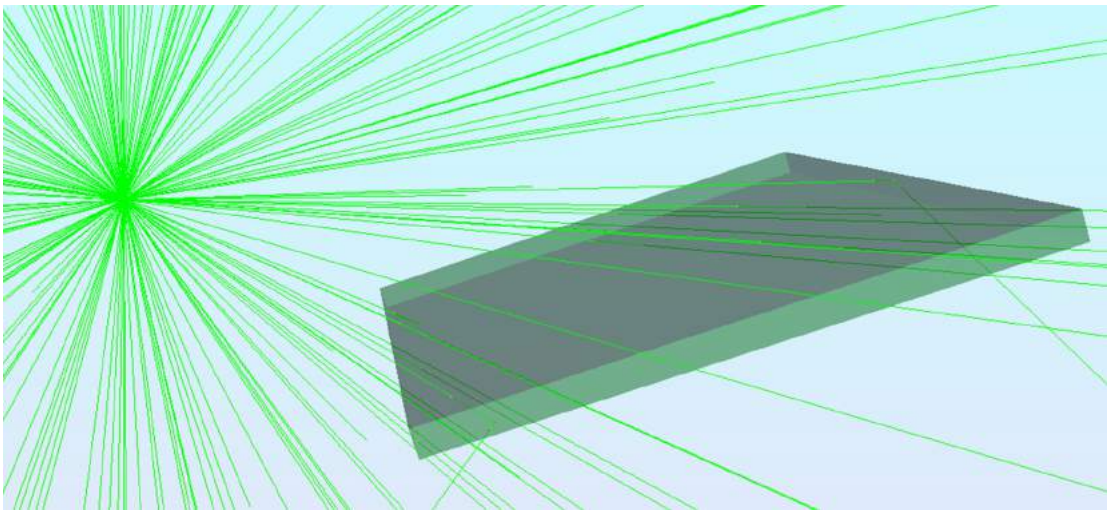

Figure 2.13: Visualisation of Geant4 simulation of rotating CsI slab exposed to isotropic 600 keV photon point source.

When the source was positioned 50mm from the axis of rotation 100,000 photons were released per detector step which resulted in an intensity of 1763 photons per cm^2 at the scintillator face when the detector was in the 0 degree position (large surface facing source). This simulation was repeated with the source in a variety of other positions between 50mm and 2m with the number of photons per step adjusted to keep the flux intensity consistent for each position according to the inverse square law.

Table 2.1 shows each of these positions and the corresponding events emitted by the source to maintain consistent statistics. Total detected counts in the 0 degree 'max-

Source to face distance (cm)	5	10	15	20	30	40	50	100	150	200
Total events	100k	400k	900k	1.6M	3.6M	6.4M	10M	40M	90M	160M
Counts 0 degrees	3077 ± 55	4288 ± 65	4845 ± 70	4999 ±71	5412 ± 74	5329 ± 73	5320 ± 73	5397 ± 73	5433 ± 74	5502 ± 74
Counts 90 degrees	6887 ± 83	2561 ± 51	2145 ± 46	2027 ± 45	1890 ± 43	1833 ± 43	1787 ± 42	1831 ± 43	1800 ± 42	1793 ± 42

Table 2.1: Source positions and corresponding count rates in 'maximum' and 'minimum' positions.

imum' and 90 degree 'minimum' positions are also shown.

Figure 2.14 shows a selection of response curves for this simulation, with the source positioned at different distances from the detector. It can be seen that at a distance of just 5cm from the detector the response curve is very different to the standard shape with a maximum peak, instead of the usual minimum, corresponding to the 90 degree position of the detector. As the distance of the source, from the detector, is increased, the standard response curve shape begins to appear with a smaller trough observed in the 0 degree position as well as the usual minimum at 90 degrees. At greater distances the 0 degree trough disappears completely and the standard response curve shape, as described in Section 2.1.1 becomes clear.

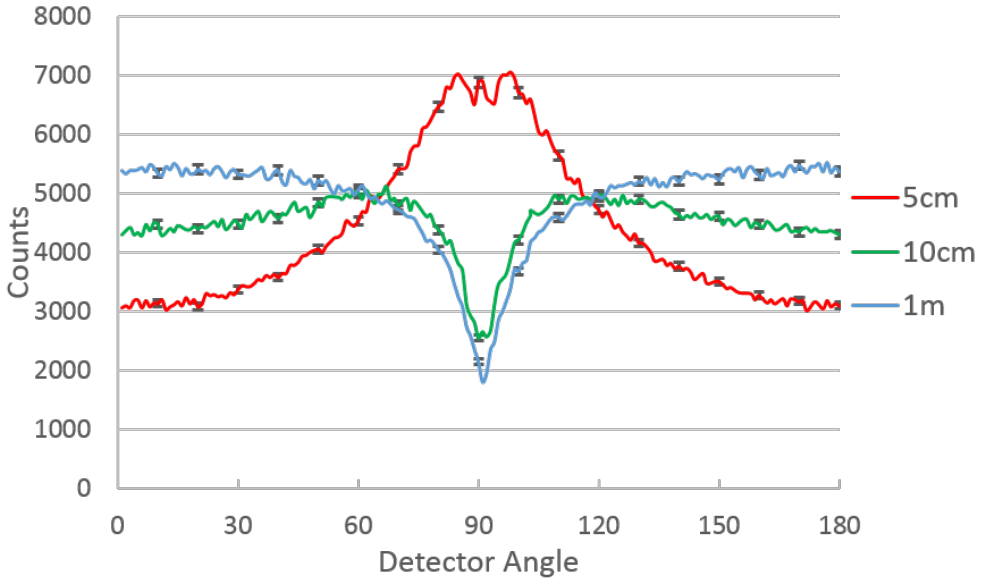

Figure 2.14: Simulation results for isotropic 600 keV source positioned at different distances from rotating CsI detector.

In order to compare these curve shapes count rates for the 0 degree and 90 degree

detector positions are shown in Table 2.1. In the 0 degree position the count rate is relatively low when the source is very close to the detector and then rises as the detector is moved further away and begins to level out at around 30cm. This is due to the photons pathlengths changing as they pass through the detector at different angles depending on the detectors distance from the source. In the 90 degree position the count rate is relatively high when the source is close to the detector but drops quickly as the detector is moved further away and levels out around 40cm. This is partly due to changing pathlengths but primarily due to the way that the edge of detector moves towards the source as it is rotated towards the 90 degree position. This increases the proportion of the solid angle that the source is incident upon, in accordance with the inverse square law, and so the count rate decreases as the source is moved away.

Figure 2.15 shows the ratio of photon counts in 0 degree and 90 degree positions as a simple demonstration of how the response curve shape changes as the source is moved away from the detector. It can be seen that this ratio initially rises drastically before levelling out at a relatively consistent level at distances of above around 50cm. This can be used as an effective minimum range for this geometry of detector. This is far less than the proposed detector position of 2.5m, from the source, described in Chapter 1.5.2.

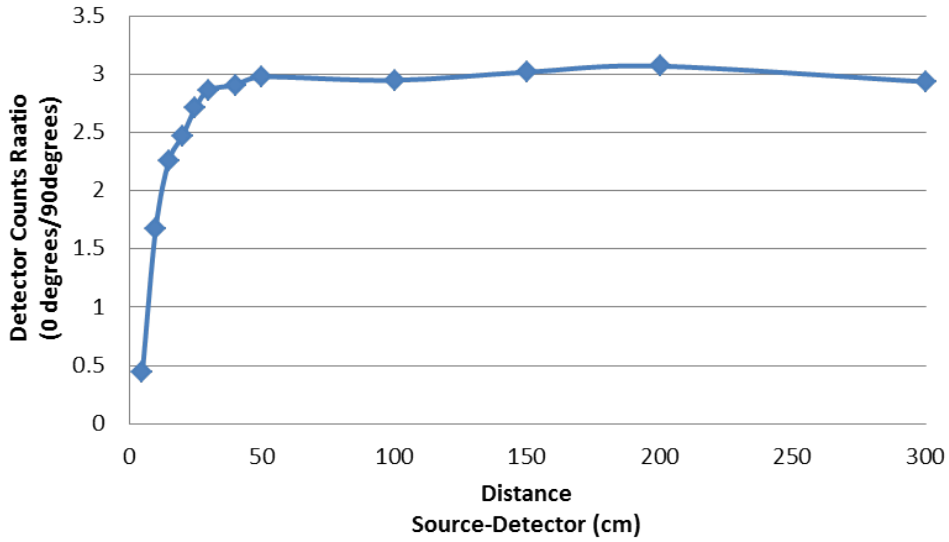

Figure 2.15: Ratio of detector count rates (0 degrees/90degrees) plotted against distance of source to detector.

2.2.3 Photodetector Position

Whilst a large quantity of modelling had been completed each of the simulations described already only considered the energy that was deposited by photons in a detector and not the scintillation process or the transfer of this energy, via the transport of optical photons, to the photodetector. The RadICAL detection concept, described originally in Chapter 1.6.1 features a rotating scintillator and so, for ease of manufacture, the photodetector was to be positioned away from the detector surface and scintillation light reflected within a sealed enclosure. For the RadICAL Stack detector, described in Chapter 1.6.2, a direct coupling was investigated.

In many simulation scenarios it can be considered adequate to model just the deposition of energy within the scintillator and may be preferable given the greatly increased processing requirements associated with simulating the transport of many optical photons for every scintillation event. However the shapes required for the RadICAL imaging technique may increase the probability of indirect pathlengths between the creation of an optical photon, through scintillation, and its detection by a photodetector. This has the potential to result in inefficient light collection and may also reduce the PSD capability of the EJ299-33 plastic scintillator that is to be used in the later stages of this project.

A major factor to be considered when mounting a photodetector to the surface of a scintillator is its exact position. In many traditional scintillator detection applications the detector is cut specifically to match the photodetector window in order to maximise light collection. For the geometry required by RadICAL this may not be possible and so an investigation was carried out into the ideal position for a photodetector to ensure efficient light collection.

A 20mm x 20mm x 100mm CsI scintillator slab was modelled using the same material properties as described in section 2.2.1. Two of the faces were split into equally sized 20mm x 20mm sensitive detector areas as shown in Figure 2.16 and all outer surfaces were covered with 2mm thickness of Barium Sulfate ($BaSO_4$), which is the main component of the diffuse reflective paint to be used in the final detector construction. Physical properties for the paint were determined using the 'G4BARIUMSULPHATE' material class. Optical properties were introduced to the model including the refractive index, absorption length, emission spectrum, scintillation yield and fast time constant

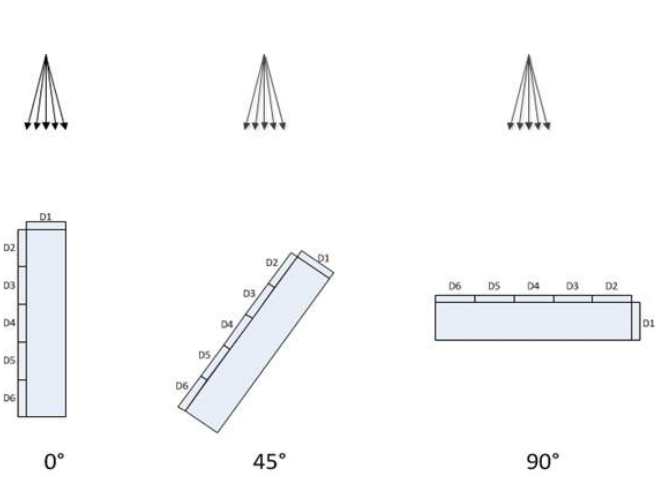

(a) Position of detector, including photodetector positions, relative to source, in each orientation.

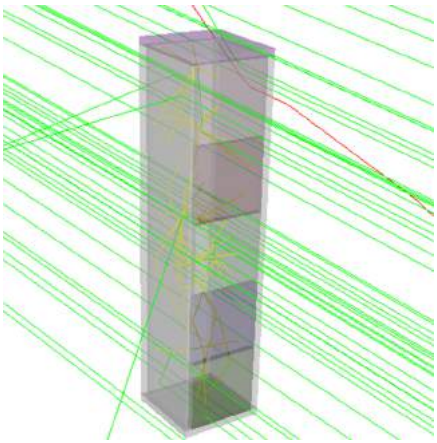

(b) Geant4 Visualisation of photodetector positions on rotating detector in photon field.

Figure 2.16: Model of rotating CsI detector with separate photodetector positions.

of the CsI and the refractive index and absorption length of the $BaSO_4$ coating. In addition to the standard EM physics list previously used an optical physics list was also introduced. This introduced boundary processes, absorption, and Raleigh scattering of optical photons to the model.

The detector was rotated in a uniform flux of 300 x 500 keV photons per cm^2 per 1 degree step for a total of 360 degrees as shown in Figure 2.16a. For each gamma interaction a number of optical photons, proportional to the energy deposited based on a scintillation yield of 41 photons per keV for CsI(Na), were created and travel around the scintillator until they reach the photodetector and a hit is recorded. Figure 2.16b shows a visualisation of this simulation with the detector in the 90 degree position. Photons are shown in green and optical photons are shown in yellow.

Figure 2.17 shows the results from this investigation. The best light collection is seen with the photodetector in position D1. This corresponds to the photodetector being positioned on the small end of the scintillator. This position also results in the most symmetrical response curve. The asymmetry of the response curve when the photodetectors are in different positions is a result of the longer pathlengths taken by the optical photons when the photodetector is positioned on opposite side of the scintillator to the gamma source. D2 and D6, in particular show a significant difference between their light collection depending on whether they are positioned towards the source, or away from it. Both of these factors point to the clear conclusion that a photodetector

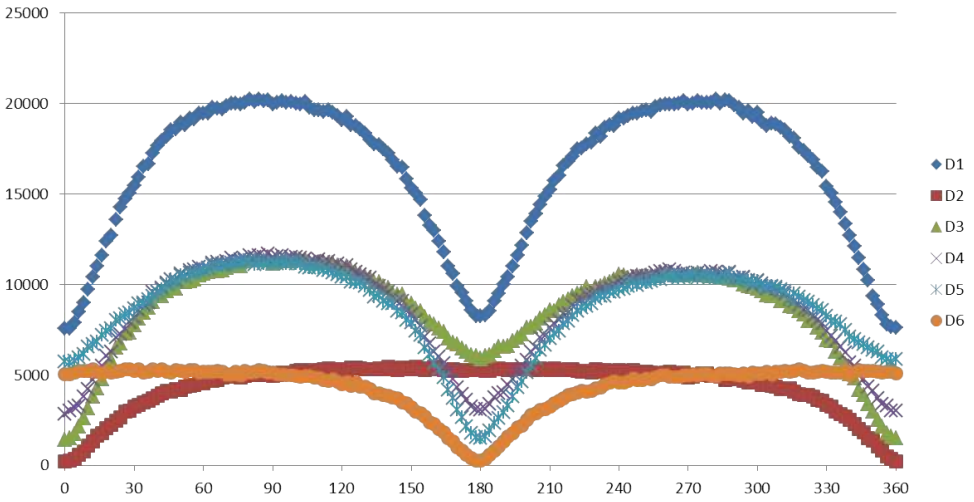

Figure 2.17: Optical photon counts per photodetector as detector rotates.

should be positioned at the end face for a scintillator geometry such as this.

2.3 Summary of Modelling

A simple mathematical model was created to investigate the RadICAL concept and considerations that should be made when choosing detector geometry and material. A Monte-Carlo model was created using Geant4 and used to validate the simple model. The two models were shown to agree closely and demonstrate that a RadICAL detector can be used to successfully determine the direction of a point source of gamma photons by building a characteristic standard response curve (SRC) as the detector rotates. The shape of the SRC was shown to be dependent on the detector geometry and material and the energy of the incident photons.

Further modelling was conducted, using Geant4, to investigate the creation and transit of optical photons from scintillation processes within the detector. This work was used to determine a technique for mounting a photodetector onto a scintillator that would optimise light collection and PSD capabilities. The results of these investigations were used to inform decisions made when building the detectors described in Chapters 3 and 4 of this thesis.

Chapter 3

RadICAL Detector

In order to validate the basic RadICAL concepts demonstrated by the models detailed in Chapter 2 a number of detectors were constructed. Each detector was then tested in a variety of situations and these results were compared to the modelled data.

3.1 Construction of the prototype RadICAL detector system

Three separate RadICAL detectors were built, each containing a scintillator slab of a different material or geometry. This allowed a variety of detector materials and geometries to be investigated and the models described in Chapter 2 to be validated. These detectors are detailed in Table 3.1 below.

Table 3.1: RadICAL Detector Overview

Detector		PMT	Minimum Step Angle (degrees)	PMT Base
Material	Geometry (mm)			
CsI (Na)	100 x 100 x 5	EMI 9531	0.072	Tapered voltage divider
CsI (Na)	40 x 40 x 3	ET 9956 B	1.8	Tapered voltage divider
EJ200 Plastic	140 x 150 x 12.7	ET 9390 B	1.8	Ortec DigiBASE

In most normal applications, where a photodetector is used to detect the light output from a scintillator, the photodetector is either coupled directly to the detector face using optical coupling gel with a refractive index similar to that of both surfaces or a light guide is used, with coupling gel, for the same purpose. This is to minimise the reflection that occurs between boundaries of the components and so maximise the quantity of the optical photons produced that reach the photodetector [93]. In the pro-

posed RadICAL setup this method of coupling introduces a number of problems such as attenuation of the signal by the photodetector and lightguide as well as practical concerns associated with rotating the photodetector and associated electronics. Instead the photodetector is mounted vertically above the rotating scintillator. Due to this unusual method of coupling a proportion of the optical photons produced by the scintillator may be lost as they are reflected between the scintillator surface, air, container edges and photodetector window. Each of the prototype detectors described in this chapter involve this method and their construction is described below.

3.1.1 RadICAL Detectors

3.1.1.1 Large CsI(Na) Detector Construction

The original RadICAL detector prototype was built using a slab shaped 100 x 100 x 5mm CsI(Na) scintillator from Hilger Crystals Ltd. This was rotated within a hollow plastic cylinder, internally painted with a diffuse reflective coating. The scintillator slab was rotated, in discrete steps, by a centrally positioned 12V stepper motor with a step angle of 1.8° and a 25:1 gearbox to allow initial acquisitions to be made with a step angle of as little as 0.072°. A 91mm photomultiplier (PMT - EMI model 9531B) was chosen due to its diameter matching the dimensions of the crystal and housing and its sensitivity to the wavelength of the scintillation light emitted by the crystal, as shown in Figure 3.1 [94] [95]. It was mounted vertically above to form a light-tight, reflective, enclosure in which the optical photons, created by scintillation processes in the slab, were reflected until entering the PMT window. Due to the hygroscopic properties of sodium doped caesium iodide it was necessary to vacuum pack the crystal between uses in order to minimise its degradation on exposure to moisture in the air. When exposed to air at room temperature and 50% humidity Cs(Na) has been demonstrated to not degrade notably for up to 40 hours. When exposed to 75% humidity the pulse height response has been shown to reduce to 50% in just 24 hours [96]. The detector was built for easy access to, removal and replacement of the crystal in order to simplify the process of minimising the crystals exposure to air.

The material used for the detector housing was 114.3mm outer diameter black PVC pipe with 4.9mm wall thickness. These dimensions allowed the detector to rotate with only a small clearance, to allow test sources to be placed as close as possible to the

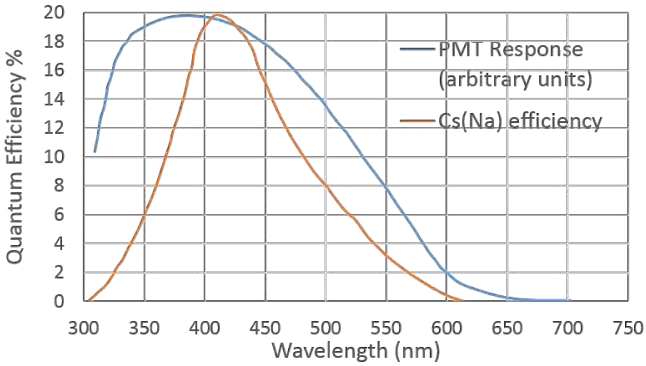

Figure 3.1: Spectral response of Electon Tubes PMT 9531B compared to emission spectra for CsI(Na) scintillator.

detector and minimise the volume within which the scintillation light is reflected. The 4.9mm wall thickness was chosen to be sufficiently thin to minimise the attenuation of the gamma photons being detected whilst maintaining enough thickness to minimise any problems associated with light penetrating the detector enclosure. An acrylic flange was bonded to the housing using a strong adhesive and this was used to secure the pipe to an ABS enclosure housing the stepper motor and gearbox. Black PVC tape was used seal up the gap and minimise light leakage through the flanged connection. A labelled diagram of this detector can be seen in Figure 3.2.

A tapered resistor network was built to provide a range of potential differences to the different dynodes of the PMT in order to accelerate and multiply the electrons ejected from the photocathode towards the anode where they can be read as a sharp current pulse as described in section 1.10. A circuit diagram of this setup can be seen in Figure 3.3. The circuit is tapered; the resistor values increase towards the anode. This is to overcome the space charge effect which can lead to non-linearity when dealing with high current pulses. The capacitors positioned between the final dynodes are used to ensure the transient signal charge required for pulse mode. This network was positioned inside the PVC housing and BNC and SHV connectors were used to connect the signal and high voltage power supplies respectively using coaxial cables passed through small holes in a rubber cap at the open end of the cylindrical housing.

The stepper motor was rotated using a 12V DC bench top power supply and controlled using a Greenwich Instruments RSSM2 driver card which is operated using 5V TTL pulses from National Instruments USB-6525 digital interface device.

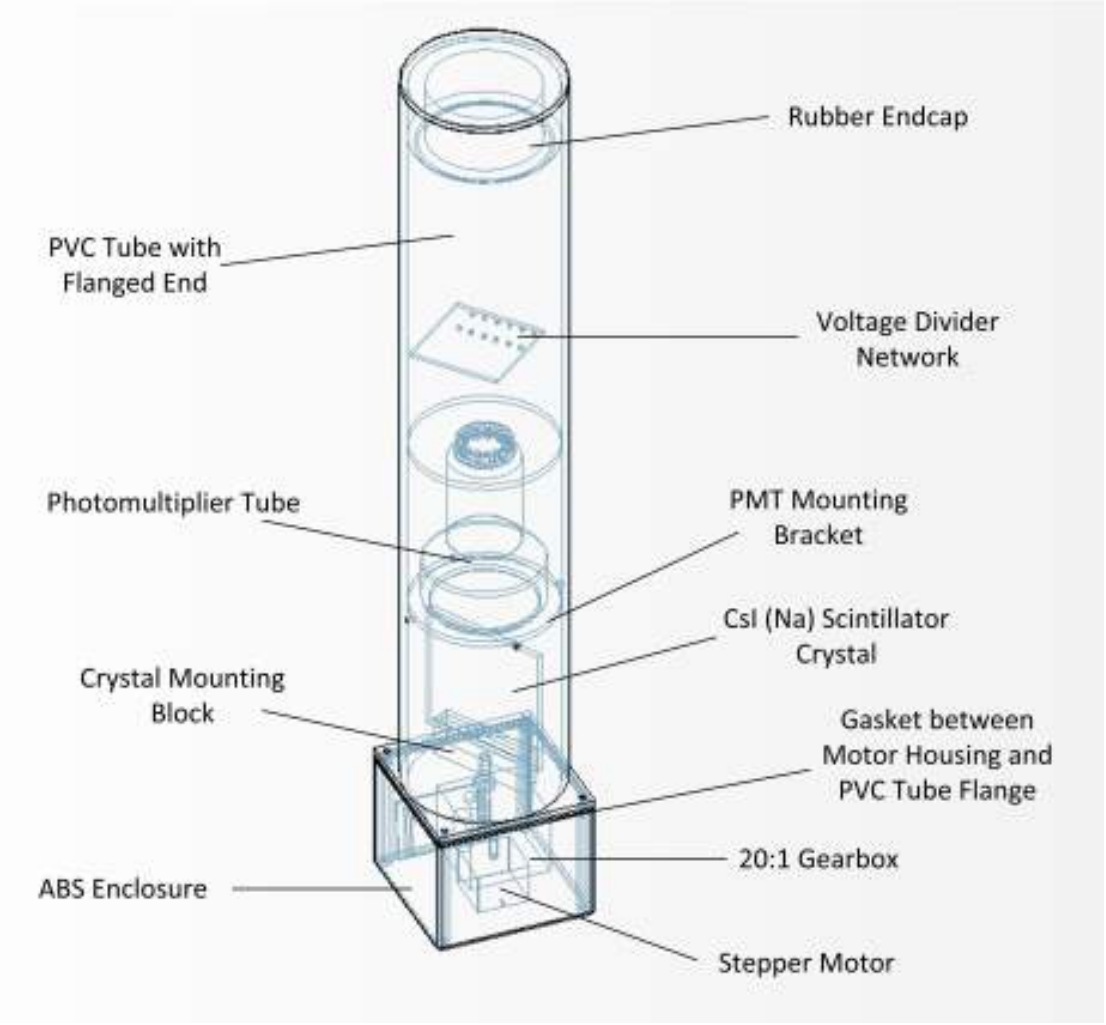

Figure 3.2: Labelled view of RadICAL detector 1.

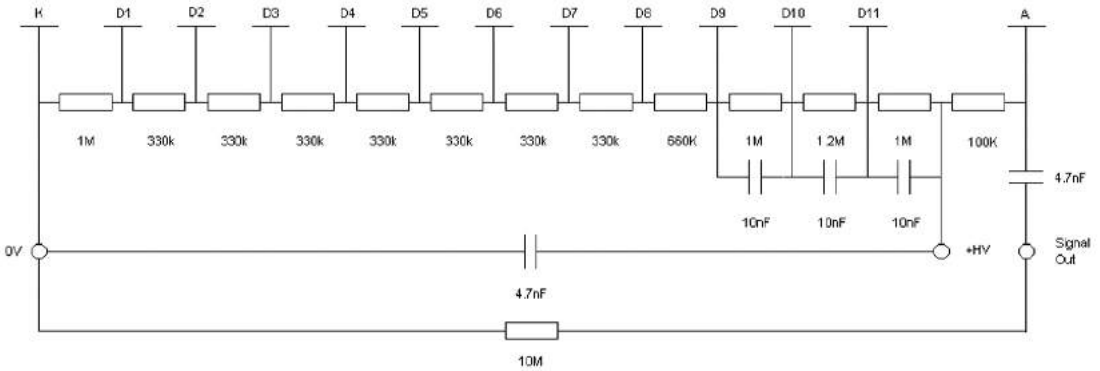

Figure 3.3: The tapered pulse mode voltage divider used in both CsI(Na) detector.

3.1.1.2 Small CsI(Na) Detector Construction

In order to further validate the modelled results a second, similar but smaller, detector was built. This detector was built around the same principles as the previously described model but with a smaller piece of scintillator - a 40x40x3mm piece of the

same CsI(Na) material mounted within a 60.4mm black PVC pipe. The same 12V, 1.8° stepper motor was used but the crystal mounting was secured directly to the motor shaft without the use of any gearing system. The same RSSM2 stepper motor driver and USB digital interface described earlier were used. An ET Enterprises photomultiplier 9956B was chosen as it's 51mm diameter covered the rotating scintillator and it is sensitive to the emission spectrum of CsI(Na) (350-550nm). A custom made tapered resistor network, similar to that described previously, was built to provide power to the dynodes and return a signal. All components were housed within two pieces of pipe and these were connected using a standard pipe fitting to allow the scintillator crystal to be removed and vacuum packed between uses to prevent degradation. Figure 3.4 shows an exploded detail view of this detector in two parts. The internal surfaces of the detector enclosure were painted with matt white paint to maximise the diffuse reflectance of light as it travelled between the scintillator and the photomultiplier.

3.1.1.3 Large Plastic Scintillator Detector Construction

Based around the concepts described above a further detector was constructed using polyvinyl toluene based plastic scintillator. A 140 x 150 x 12.7mm slab of Eljen EJ200 plastic scintillator was chosen due to its high light output, relatively low cost and emission spectrum close to that of commonly used photomultipliers as well as possessing similar properties to the Eljen EJ299 PSD plastic scintillator to be used in the final detection system. A further benefit of using plastic scintillator is that it does not possess hygroscopic properties like Caesium iodide (and other inorganic scintillators) and so can be permanently located within the detector system.

As with previous systems the scintillator was mounted directly onto the shaft of a 12V stepper motor and this was controlled using 5V TTL pulses to the same RSSM2 control card. A further mount was positioned opposite the motor shaft, at the top of the scintillator and used to secure it to a central bearing to minimise any lateral movement as shown in Figure 3.5. A thin aluminium cylinder was used to form the walls of the detector enclosure and all internal surfaces were painted using diffuse reflectance paint (Pro-Lite Spectraflect) to maximise internal reflection of scintillation light. A large (130mm diameter) photomultiplier tube (Electron Tubes 9390B) was mounted above the enclosure. An Ortec Digibase was plugged directly into the photomultiplier. This

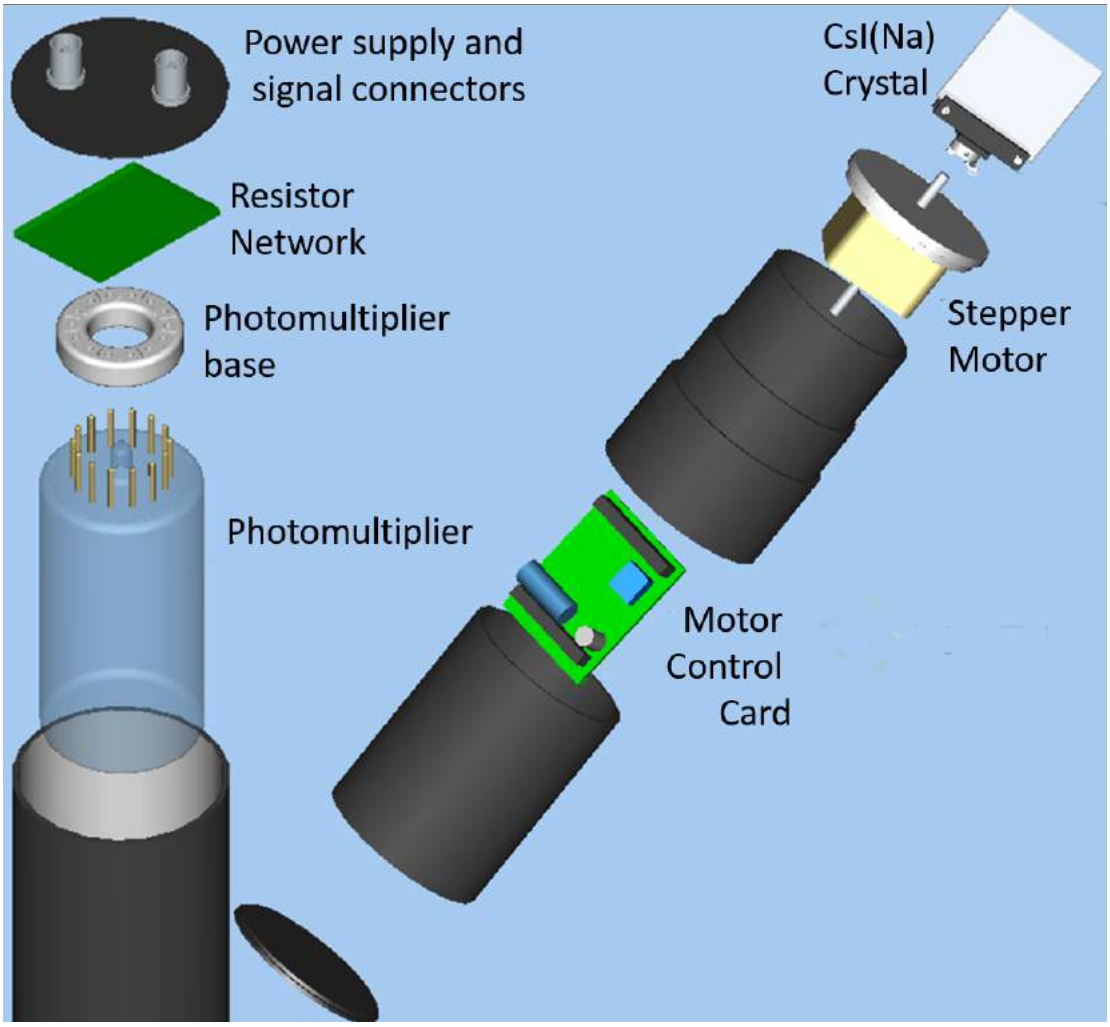

Figure 3.4: Exploded view of top and bottom sections of small CsI(Na) detector.

item runs from a single USB connection and replaces the voltage divider and HV power supply and includes a built in preamplifier and multichannel analyser which allows a digital output directly through the same USB.

The entire detector system was then enclosed entirely within a single length of 168.3mm diameter PVC pipe. The assembled detector, with the outer sleeve removed, is shown in Figure 3.5.

3.1.2 Control System and Data Processing

In order to determine directional information from the detector it was necessary to synchronise the data acquired by the system with the rotation of the motor so that individual pulses could be recorded and sorted into bins according to the position of the scintillator.

Figure 3.5: Large plastic scintillator RadICAL detector with outer sleeve removed.

3.1.2.1 Control System for CsI(Na Detectors)

For both of the CsI(Na) based systems, pulse data was fed directly from the voltage divider signal output through a pulse shaping amplifier (Ortec model 855) to a multi-channel analyser (MCA - Ortec model 927) which digitises the signal. Data from the MCA was then passed to a PC via a USB connection and was read as pulse information using the Ortec Connections-32 software suite. The same computer is connected, via another USB connection, to the USB digital interface device and used to control the movement of the stepper motor through a series of 5V TTL pulses. A flow chart of this complete set up is shown in Figure 3.6.

3.1.2.2 Control System for Large Plastic Scintillator Detector

The control system for the plastic scintillator system is similar to that described above, in Section 3.1.2.1. The major difference is that the high voltage power supply, voltage divider, preamplifier and MCA is replaced directly by the Ortec DigiBASE. This allowed the detector to run directly off USB without the need for any bulky auxiliary

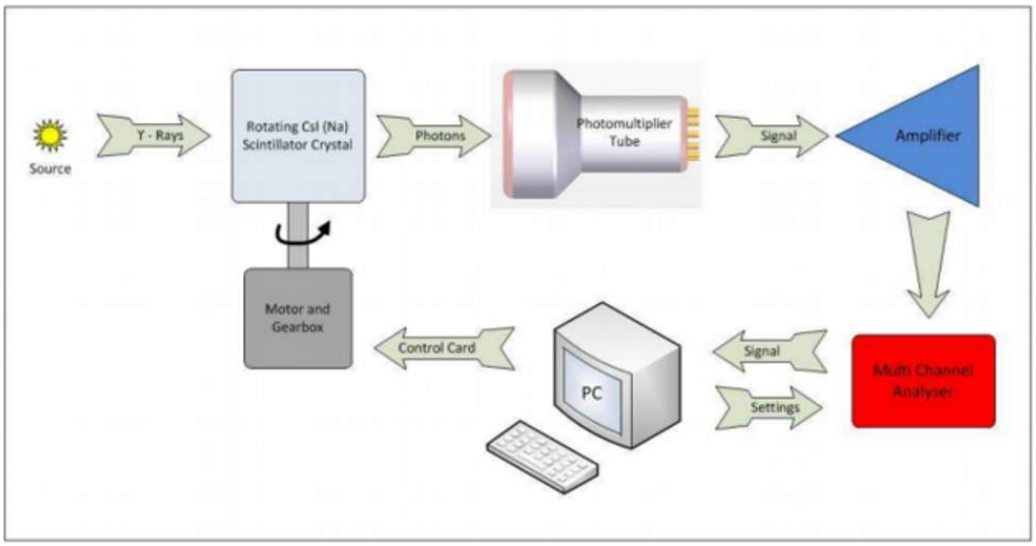

Figure 3.6: Flow diagram of entire system

equipment. The drawbacks associated with this method are a drastically reduced choice of photomultipliers, a smaller range of voltage and gain settings that can be used and an inability to process the information in an alternative mode, such as current mode (described later in this chapter).

3.1.2.3 LabVIEW Code

Each detector was controlled using variations of the same LabVIEW code, which was written specifically for this project.

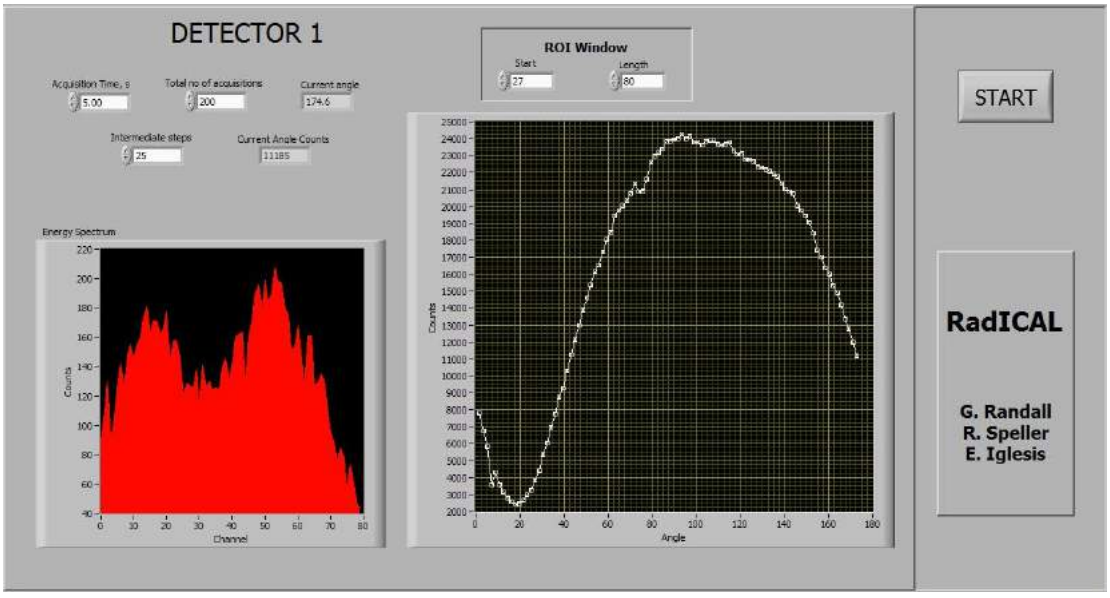

Figure 3.7: LabVIEW control screen showing the typical response curve on the right and the detected spectrum on the left.

This code provides pulses to the stepper motor controller to rotate the scintillator slab by a set increment. After each step, pulse data from the photomultiplier was acquired for a set period of time before the next rotation. A user interface was designed to allow different dwell times, angular increments and other operating parameters to be set the acquisition and storage of detected events. A further function was added for the user to pick upper and lower level discriminators to allow a specific energy window to be picked from a displayed spectrum. This was normally used to remove low energy noise. Whilst running, the code recorded and plotted integrated counts per step against the detector angle in order to build a characteristic response curve within the graphical user interface. Figure 3.7 shows the front panel of one variation of this code used in conjunction with the large CsI detector to detect an ^{241}Am source. After each run a complete set of data was saved in a .txt file. This consists of a two dimensional array with each row representing an energy window and each column representing a detector step. This data could subsequently be analysed to determine source information.

3.1.3 Detector Modifications for Current Mode Data Acquisition

Modifications were made to the original large CsI(Na) detector by an MSc student, Alexandros Alexandrou, under my close supervision in order to compare the function of the system in current mode. Current mode operation would allow a detector system to be run without the complicated electronics required to analyse individual pulses and so cut the overall cost of a system greatly. It would also prove advantageous in high flux environments where counting individual pulses becomes problematic.

The detector modifications involved a simplified resistor network with uniform resistance between each dynode and no decoupling capacitors and outputting the data into an oscilloscope where the changing light output of the system can be recorded in terms of a fluctuating voltage.

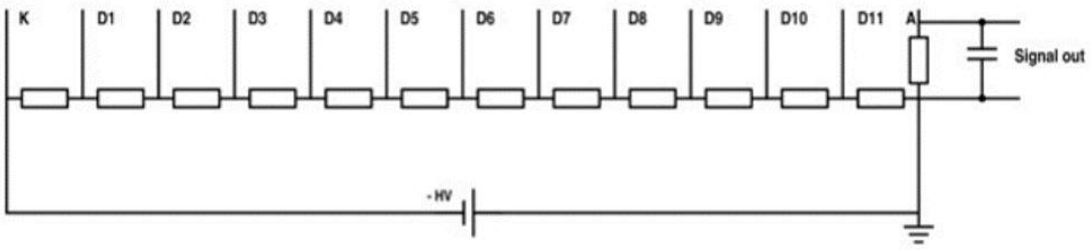

Figure 3.8: Linear voltage divider for use with large CsI detector in current mode.

Figure 3.8 shows this resistor network. All resistors in the circuit were 330 kΩ (as recommended by the PMT manufacturer). A capacitor is shown in parallel with the final resistor to form a resistor-capacitor (RC) circuit. This increases the response time of the detector depending on the resistance and capacitance values of these components and so the capacitor was changed, to minimise noise, according to the speed of rotation.

The same power supply was used to provide -1800V to the detector, via the new voltage divider, but the output was connected to a digital oscilloscope (Picoscope 3406A) so that the signal could be recorded.

The LabVIEW code was greatly simplified so that the motor was rotated at an effectively constant rate with equal steps of 0.072°. This resulted in a minimum time for a complete rotation of 25.0 ± 0.2 seconds. The detector output was saved separately for later analysis.

3.2 Performance Evaluation of RadICAL Detector System

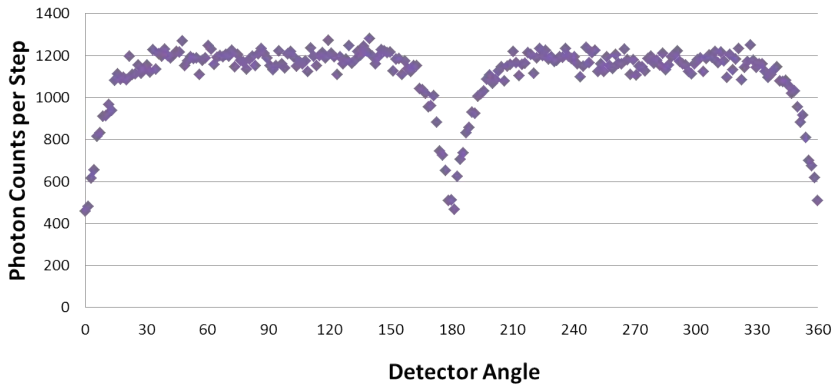

Figure 3.9: Example response curve to single 156kBq ^{137}Cs source 25cm away from detector.

The basic output from a RadICAL detector system is the characteristic curve of detector response as the scintillator is rotated as shown in Figure 3.9. This curve shape is known as the SRC (Standard Response Curve) and varies according to the experimental conditions (detector material, isotope used, etc.) but the primary result, i.e. source location, is always taken by finding the angular rotation that leads to the minimum point in the curve. This is because the fewest gamma photons are incident upon the detector when it is in the 0° position as shown in Figure 3.10. A number of experi-

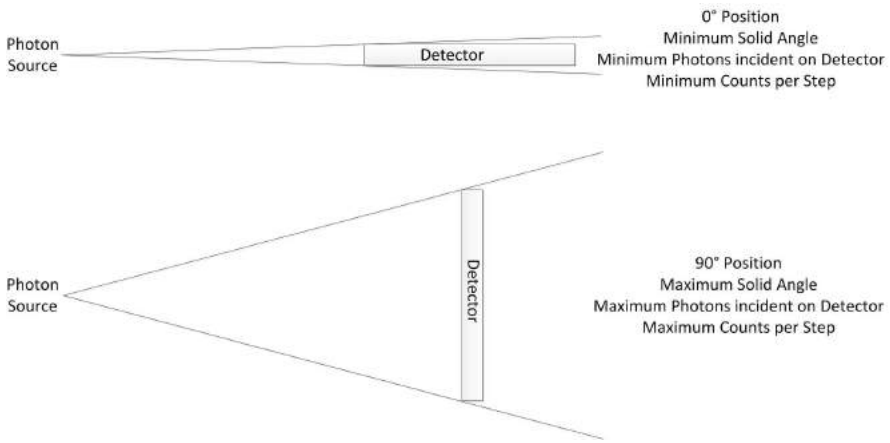

Figure 3.10: Example response curve to single 156kBq ^{137}Cs source 25cm away from detector.

ments were performed to evaluate the response of the RadICAL detector under various different conditions and to test the effectiveness of the models detailed in Chapter 2.

3.2.1 Determination of Source Location from SRC

A simple method of determining a source location from an SRC, like the one shown in Figure 3.9 is to pick the point with the lowest count rate and assume that this corresponds with the small faces of the crystal aligning with the direction of the source. Whilst this concept works in general it does introduce a number of errors:

- The accuracy of the determined direction of the source is limited to a discrete number of possible directions that correspond to each detector step.
- Noise can cause major inconsistencies when picking the minimum count rate.
- Ambiguity can exist when minimum count rates are present in multiple positions.

Instead the direction of the source was found from the following procedure:

- An initial minimum point was estimated from the lowest count recorded
- From this point two sets of recorded counts either side of this first estimate were then selected. The number of points chosen depended upon the scintillator, energy of the source and step angle but the important consideration was linearity of response in the region of the chosen points.
- To check this linear weighted least squares regression was used (the reciprocal of the standard deviations were used as weights) and the maximum number of points chosen before the R^2 value was reduced below 0.95

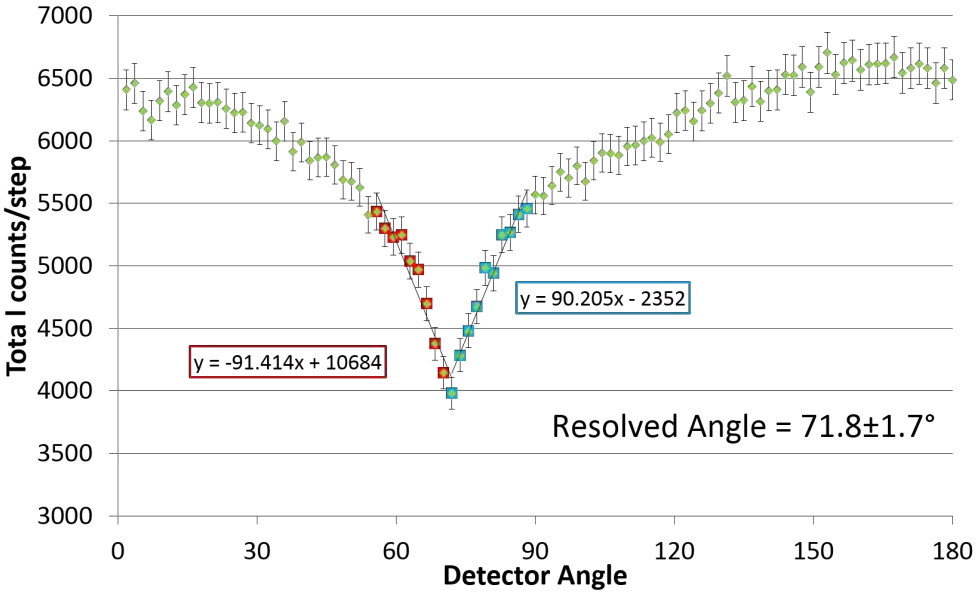

Figure 3.11: Example of source location method used for localisation of ^{137}Cs source.

- For the materials and sources used in this thesis a range of points up to 15° either side of the initial estimate of the minimum was found to satisfy these requirements.

- The point of intersection of the two lines of regression was chosen as the true minimum in the SRC.

Figure 3.11 shows an example of the improved method used for source localisation. This method was used throughout this thesis to determine the source direction from each SRC.

3.2.2 Determination of Performance Measures

In order to quantify and compare the performance of each detector a number of performance measures were determined. These were:

- Energy Resolution - This describes a detectors ability to recognise the energy of an event. It is determined by identifying a specific photopeak and finding its Full Width Half Maximum (FWHM). It is expressed as a percentage of the FWHM at a specific energy.

- Source Direction Accuracy - This describes how close the predicted source direction is to its actual value. In the case of the RadICAL detectors this is expressed in terms of an angle.

- Source Direction Precision - This is a measure of random errors around a predicted source direction and describes the repeatability of a measurement.

The energy resolution is largely dependent on the detector material and geometry. The accuracy and precision are dependent on the detector material, geometry, acquisition time and the position, energy and activity of the source.

3.2.3 Determining the SNR for further performance estimates

For each detector, performance measures have been determined. All measurements were made under similar noise conditions as defined by operating the RadICAL with a fixed SNR, determined by a specific acquisition time. This time was found in the following way. For each acquisition the 5x100x100mm CsI(Na) detector was stood upright, so that its rotation axis was vertical, and a source was positioned at a height that corresponded to the midpoint of the scintillator slab. The measured distance, x, was between the centre point of the source and the axis of rotation of the crystal as shown in Figure 3.12. A range of measurements were taken for different values of 'x'.

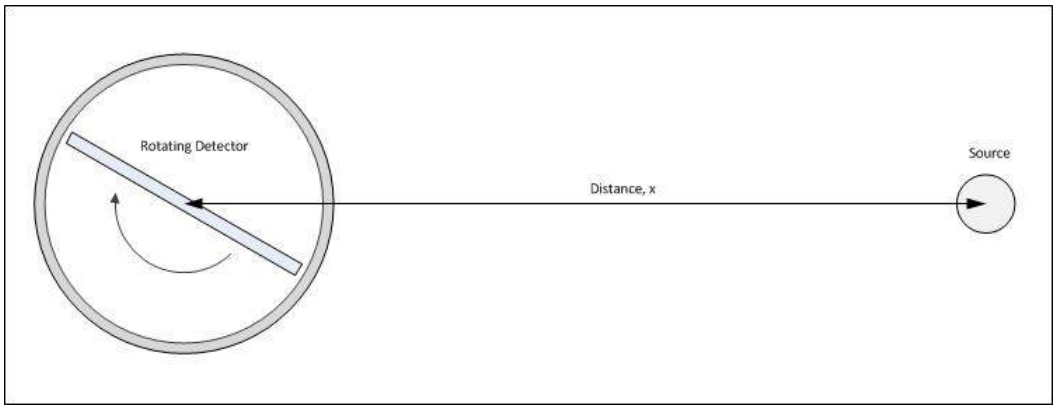

Figure 3.12: A simple plan of the detector setup.

An initial acquisition was taken using a ^{137}Cs source close enough to touch the outer casing of the detector (approx. 55mm from the axis of rotation) and the MCA was calibrated to the 662 keV photopeak. Each spectrum showed a large number of counts around the lower energy channels. A further spectrum was taken with no source present and the same high count rate was seen around the lower channels. This was considered to be low energy noise and an energy window was set with a lower level discriminator at channel 33 (58.6 keV) where there is a minimum point before the start of the low energy noise region of the spectrum. No upper level discriminator was set.

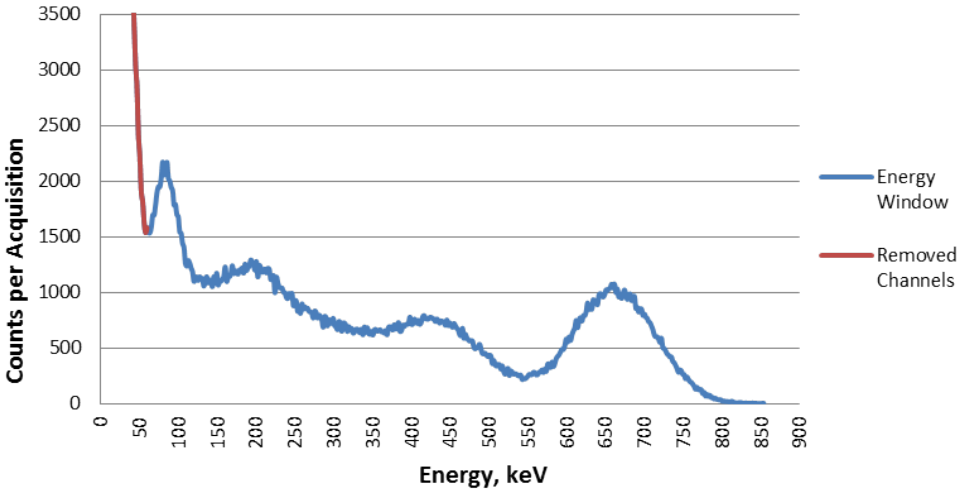

Figure 3.13: A ^{137}Cs calibration spectrum with the recorded window highlighted blue.

Figure 3.13 shows the calibration spectrum with the removed channels highlighted in red. In addition to the photopeak at 662 keV, to which the spectrum was calibrated, a Compton continuum can be seen including a Compton Edge at approximately 450 keV and a backscatter peak at approximately 180 keV. A further peak can be seen at approximately 75-80 keV due characteristic K-shell x-rays emitted when the photons interact with the lead shielding. Once set, the amplifier, voltage and window settings were kept constant for the duration of the experiment.

The signal to noise ratio was calculated as a physical measure of the sensitivity of the system in each case. This involved running 100 rotations of the detector for each value of 'x' so that a spread of counts could be determined for each detector angle. The SNR could then be determined by dividing the difference between the mean counts at the maximum (detector face on to source) and the minimum (detector end on to source) points of the overall signal by the noise [97]. This noise was determined as the standard deviation of the counts when the detected signal was at its maximum point. Figure 3.14 shows a graphic representation of how the SNR was calculated.

$$SNR = \frac{\mu}{\rho} \tag{3.1}$$

For each source position that was investigated SNR was calculated for a range of different acquisition times. In each case the minimum point was found by aligning the detector so that its 5x100mm side was facing the source, the live time was set to a fixed

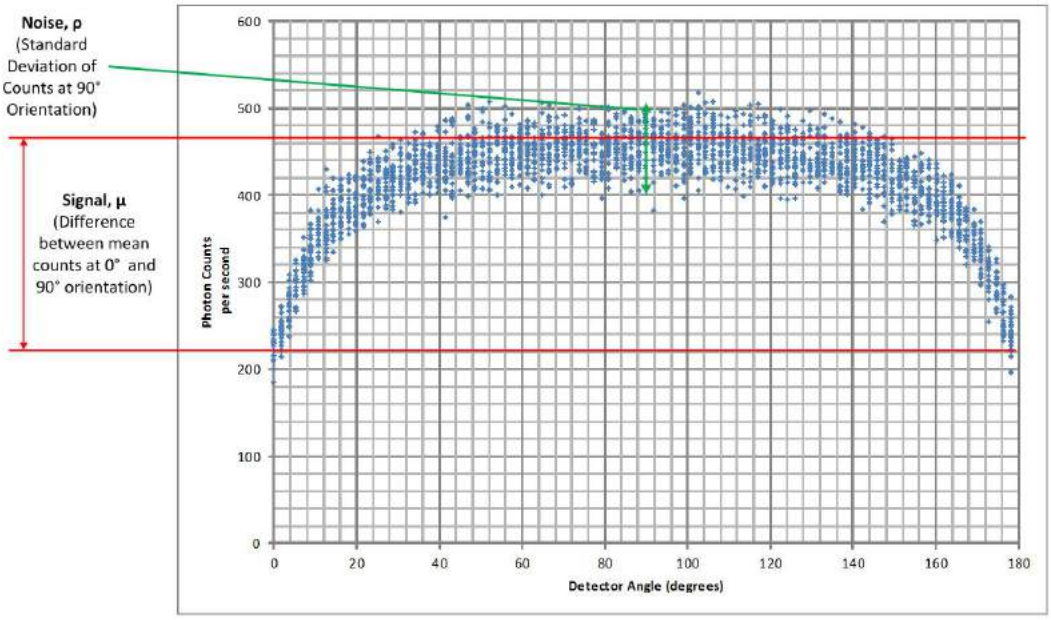

Figure 3.14: Example response curve with data used to determine SNR marked

value and 100 separate acquisitions were taken. This allowed a range of different SNRs between 5 and 20 to be demonstrated for counting times between 0.1 and 10 seconds per step. The detector was then rotated exactly 90° , by the stepper motor, and this process was repeated. The signal could then be determined as the difference between the mean count rates (s^{-1}) in each of the two positions. The noise was determined, for each position, as the standard deviation of the count rate. This value varies with the count rate as the detector rotates so was fixed as the maximum (face-on) position for the purpose of determining the SNR.

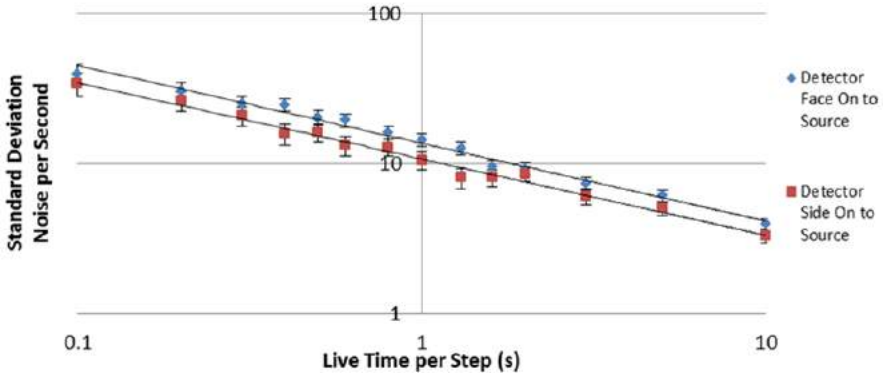

Figure 3.15: Standard deviation noise response to changing acquisition time used to determine SNR for 156kBq ^{137}Cs source 40cm away from the centre of rotation of the detector.

If the flux, on the detector, from the source is significantly higher than the back-

ground then it was predicted that the standard deviation of the count rate, in each position, should be proportional, and close in value, to the square root of the count rate itself. By plotting these noise values against the live time for several different acquisitions a clear power relationship becomes apparent to confirm this suggestion. One example of this is demonstrated in Figure 3.15. This can be used, by dividing the signal by this noise data as shown in Figure 3.14, to predict the live time required, per step, to maintain any chosen SNR. An SNR of 5 was used as an initial benchmark, with larger values of 10, 15 and 20 recorded for further comparison.

3.2.4 Detector Response to Different Flux Levels

A preliminary test was conducted to evaluate the sensitivity of the detector to differing levels of flux by measuring the response to a single 156kBq ^{137}Cs source in different positions, relative to the detector.

By using the method described above 14 different acquisition times, between 0.1 and 10 seconds per step, were investigated and the SNR was determined for each. The SNR was then plotted against the step time as shown, for when the source is 40cm away from the detector, in Figure 3.16. These values were plotted for 10 different source positions between 10 and 100cm from the detector. In each case a power relationship is observed between the SNR and step time and this trend could be used to predict the step time required to produce any chosen SNR.

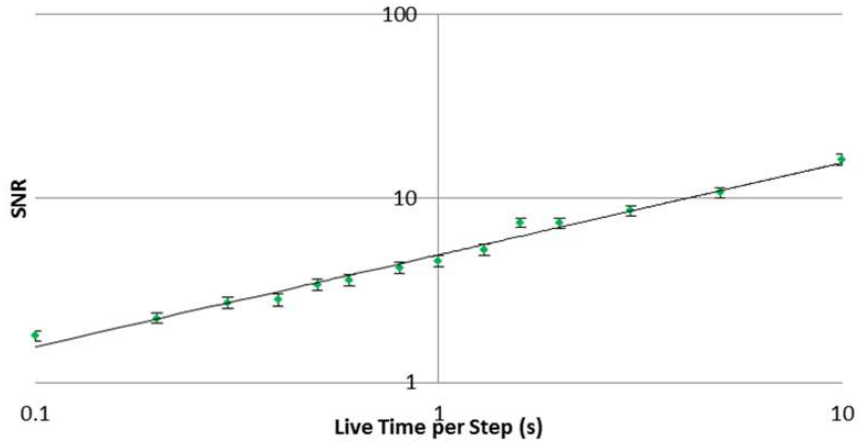

Figure 3.16: SNR response to changing acquisition time for 156kBq ^{137}Cs source 40cm away from centre of rotation of the detector.

The acquisition times required to achieve SNRs of 5, 10, 15 and 20 were determined and these were plotted against the distance of the source from the centre of the

detector. One of these plots, for SNR values of 5 and 20, is shown in Figure 3.17. It can be seen that there is a log scale relationship between the acquisition time required to maintain an SNR and the distance of the source from the detector. This is consistent with the statistics associated with the inverse square law.

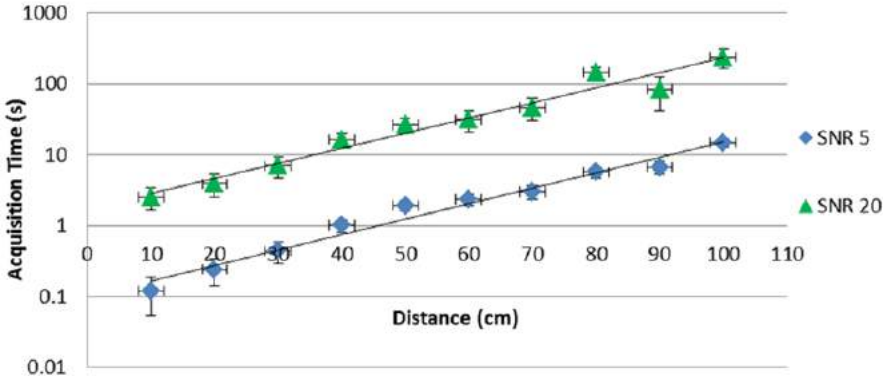

Figure 3.17: Plot of acquisition time required to maintain SNR values for 156kBq ^{137}Cs source as it is moved away from the detector

Once each of these acquisition times were determined a full 360° rotation was taken in each position so the respective curves could be compared with clearly defined SRCs. A step angle of 1.8° was used in all cases. Figure 3.18 shows SRCs for the detector exposed, at a distance of 40cm, to a 156kBq ^{137}Cs source with step times set at 1.02s and 16.52s for SNRs of 5 and 20 respectively.

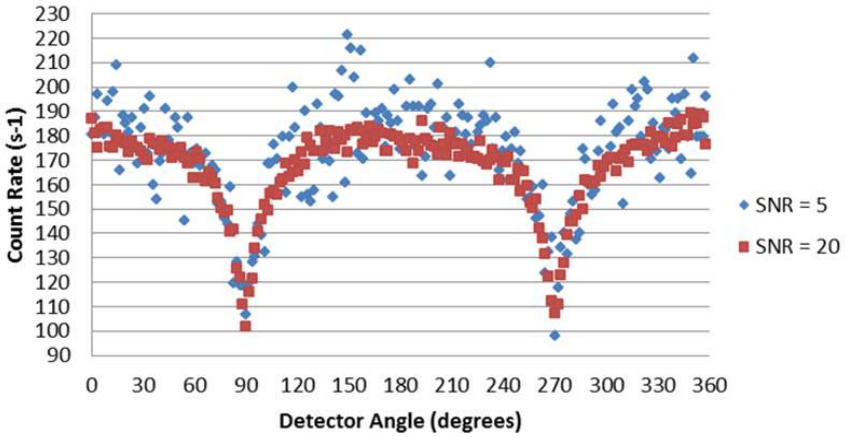

Figure 3.18: Standard response curves to 156kBq ^{137}Cs source, 40cm away from the detector. Live time set to 1.02s and 16.52s, per acquisition, for SNR of 5 and 20 respectively.

3.2.5 Comparison of SRC from Different Detectors

Acquisitions were taken with each of the three detectors described in Section 3.1 in order to compare the effect of detector materials and geometry on the shape of the SRC. In each case a ^{137}Cs source was positioned at a fixed distance from the centre of rotation and the detector was rotated a total of 360°. The setup for each acquisition was chosen to maximise the SNR of each SRC over a 14 hour acquisition. In each case an SNR of over 40 was achieved. These settings are shown in Table 3.2. The time stamp for the digitiser is quoted in nanoseconds and hence the error on the integration time can be considered negligible [98].

Detector		**Step Angle (degrees)**	**^{137}Cs Source Activity**	**Distance of Source to Axis of Rotation (cm)**	**Live Time per Step (s)**
Material	**Geometry (mm)**				
CsI(Na)	100x100x5	0.144	156	30 ± 0.5	20
CsI(Na)	40x40x3	1.8	156	30 ± 0.5	250
EJ200 Plastic	140x150x12.7	1.8	3280	50 ± 0.5	240

Table 3.2: Acquisition parameters for detector comparison.

Figure 3.19a shows the SRC results from the large CsI(Na) detector, described earlier in this chapter, exposed to a 156kBq ^{137}Cs source at a distance of 30cm over a period of 14 hours. The inclusion of a gearbox allowed for a far smaller step angle. A total of 2500 x 0.144° steps were taken in order to gain a greater understanding of the details of the response curve and a live time of 20s was acquired between each step. The spectrum was calibrated by fitting its photopeak to 662 keV. A lower level discriminator was set at 50 keV in order to cut out the low energy noise whilst losing a minimum number of events. The SRC is seen to descend from a maximum of approximately 9400 counts per step to a minimum of 4900. Figure 3.19b shows the corresponding energy spectrum with a clear photopeak at 662 keV as well as a clear Compton continuum of scattered events. An energy resolution of approximately 18-19% is observed at 662 keV.

Figure 3.20 shows the corresponding SRC and energy spectrum for the smaller CsI detector. The same ^{137}Cs source was used at the same distance as for the larger detector. The minimum possible step angle of 1.8° was used and the live time per step was increased to 250s to achieve the same total acquisition time for the 360° rotation.

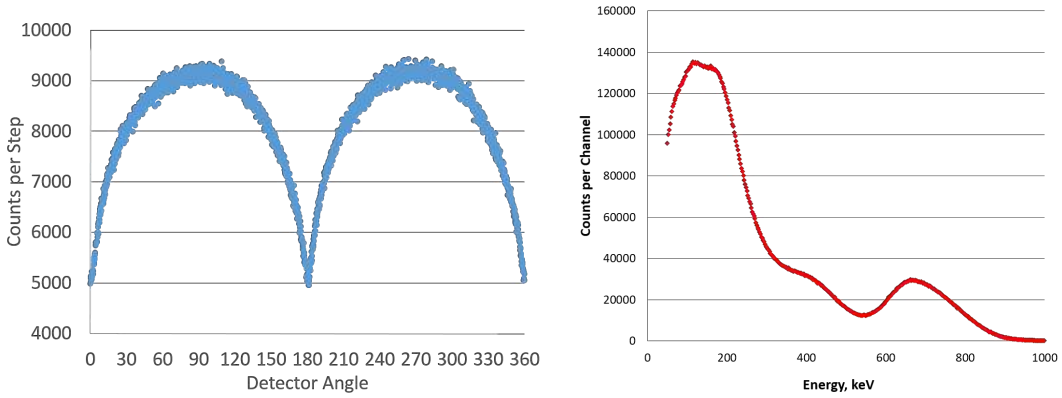

(a) Standard Response Curve. **(b)** Spectrum.

Figure 3.19: SRC and Energy Spectrum for Large CsI(Na) Detector Exposed to ^{137}Cs Source.

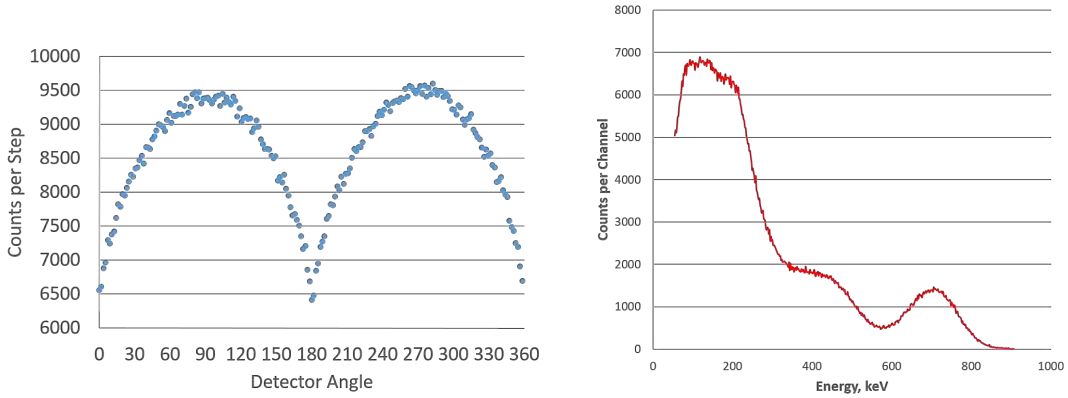

(a) Standard Response Curve. **(b)** Spectrum.

Figure 3.20: SRC and Energy Spectrum for Small CsI(Na) Detector Exposed to ^{137}Cs Source.

As in the previous results the detector was calibrated by fitting its photopeak to 662 keV and the lower level discriminator was again set at 50 keV to filter out low energy noise. An energy resolution of approximately 15-16% is observed at 662 keV in this detector. This is slightly lower than that seen in the larger CsI(Na) crystal. The difference may be due to the different geometry of each detector or because of deterioration of the crystals over time when exposed to ambient conditions. Both the SRC and the energy spectra can be seen to be broadly similar to the large CsI detector results. The SRC can be seen to drop from a maximum of approximately 9500 counts per step to a minimum of around 6500. This difference is less pronounced than is observed in the larger detector and be explained by a smaller aspect ratio of this scintillator (max/min dimension of slab).

Figure 3.21 shows the SRC and an energy spectrum for the EJ200 plastic scintil-

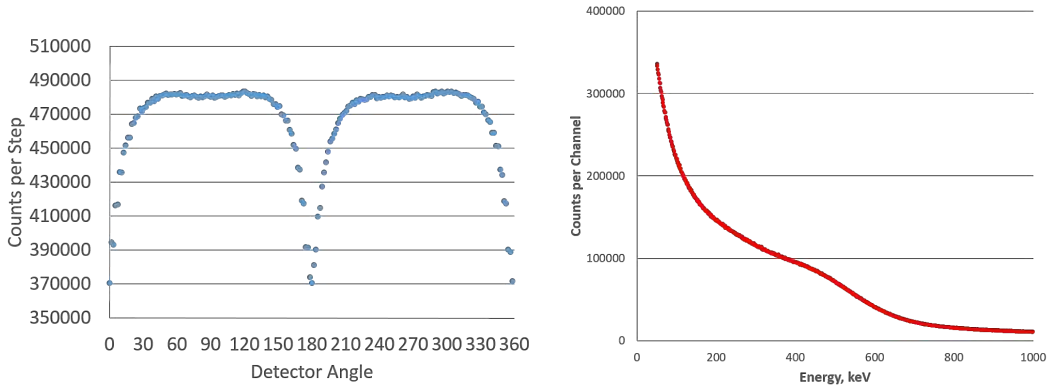

(a) Standard Response Curve. **(b)** Spectrum.

Figure 3.21: SRC and Energy Spectrum for EJ200 Plastic Scintillator Detector Exposed to ^{137}Cs Source.

lator detector. For this acquisition a larger, 3.28MBq, ^{137}Cs source was used. This was positioned 50cm from the central axis of the detector. A live time of 240s was used per step and the step angle was set to 1.8°.

The energy spectra for this detector is shown in 3.21b. At 662 keV virtually all energy deposition occurs through Compton scattering so no photopeak is seen. The plastic scintillator material also possesses very poor energy resolution so the only definition that can be seen in the spectrum is a poorly defined Compton edge. For 662 keV photons the Compton edge appears at 476 keV and, although calibration was not possible, this value was used to ensure that a similar range of energies were detected to those acquired by the CsI(Na) detector. The lower level discriminator was again set to 50 keV to cut out the low energy noise whilst retaining as many events as possible.

The SRC can be seen to maintain its maximum count rate for a greater spread of angles before descending sharply towards the minimum point. This contrasts directly with the smoother SRCs generated by the CsI detectors. This can be explained by the lower attenuation coefficient of the plastic scintillator allowing greater penetration of photons within the detector than occurs with CsI. In the case of CsI the value of μ in the 'μx' exponent is important. For EJ200 the x value is more dominant.

3.2.6 Comparison With Models and Discussion

The results for the acquisitions described in Table 3.2 were compared to modelled results described in Chapter 2.

Figure 3.22 shows the experimental results of the 5x100x100mm CsI(Na) detector,

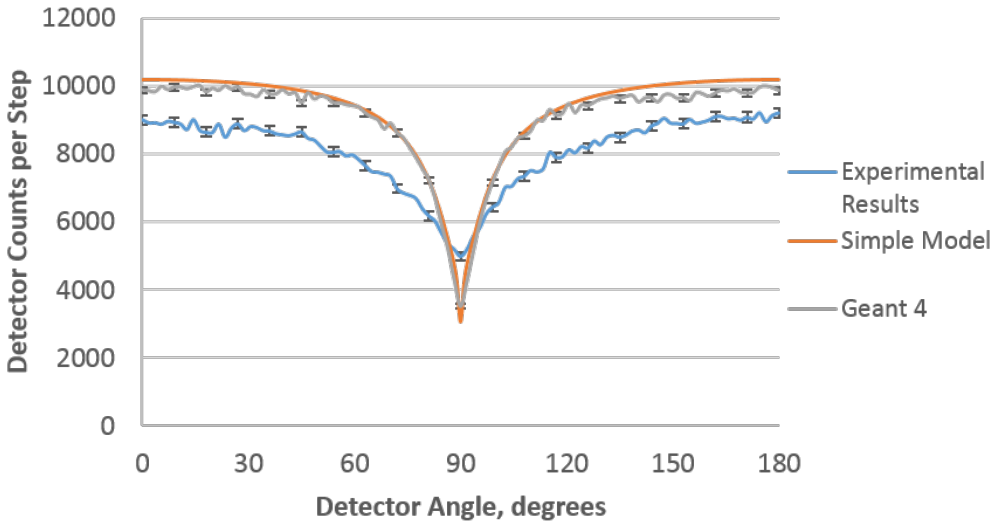

Figure 3.22: A comparison of the Geant4 model with detector results for a 156kBq ^{137}Cs source 30cm away from the large CsI(Na) detector with 20 second acquisition time per 1.8° step.

rotated in 0.144° steps and 20 seconds live time per step, exposed to a 156 kBq ^{137}Cs source 30cm away from the axis of rotation. This is compared to a simple model and a Geant4 model of the same detector and source geometry only. Both models were based on an equivalent flux of 662 keV photons. For the simple model this was based on a parallel beam covering the whole detector and for the Geant4 model it was based on photons emitted isotropically from a point source 30 cm from the centre of detector rotation. The Geant4 model is based on the 'G4_CESIUM_IODIDE' material properties from the Geant4 NIST compounds database and the same 0.144° step angle as seen in the experimental results.

Figure 3.23 shows a similar comparison for results from the 40x40x3mm CsI(Na) detector. As with the previous models the source was modelled as a parallel beam of 662 keV photons in the simple model and as an isotropic source of 662 keV photons, 30 cm from the centre of rotation, in the Geant4 model. The Geant4 model is based on the 'G4_CESIUM_IODIDE' material properties from the Geant4 NIST compounds database. A step angle of 1.8° was used in the Geant4 model to match that used in the experimental data.

Figure 3.24 shows a comparison for results from the 150x140x12.7mm EJ200 plastic scintillator detector. The source was again modelled as a parallel beam of 662 keV photons in the simple model and as an isotropic source of 662 keV photons, 50

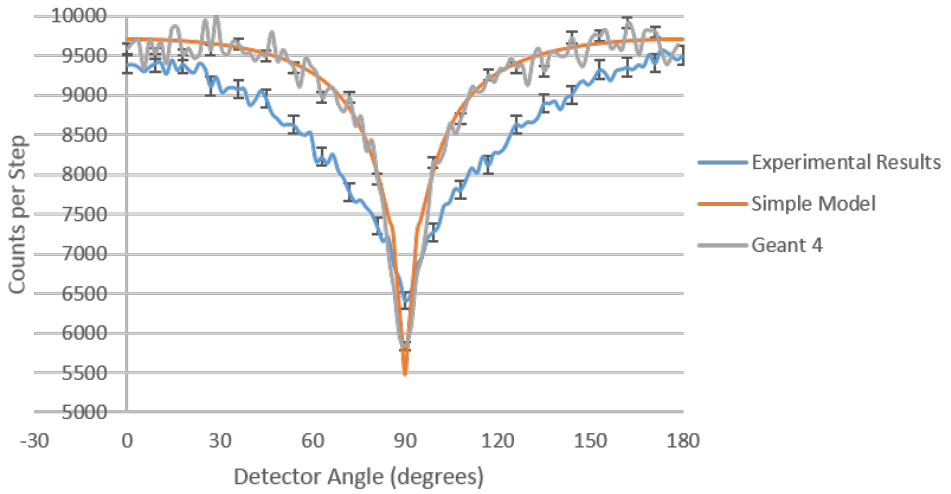

Figure 3.23: A comparison of the Geant4 model with detector results for a 156kBq ^{137}Cs source 30cm away from the small CsI(Na) detector with 250 second acquisition time per 1.8° step.

cm from the centre of rotation, in the Geant4 model. The Geant4 model is based on the 'G4_PLASTIC_SC_VINYLTOLUENE' material properties from the Geant4 NIST compounds database. A step angle of 1.8° was used in the Geant4 model to match that used in the experimental data.

It can be seen in each of the results that the simple model produces a very close fit to that of the Geant4 model. The experimental results demonstrate a similar shape to that seen in the models but in each case the count rate is less, than that seen in the models, in the 0° (maximum) position and greater in the 90° (minimum) position. The underestimation at 0° may be due to photons scattering away from the detector, poor detector efficiency or inefficient light collection. The overestimation, of around 30% of the total predicted signal, at 90° may be to do with photons scattering into the scintillator from the detector housing, other detector components or surrounding materials.

Further errors may have been caused by the detection of unwanted optical photons caused by background radiation and light leakage. Much of this background is a result of light penetrating the enclosure and reaching the photomultiplier due to the imperfect build of the detector. Further background radiation from other sources present in the laboratory was detected along with other common sources such as trace elements found in common materials, airborne radioactivity and cosmic radiation [38]. These errors are

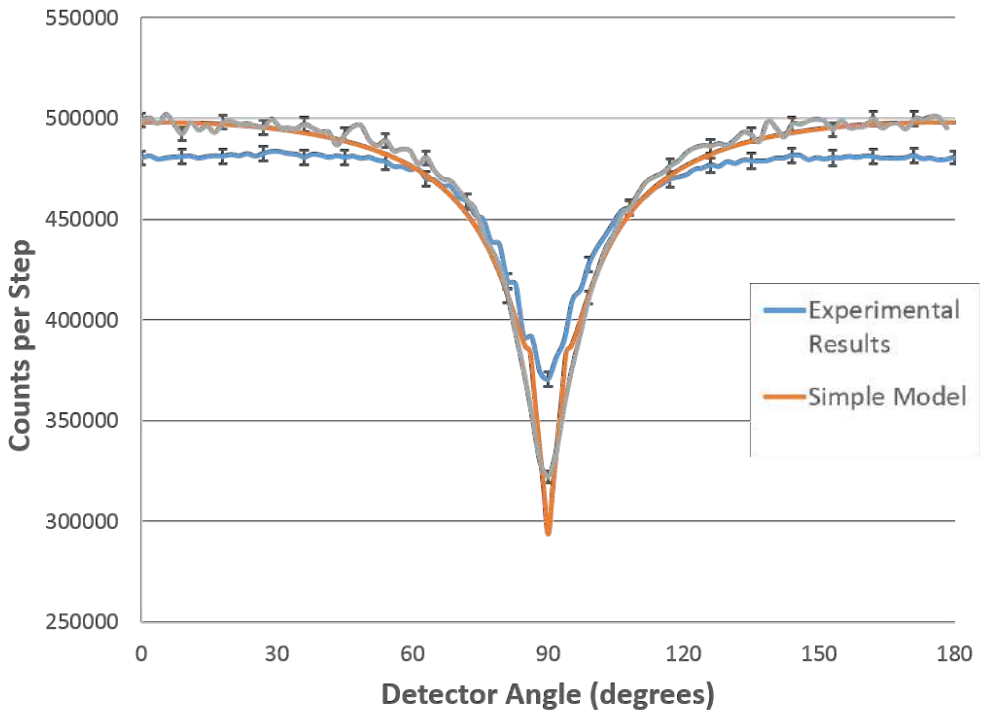

Figure 3.24: A comparison of the Geant4 model with detector results for a 156kBq ^{137}Cs source 30cm away from the EJ200 plastic scintillator detector with 240 second acquisition time per 1.8° step.

likely to add noise to the curve, rather than effect the overall shape.

3.2.7 Source location resolution

In order to determine the angular resolution of the detector it was necessary to compare the positions predicted by the Standard Response Curves (SRC) with the corresponding measured positions. This involved positioning the detector upright in the corner of a large warehouse and moving a single 500MBq ^{137}Cs source between a number of fixed positions within a 7 x 13 meter area, as shown in Figure 3.25a. Each source position was measured, relative to the detector, to within the nearest 5cm.

For each source position the detector was run for 200 separate 1 second acquisitions at a $1.8 \pm 0.02°$ step angle, resulting in a complete 360° rotation per source position. The detector angle that resulted in the minimum count rate was used to predict the position in each case using the method described in Section 3.2.1. These results are plotted in Figure 3.25b.

Source locations were measured to the nearest 5cm and the corresponding angle, from the detector was considered accurate to within 1.3° depending on the distance

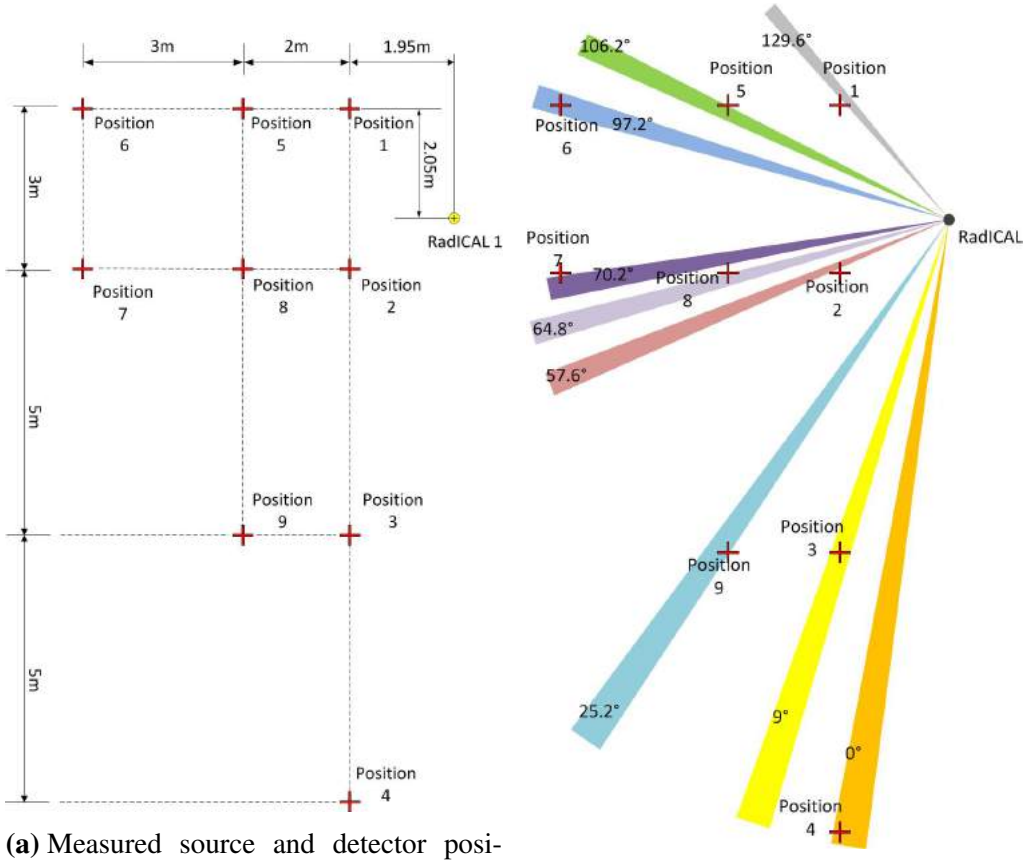

(a) Measured source and detector positions.

(b) Measured and detected positions.

Figure 3.25: Positions and results of large area localisation of 500MBq ^{137}Cs source.

from the source. The detector was considered accurate to within the nearest acquisition step of 1.8°.

Position	Distance to Source	Predicted Angular Location	Measured Angular Position	Difference
1	$2.83 \pm 0.05m$	$129.6 \pm 0.9°$	$127.2 \pm 1.0°$	$2.40 \pm 1.3°$
2	$2.17 \pm 0.05m$	$57.6 \pm 0.9°$	$54.8 \pm 1.3°$	$2.80 \pm 1.6°$
3	$6.26 \pm 0.05m$	$9.0 \pm 0.9°$	$8.92 \pm 0.5°$	$0.08 \pm 1.0°$
4	$11.12 \pm 0.05m$	$0 \pm 0.9°$	$0.87 \pm 0.3°$	$0.87 \pm 0.9°$
5	$4.45 \pm 0.05m$	$106.2 \pm 0.9°$	$108.2 \pm 0.6°$	$2.00 \pm 1.1°$
6	$7.25 \pm 0.05m$	$97.2 \pm 0.9°$	$97.2 \pm 0.4°$	$0.00 \pm 1.0°$
7	$7.01 \pm 0.05m$	$70.2 \pm 0.9°$	$72.99 \pm 0.4°$	$2.79 \pm 1.0°$
8	$4.06 \pm 0.05m$	$64.8 \pm 0.9°$	$67.25 \pm 0.7°$	$2.45 \pm 1.1°$
9	$7.14 \pm 0.05m$	$25.2 \pm 0.9°$	$24.35 \pm 0.4°$	$0.85 \pm 1.0°$

Table 3.3: Comparison of detected and measured positions using 500MBq ^{137}Cs source over 13 x 7m area.

Table 3.3 shows each measured source position and its corresponding predicted position, taken from the detector. The differences are shown and the mean of these

differences is $1.58 \pm 1.12^{\circ}$. Greater resolution may be possible given a smaller step angle or longer acquisition time.

3.2.8 Two Dimensional Source location resolution

A further test was conducted, within the UCL laboratory, to locate a source within a 2 dimensional plane using 2 separate detectors. For this experiment the two CsI(Na) detectors described in Section 3.1.1 were used to detect a 3.28MBq ^{137}Cs source.

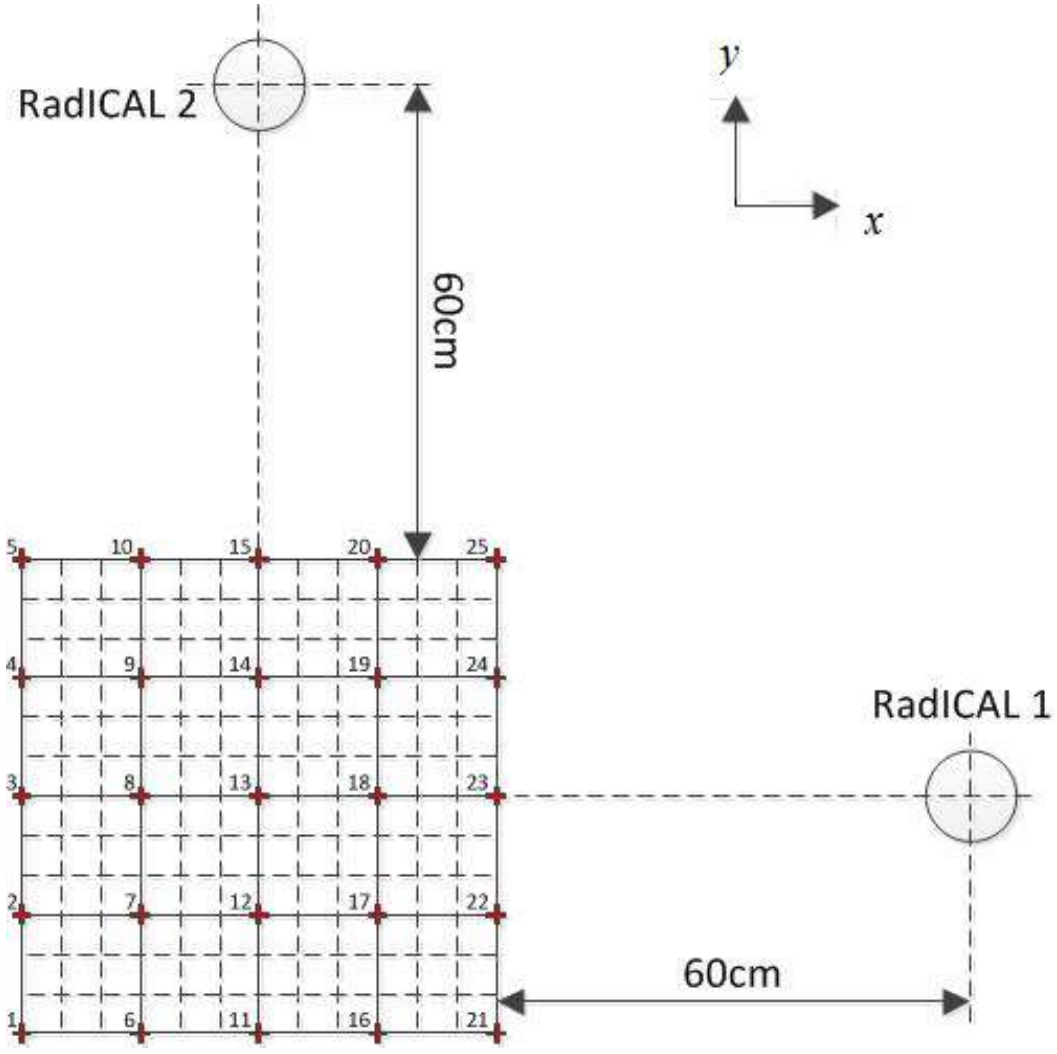

Figure 3.26: 2D source mapping - detector locations.

25 source positions were mapped onto a flat surface in a 5 x 5 grid. Each position was equally spaced, 15cm apart, resulting in a total detection area of 60cm x 60cm. The two RadICAL detectors were placed with their axes of rotation vertical and were positioned 60cm away from perpendicular edges of the detection area as shown in Figure 3.26.

The directionality of the detectors were calibrated by positioning the ^{137}Cs source in the centre of plan (Position 13 in Figure 3.26) and taking a long acquisition of 200 x 1.8°, 20 second steps, with each unit and finding the minimum point using the method described in Section 3.2.1.

Once the detectors were calibrated the source was placed in Position 1 and both detectors took acquisitions using a step angle of 1.8° and a live time per step of 1 second for a total of 200 steps (360°). The source was then moved to Position 2 and the acquisitions were repeated. This process was then repeated for each of the 25 positions and a response curve was saved in each case. The entire process was then repeated with 3 seconds of live time used for each detector step.

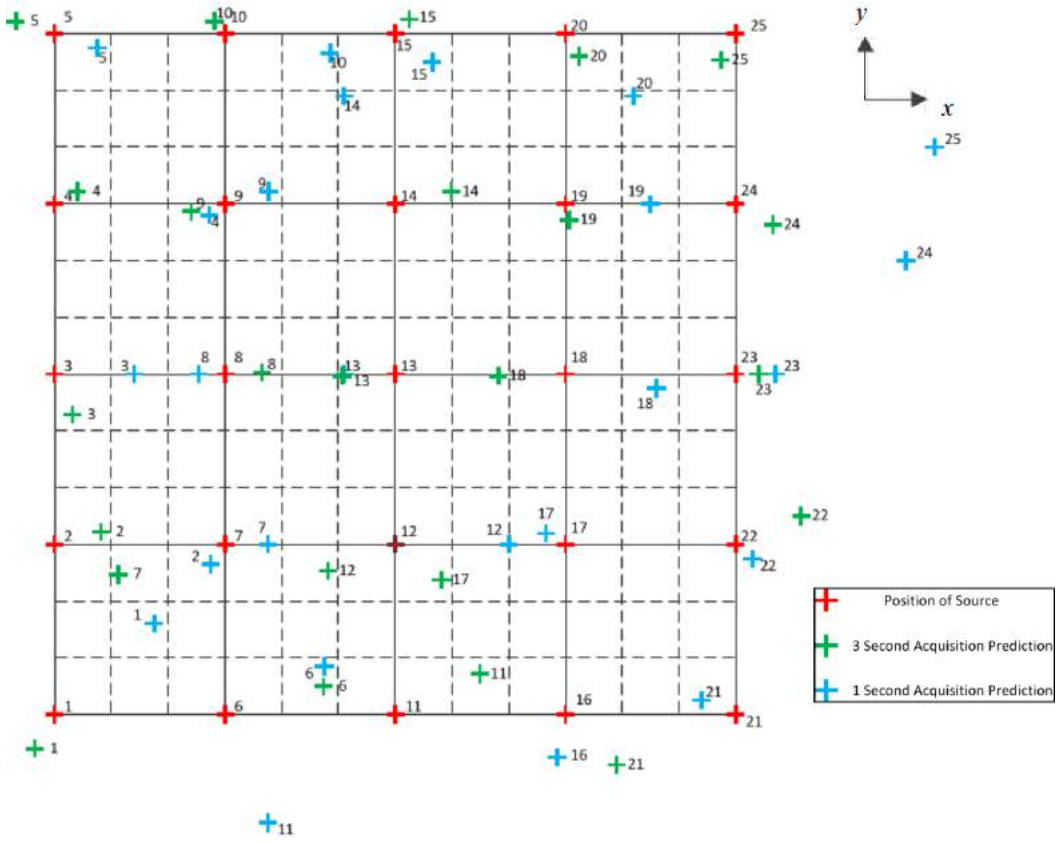

Figure 3.27: Predicted source positions from 2D mapping showing 1s and 3s acquisition results.

Each set of data was analysed, the minimum point of each SRC was resolved and the direction of each source position, from each detector, was found relative to the calibration. The direction from each detector was then used to resolve a position for each source for the 1s and 3s acquisitions and these were compared to the physically measured source positions. These results are plotted in Figure 3.27. It can be seen that

greater precision and accuracy is achieved in y-axis than in the x-axis. This is because the 5x100x100mm detector (RadICAL 1 in Figure 3.26) was positioned to resolve directions in the y-axis and the smaller 3x40x40mm CsI(Na) detector (RadICAL 2 in the figure) was used to resolve directions in the x-axis. Greater accuracy was achieved for the longer acquisition times with a mean difference between the measured and detected source positions of $75 \pm 46.6mm$ for 1 second acquisitions per step and $45 \pm 29.1mm$ for 3 second acquisitions per step. Greater accuracy, and precision could be achieved by using larger detectors, a higher activity source or longer acquisition times.

3.2.9 Energy Window Results

A further investigation was conducted into whether multiple sources could be located within a mixed energy gamma field. This involved exposing the 5x100x100mm CsI(Na) RadICAL detector to a ^{137}Cs and a ^{60}Co source simultaneously and assigning two separate energy windows to the results in order to pick out separate SRCs which could then be used to locate each of the sources. These experiments were conducted at the Home Office Centre for Applied Science and Technology (CAST) in Sandridge, Hertfordshire.

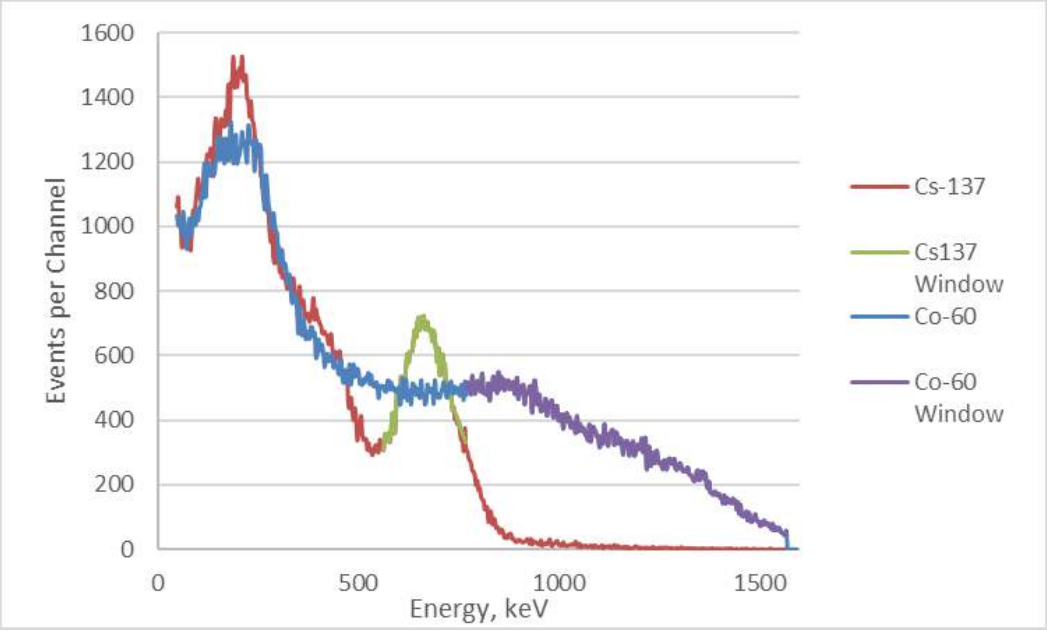

Figure 3.28: ^{137}Cs and^{60}Co energy spectra, taken with 5x100x100mm CsI(Na) RadICAL detector with energy windows shown.

An energy calibration of the detector was taken using a 9.0 MBq ^{137}Cs source and then a separate spectrum was taken using a 7.4 MBq ^{60}Co source. Energy windows

were set around the 662 keV ^{137}Cs photopeak and from 761 keV to 1600 keV to include the ^{60}Co only results. These spectra, and highlighted energy windows, are shown in Figure 3.28.

The two sources were then moved between 6 clearly defined positions at distances of between 1 and 3 meters from the detector, as shown in Figure 3.29. Each source position was measured to an angle within $\pm 2.5^{\circ}$ of the calibration position shown in Figure 3.29. Due to time constraints only four acquisitions were taken. For each acquisition the two sources were placed in separate positions and an acquisition was taken with 250 x 5 second, 1.44° steps.

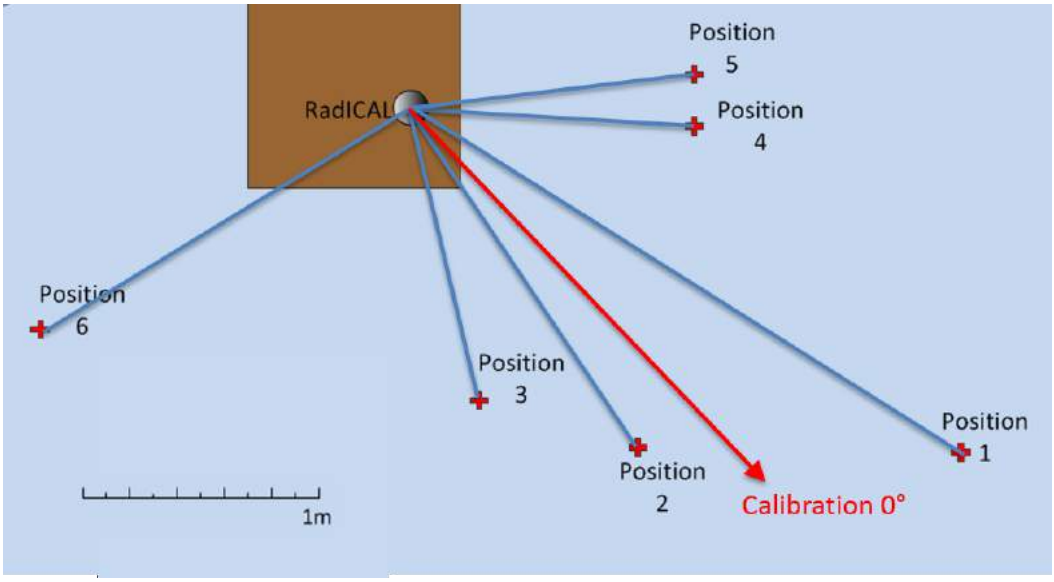

Figure 3.29: Source positions for ^{137}Cs and ^{60}Co data taken simultaneosly with multiple energy windows.

For each acquisition SRCs were plotted using only events from within each of the two energy windows, described above. Figure 3.30 shows response curves for the events occurring within each of the two energy windows taken from acquisition 2. It can be seen that events from the high energy, 761-1600 keV, window produce a clear SRC as all of these events are from ^{60}Co only. The 561-762 keV window, corresponding to the ^{137}Cs photopeak, produces a response curve with a clear indication of the ^{137}Cs position as well as an artefact that corresponds to the direction of the ^{60}Co source.

Table 3.4 shows the results. For each combination of source locations it was possible to correctly determine the direction of both the ^{137}Cs and the ^{60}Co source from a single acquisition. The mean difference between the measured and detected source

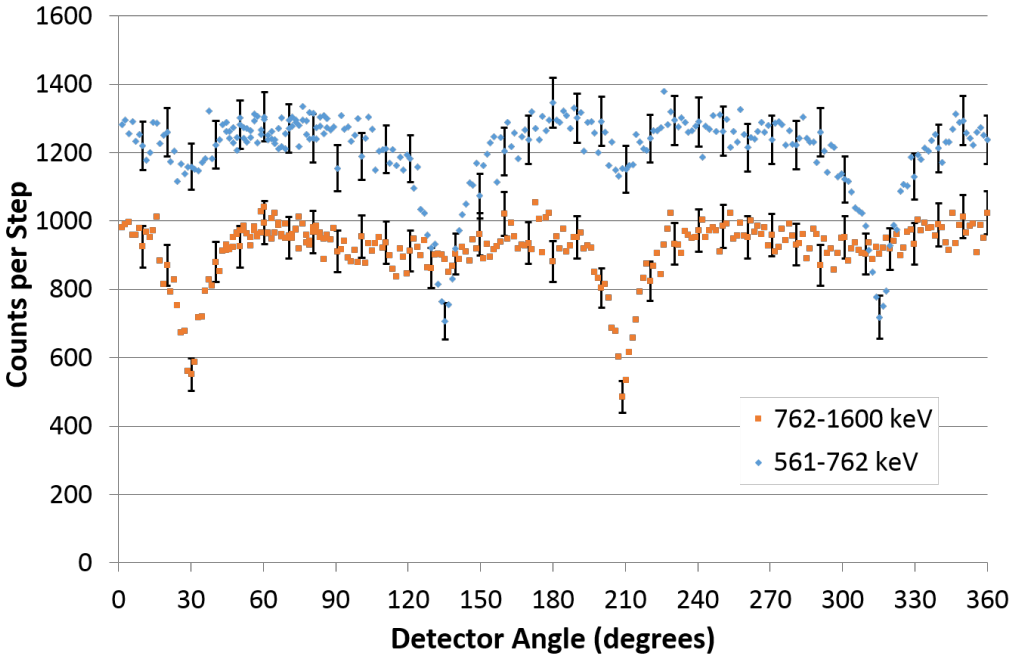

Figure 3.30: SRCs for ^{137}Cs and ^{60}Co source detection taken simultaneously and discriminated by energy.

Acquisition Number		1	2	3	4
Position	**^{137}Cs**	1	4	5	5
	^{60}Co	2	3	4	6
Measured Angle	**^{137}Cs**	$165 \pm 2.5°$	$135 \pm 2.5°$	$125 \pm 2.5°$	$125 \pm 2.5°$
	^{60}Co	$10 \pm 2.5°$	$30 \pm 2.5°$	$135 \pm 2.5°$	$105 \pm 2.5°$
Predicted Position	**^{137}Cs**	$164.16 \pm 0.72°$	$135.36 \pm 0.72°$	$125.28 \pm 0.72°$	$125.28 \pm 0.72°$
	^{60}Co	$8.64 \pm 0.72°$	$30.24 \pm 0.72°$	$135.36 \pm 0.72°$	$103.68 \pm 0.72°$
Difference	**^{137}Cs**	$0.84 \pm 2.60°$	$0.36 \pm 2.60°$	$0.28 \pm 2.60°$	$0.28 \pm 2.60°$
	^{60}Co	$1.36 \pm 2.60°$	$0.24 \pm 2.60°$	$0.36 \pm 2.60°$	$1.32 \pm 2.60°$

Table 3.4: Measured ^{60}Co and ^{137}Cs source positions compared to predicted energy windowed events.

directions of $0.63 \pm 2.60°$. The size of the ^{60}Co artefact in the 561-762 keV window results depends on the relative flux contributions of the two sources.

3.2.10 Current Mode Results

The detector setup described in Section 3.1.1.1 was tested with a variety of sources in current mode as an alternative to the previously acquired pulse mode data. A 156 kBq ^{137}Cs source was positioned 20cm from the axis of rotation of the large CsI detector setup for current mode acquisition. The detector was rotated at a constant rate of 250s per 360° revolution. A 10μF charging capacitor was used in parallel with a 330kΩ

resistor in the RC circuit to allow a time period of 3.3s. The fluctuating voltage was logged throughout the rotation and this signal is plotted against time in Figure 3.31. The detector was run at -1800V so the output is seen to decrease as scintillation light increased therefore the output appears to be inverted, compared to previously acquired pulse mode data.

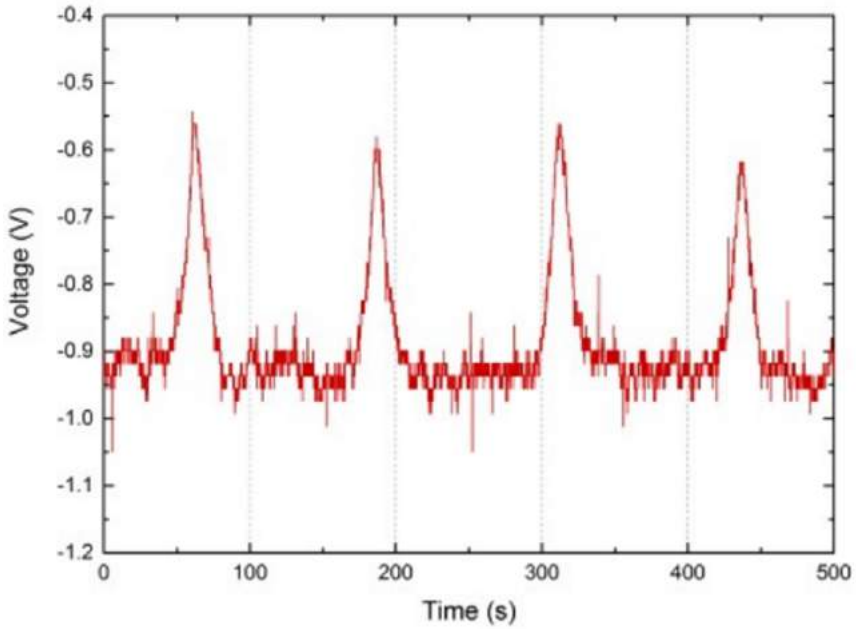

Figure 3.31: Current Mode Voltage Output (A. Alexandrou)

A separate set of data was then acquired using the same detector setup for pulse mode for comparison. The same source, position and high voltage supply were used. The detector was rotated 360° and an acquisition was taken at each 1.8° step. As with previous pulse mode data a lower level discriminator was set at 50 keV to filter out pulses caused by low energy noise.

By inverting the current mode results and normalising both these and the equivalent data from the pulse mode system the two signals can be compared. This can be seen in Figure 3.32.

It can be seen that the two outputs correlate closely, to within 6% of the maximum counts for each individual step. Within the error bars shown the two curves demonstrate the same behaviour. This suggests that current mode presents a viable alternative processing method for the RadICAL system. Advantages of this method include the lack of expensive and bulky auxiliary equipment required, the potential to run the detector more quickly and the elimination of problems associated with dead time in high

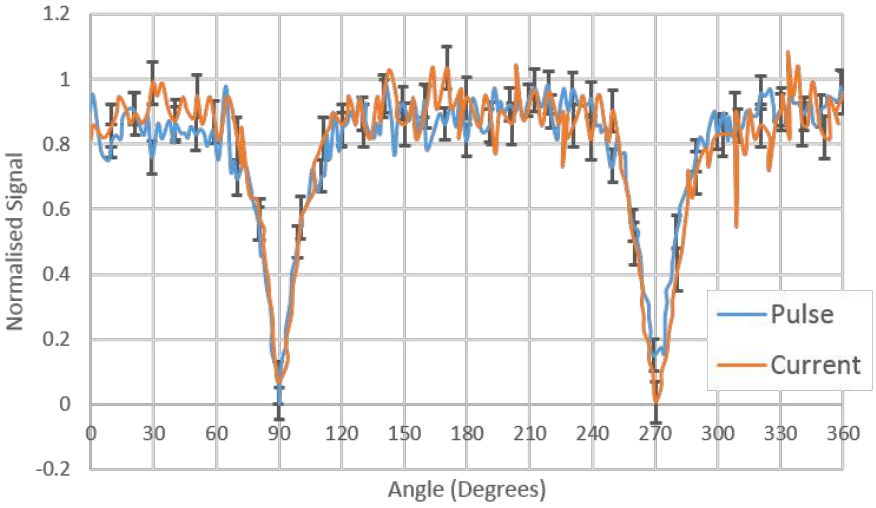

Figure 3.32: A Comparison of Current Mode and Pulse Mode Data.

flux environments. Disadvantages are due to an inability to gain information from specific pulses, most notably energy, which can be used to identify sources and filter out background radiation, and PSD.

3.2.11 High Flux Current Mode Results

The same setup was used for a further investigation into high flux environments. This involved exposing the detector to a high intensity photon flux from an X-ray source.

The detector was setup in current mode, as described previously. The rotation speed was set to its minimum period of $25.0 \pm 0.2s$. The capacitor in the RC circuit was set at $2.2\mu F$ which resulted in a response time of $0.726s$.

This setup was positioned 140cm from the X-ray source, which was set to 63kV and 0.1mA. Due to the high flux the signal to the oscilloscope exceeded its maximum input of 20V. To reduce this signal a 39.9 ± 0.1mm aluminium filter was placed in front of the source.

Figure 3.33 shows the way that the voltage fluctuated with the angle of the rotating detector. A smooth response can be observed due to the high number of incident events. A slight difference in response can be seen at the minimum voltage at 90° separation on the plot. This may be due to imperfections in the crystal material due to degradation over time.

The detector was then converted to obtain equivalent pulse mode data, as described in previous experiments, for direct comparison. The X-ray source was again set to

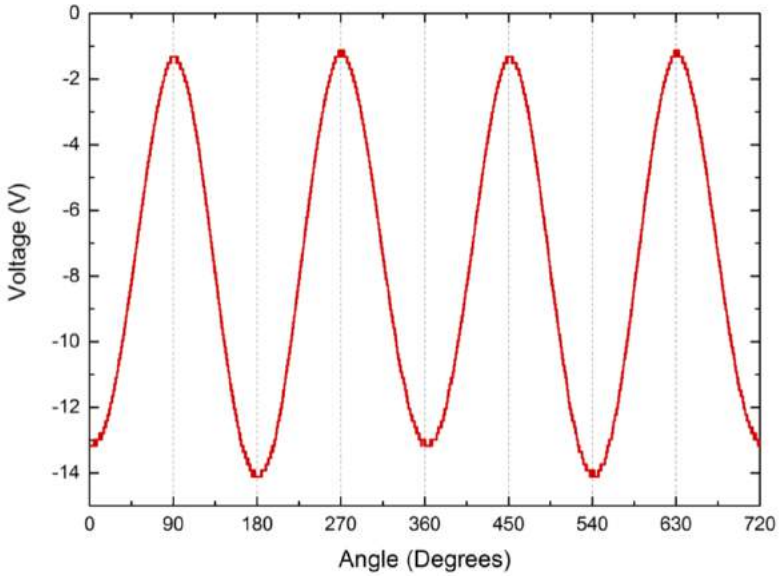

Figure 3.33: Current mode response to X-ray source. 63kV, 0.1mA, 1.40m away. (A. Alexandrou)

63kv and 0.1mA and the detector was positioned 140cm from the source window and the 39.9 ± 0.1mm aluminium filter was again positioned between the source and the detector

In order to achieve equivalent conditions the acquisition time (real time) per 1.8° step of the detector was set to 0.02s so that a minimum total acquisition time of 34 ± 1s could be obtained. A high dead time of around 80% was recorded.

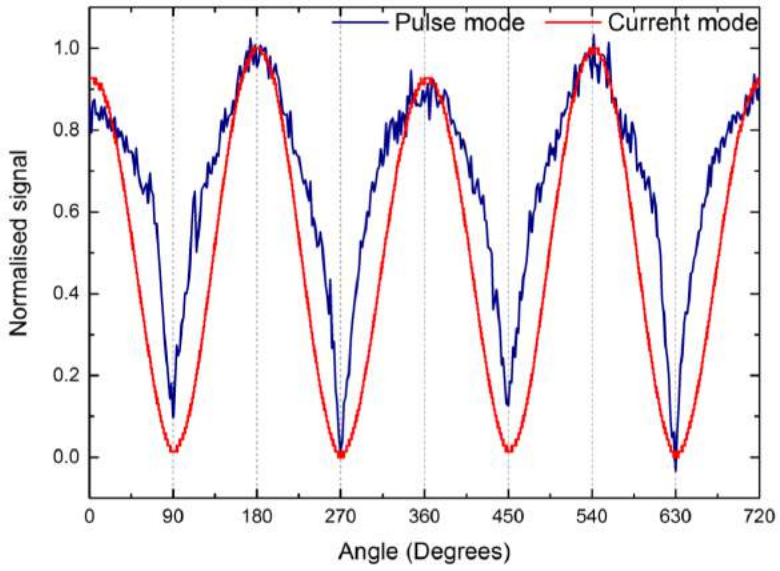

Figure 3.34: Normalised current mode and pulse mode response to X-ray source. 63kV, 0.1mA, 1.40m away. (A. Alexandrou)

Figure 3.34 shows a comparison of the pulse mode and current mode SRC data. Both responses have been normalised and the current mode data has been inverted to allow direct comparison. The pulse mode data can be seen to be much noisier than the current mode data due to the inefficiency associated with pulse counting in such high flux environments. The relatively smooth shape of the current mode response could be a result of a high proportion of low energy events that are cut by the lower level discriminator used in pulse counting mode.

3.3 Summary of RadICAL Detector Evaluation

Three different RadICAL detectors have been constructed and tested under a variety of different experimental conditions. The concept has been proven as an effective means of discerning the direction of a photon source and multiple detectors can be used to find the specific location of a source. The accuracy and precision depends on the flux at the detector, the geometry and material of the detector or the time available for acquisition.

A single, 500 MBq, ^{137}Cs source has been located to within $1.58 \pm 1.12^{\circ}$ over distances up to 11m. Two detectors have been used simultaneously to locate a 3.28 MBq ^{137}Cs source to within $45 \pm 29.1mm$ over a 2 dimensional, 60cm x 60cm grid.

It has been shown that separate SRCs can be obtained from a single acquisition by sorting events according to energy. A 9.0 MBq ^{137}Cs source and a 7.4 MBq ^{60}Co source have been located in separate positions simultaneously to within $0.63 \pm 2.60^{\circ}$ over distances from 1m to 3m. This suggests that gamma and neutron events may be sorted into separate SRCs to find the location of a neutron only source within a mixed field. This is likely to have positive implications for the final detector system, which is described in the next chapter.

Current mode operation has been investigated and shown to be a viable alternative to pulse mode, particularly in high flux environments. Due to the neutron discrimination methods required for the final detector system all further work on this project is to be conducted in pulse mode.

Chapter 4

Final Detector Design

This chapter describes the decision making process behind the final design and build of the mixed field detection system. This system is based around the RadICAL Stack concept described in Chapter 1.6.2.

Modelling and experimental investigations, into the curve fitting technique used to determine source direction from a set of stationary points, are included. Based on these investigations a detection system was designed and built. A detailed description of this system, and its construction, is also included.

4.1 Source Localisation Method and Validation

In order to determine directional information from a stack of stationary detectors it was necessary to determine a method of fitting count rates from each element to a standard response curve (see section 1.6.2).

4.1.1 Curve Fitting Procedure

The localisation method works by examining count rates from a stack of stationary detectors, each positioned around a central axis and offset by a fixed angle to one another. A Calibration Standard Response Curve (cSRC) is generated by rotating the stack of detectors relative to a source and recording counts from each element at regular intervals. When the stationary detector is then exposed to a source it can be used to determine the source's direction by plotting count rates on top of the cSRC and conducting a least-squares fit.

The 100x100x5mm CsI(Na) detector described in Chapter 3 was then used to validate the method using a single detector.

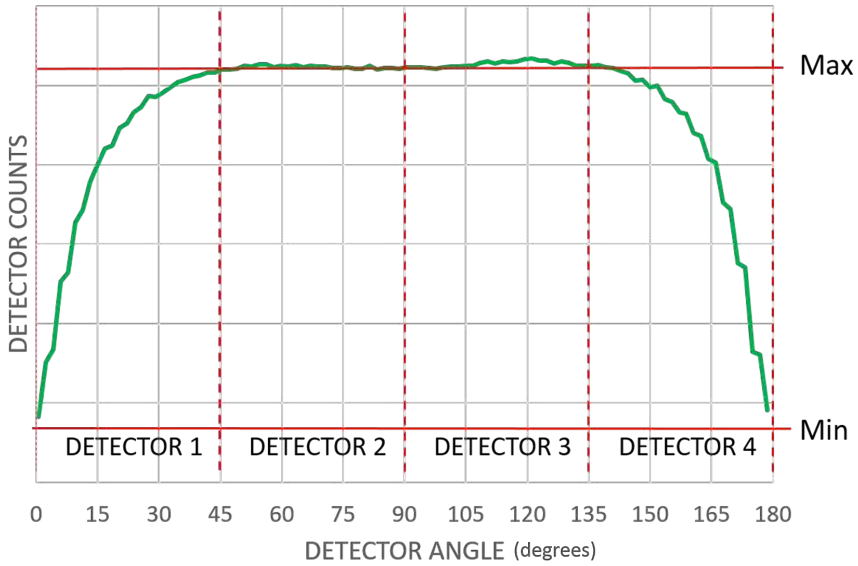

Figure 4.1: cSRC Marked with Max and Min Count Rates and Split into 45 Degree Regions.

First the detector was calibrated by generating a cSRC that was specific to the scintillator geometry, material and the energy range of the source. These are identical to the SRCs described in Chapter 3 and are generated using long acquisitions in order to keep noise to a minimum. The maximum and minimum count rates were logged and the cSRC was then normalised between 0 and 1.

The stationary stack could then be used to locate a source using a specially designed MATLAB code. An example of this code, written for 4 detector elements separated by an angular offset of 45°, is included in Appendix A of this thesis. A summary of this example is detailed below:

- Each of the four detectors was used to acquire a separate count rate based on a fixed time window and these count rates were compared.

- Figure 4.1 shows a 180° cSRC split into four separate 45° regions that coincide with each detector. It can be observed that approximately 90°, or 50%, of this cSRC coincides with the flat region of the curve that shows maximum count rate. Based on this observation it can be assumed that the maximum of the four detected count rates will coincide with the maximum of cSRC.

- Based on this assumption the four count rates were scaled to fit the count rate of the cSRC. This was done by using the detector with the maximum detected

counts to estimate the maximum point on the curve and the max/min ratio of the cSRC to estimate the minimum point.

- These scaled detector points were then plotted on top of the cSRC, separated at angles that correspond to the angular separation of detectors - 45° in the case of this example .

- A least squares fitting method was used to evaluate how close these points correlated with the cSRC. This involved finding the minimum distance between each of these points and cSRC, as shown in Figure 4.2, squaring each of these distances and then summing each of these four values together. This value was logged.

- The four detected points were then moved 1° along the x-axis, relative to the cSRC and an equivalent value was calculated and logged.

- This process was repeated over the full cSRC. The smallest least squares value represented the closest fit and was therefore used to determine the direction of the source.

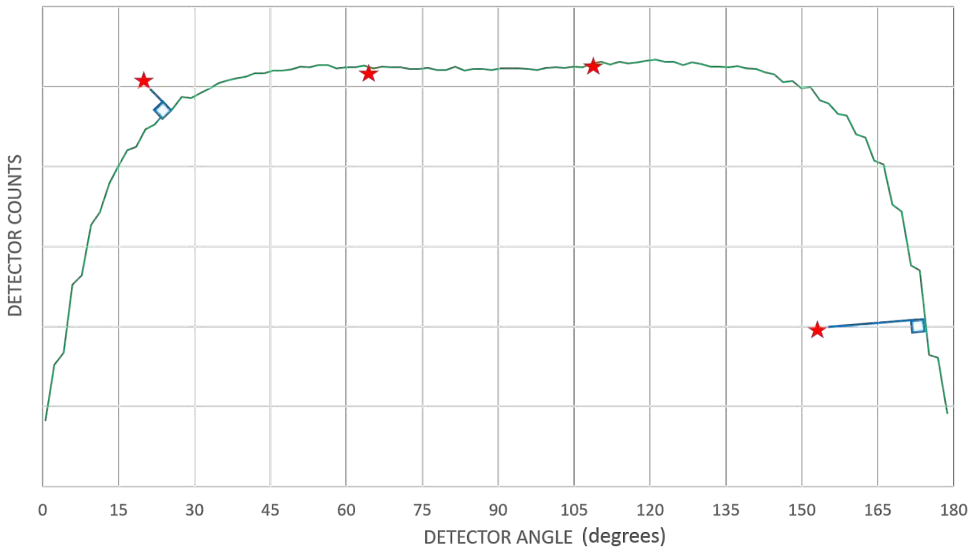

Figure 4.2: cSRC with individual count rates from 4 element stack plotted

4.1.2 Determining Direction of Source using limited points from a single rotating detector

In order to validate this method prior to construction of the final detector, and to investigate an optimum number of detector elements, and angular separation, the concept was tested using a single slab of 12.7x140x150mm Eljen EJ200 plastic scintillator, within the detector described in the previous chapter, using the following method:

- Data previously acquired and described in Chapter 3, and shown in Figure 3.20a, was used as the cSRC in this example. This involved a 3.28 MBq Cs137 source, positioned 50 ± 0.5cm from the axis of rotation whilst the detector was rotated 360° in discrete 1.8° steps, taking a 240 second acquisition at each step.

- The source was placed in a series of 16 different positions. These were at distances of $50 \pm 0.5cm$, $60 \pm 0.5cm$ and $70 \pm 0.5cm$ from the central axis of the detector. Each source was separated by $15 \pm 0.5^\circ$, relative to the detector.

- For each source location acquisitions were taken with the detector at 2, 3, 4, 5, 6 and 10 equally spaced angles ($90 \pm 0.18^\circ$, $60 \pm 0.18^\circ$, $45 \pm 0.18^\circ$, $36 \pm 0.18^\circ$, $30 \pm 0.18^\circ$ and $18 \pm 0.18^\circ$ respectively) around the central axis to mimic the behaviour of different numbers of stationary stack elements. Errors were based on the 5% non accumulative error of the stepper motor rotating the detector.

- For each source position and detector angle a 10s (live time, error quoted to nanoseconds so considered negligible) acquisition was taken.

- These count rates were compared to the cSRC using the least squared method described above and the direction of the source was determined.

- The direction of the source, determined by the detector and curve fitting method, was then compared with the physically measured direction. This comparison is shown in Table 4.1. The mean difference between each predicted and measured source position provides a measure of accuracy. The standard deviation of each position provides a measure of precision.

These results show that the direction of a single source can be determined to within the required 5°, over a 180° degree field of view, with five or more detector elements,

Number of Detectors	2	3	4	5	6	10
Angular Separation (degrees)	90	60	45	36	30	18
Mean Difference of Angle Predicted to Measured Direction (degrees)	57.9 ±33.3	28.0 ±13.4	10.6 ±5.6	5.2 ±3.7	3.8 ±3.3	3.4 ±2.7

Table 4.1: Angular resolution comparison for different number of stack elements in 360° field of view.

separated at an angle of 36° or less. An improvement in angular resolution is observed with an increasing number of detector elements. Over a more limited field of view fewer detectors elements may be necessary as the significant change in the cSRC occurs over a 90° section of the curve.

4.1.3 Curve Fitting Analysis

Further analysis was conducted to investigate the total number of events needed to achieve the systems localisation requirement using a variety of different angular separations between each detector.

Because the final system is to utilise Eljen EJ299 plastic scintillator and because data on the neutron spectrum was not available, this analysis was based around a model of photons interacting with plastic scintillator. This simple model, described in Chapter 2.1, involved a 140x150x12.7mm slab of polyvinyl toluene rotating relative to a parallel, uniform flux of 662 keV photons to form an SRC, this response was shown previously in Figure 3.23.

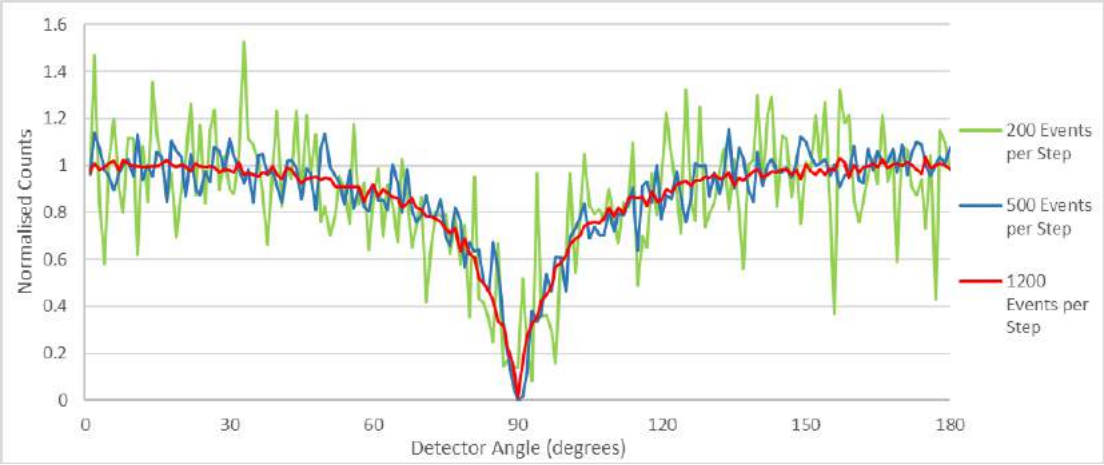

Figure 4.3: Modelled SRC with simulated Poisson noise for 200, 500 and 1200 events per step.

Different count rates were investigated between 200 and 1200 counts per step. By assuming Poisson statistics the appropriate, randomly generated, noise can be applied

to the response curve for each number of counts. Figure 4.3 shows the modelled response curve with simulated, Poisson noise based on 200, 750 and 1200 events per 1° step. By picking appropriate points along the curve to represent four elements in the stack at equal spacings of 20°, 30° and 45° different detector configurations could be investigated over 60°, 90° and 180° fields of view respectively.

By using the least squares curve fitting procedure, described previously in Section 4.2.1, each set of points, with added noise, could be compared to the original SRC to determine the direction of the source. The predicted and true position could then be directly compared. By repeating this process over a number of different angles the mean difference could then be recorded and used to compare the effectiveness of different detector setups.

Figure 4.4 shows a comparison of the modelled fit for three separate four detector setups positioned with 20°, 30° and 45° angular offsets and count rates between 200 and 1200 counts per step. It can be seen that the angular resolution of 5°, required by the detector system, occurs at count rates $\geq$ 750 events per step. These results are similar for each detector configuration but the greatest angular resolution is observed, for all count rates, when the angular separation between each element is 30° and the total field of view is 90°.

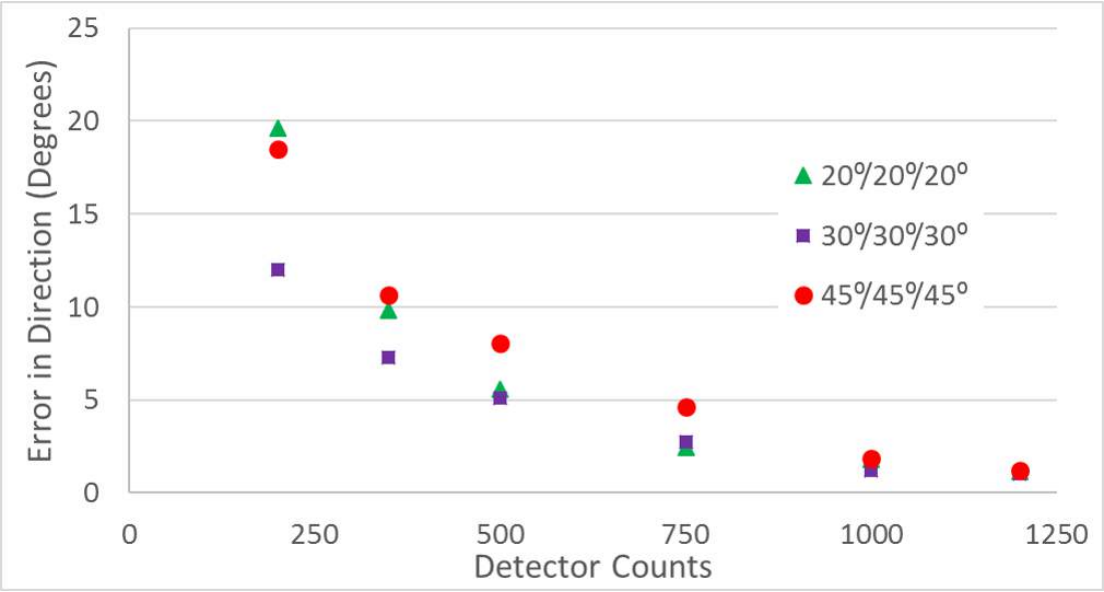

Figure 4.4: Modelled results for 4 element system with 20°, 30° and 45° angular detector offset.

4.1.4 Limitations of method

A number of major differences are to be considered between the method demonstrated above and that to be used for the final detector system. These are described below:

- A difference in detection efficiency is likely between each of the detector elements due to imperfections in the manufacturing procedure. Every effort should be made to build each element to a uniform standard and a calibration method is to be included in the updated code.

- Due to the same factors some difference may be observed between each detector element when discriminating neutrons from gammas. This should also be investigated and accounted for in the calibration method.

- Problems may be encountered due to the manner in which the detector elements are to be stacked vertically. The vertical offset between each element should be kept to a minimum, as shown in Figure 4.5 as this may cause some differences in count rates when the source is close to the detectors. This may be due to additional faces of each detector being partially exposed to the source. The vertical dimension and offset of each detector element should be minimised so that the minimum working distance from the source to the detector is not increased unnecessarily.

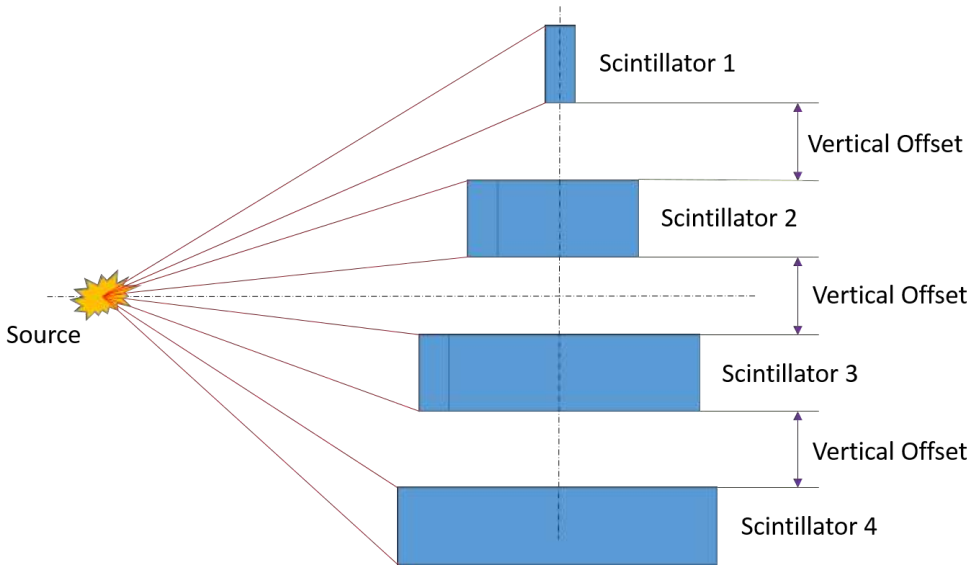

Figure 4.5: Effect of Vertical Offset on Detector Response when Source is Close

4.1.5 Detector Requirements

Based on flux conditions suggested by AWE a set of requirements for the detector system were determined. These requirements are based on a number of different potential detector positions around the interrogation volume and were used in the final design of the detector. Assuming a 'threat' object diameter of approximately 30cm and a detector standoff of 2.5m, from the edge of the interrogation volume, it was determined that an angular resolution of no better than 5° was required. Using the figure of 150 counts per cm^2 per interrogation 5m from the source, as provided by AWE, a flux of approximately 600 counts per cm^2 can be assumed, according to the inverse square rule, at the same detector standoff of 2.5m.

4.2 Construction of the prototype RadICAL Stack Detector System

Based on the suggested flux conditions, the modelling described in Chapter 2 of this thesis, and on the results of the experiment described in section 4.2 a prototype RadICAL Stack detector was built. The results of the experiment described in Section 4.2.2 suggested that the required angular resolution of 5° could be achieved by 5 or 6 detectors over a field of view of 180°. Given that the system was to be designed for a reduced field of view of 90° it was decided that further analysis should involve 4 detector elements.

4.2.1 Initial Detector Geometry Design

Based on suggestions provided by AWE a predicted flux of around 600 neutrons per cm^2 per interrogation was estimated. Using a conservative estimate for event registration of around 10 percent it can be assumed that imaging should be based on around 60 events per cm^2 on the detector. This value was used in determining the required geometry of each element for the final detector system. Based on the predicted neutron flux detection of 60 per cm^2 and minimum number of 750 events required for imaging each detector should have an exposed surface area of at least 12.5cm^2, with improved performance expected at greater size.

Based on these figures a detector element geometry of 12.5mm x 35mm x 150mm was chosen. This was based on the standard 12.5mm thickness of available EJ299 plas-

tic scintillator and some concerns about loss of PSD ability within irregularly shaped scintillators, as previously discussed in Chapter 2.2.4. The ratio of the longest and shortest dimensions provided an aspect ratio of 12:1, similar to those used in the existing RadICAL detectors and modelling. The 35mm dimension was chosen to keep the total height of the detector to a minimum, a shown in Figure 4.5, whilst providing enough height for direct coupling of an appropriate photomultiplier.

4.2.2 Detector Element Construction

Four 1.5 inch photomultipliers (ET Enterprises 9102B) were chosen as appropriate photodetectors for the specific detector material and geometry. This was based on the wavelengths at which they are sensitive covering the emission spectrum of the EJ299-33 as shown in Figure 4.6. Other advantages include their good linearity and fast timing characteristics.

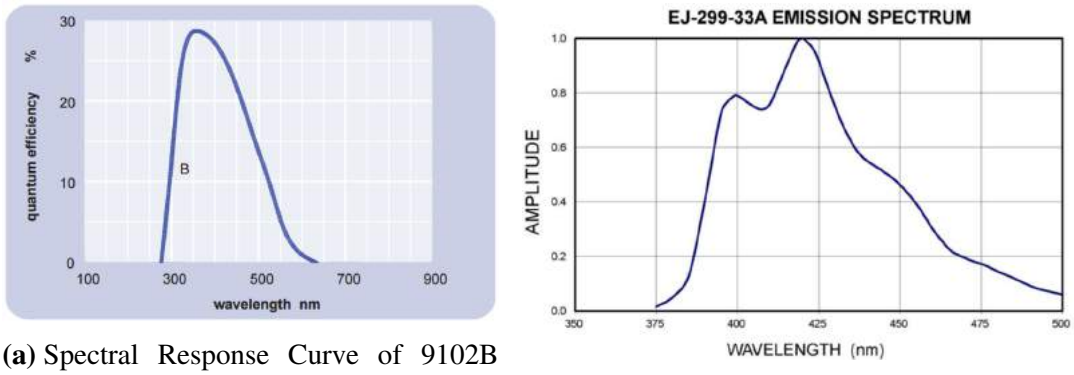

(a) Spectral Response Curve of 9102B PMT (ET Enterprises)

(b) Quantum Efficiency of EJ299-33 (Eljen)

Figure 4.6: Comparison of PMT and Scintillator Wavelengths.

Each photomultiplier is to be coupled directly to one 12.5mm x 35mm end face of each scintillator slab as this position was previously shown, in the modelling described in Chapter 2.2.3, to be optimal for light collection. This position was also chosen to keep the photomultiplier, associated circuits and cables away from the detector's field of view so that the attenuation of incident flux in these items does not distort the shape of the response curve. A further advantage of these choices is that the photomultiplers 39mm diameter face covers the 12.5mm x 35mm end surfaces of the scintillators to which they are to be coupled.

Each EJ299 block was finely polished and coated with several layers of white BaSO4 paint on 5 faces, leaving one of the small 12.5mm x 35mm faces clear. This

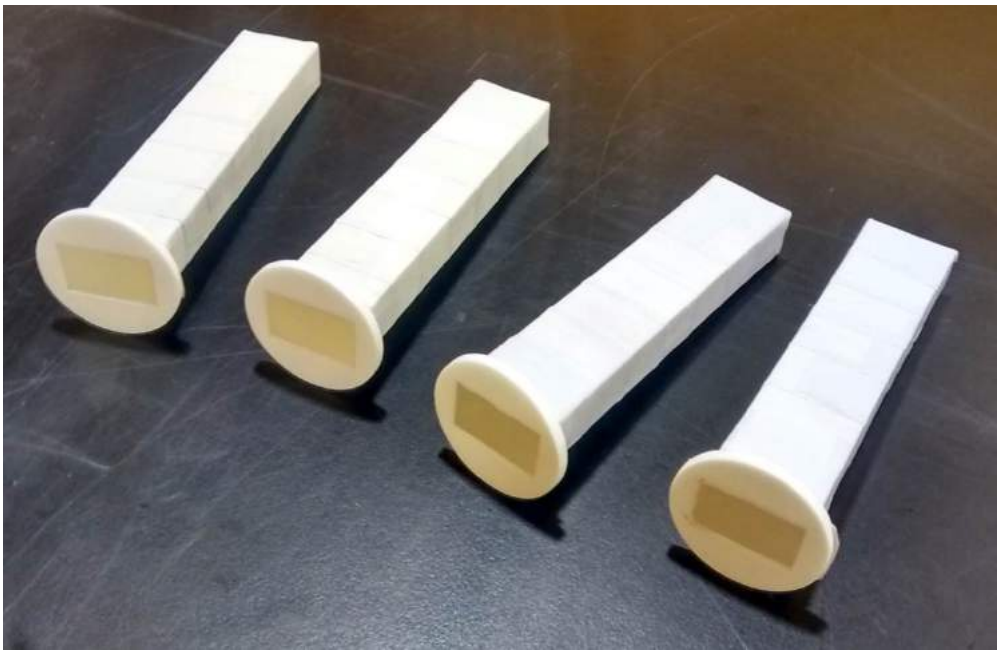

Figure 4.7: The painted, and wrapped, EJ299 detectors before coupling to the PMT.

was to provide diffuse optical reflectance to the internal surfaces of the detector. Four x 39mm diameter acrylic discs were then cut, using a laser cutter, to match the window of the photomultiplier. A 12.5 x 35mm aperture was then cut out of the centre of each. The unpainted face of each detector was then inserted into the aperture of each disc and then held in position using a strong adhesive to form the completed units shown in Figure 4.7. The circular face of each unit, consisting of the unpainted detector face and the acrylic disc was then polished to ensure a single uniform surface.

This surface, on each detector, was then coupled directly to the window of each photomultiplier. A coupling gel (Cargille 081160) was used to couple the detector to the PMT due to its refractive index, n = 1.52, being between that of the borosilicate glass used in the PMT window (n = 1.49) and that of the EJ299-33 (n = 1.58). Once the coupling gel had dried the entire unit was wrapped with PTFE tape and white vinyl insulation tape in order to secure the coupling and minimise any ambient light leaking into the detector. The pin connectors at the base of each PMT were left clear of tape and were then connected to negative high voltage resistor bases (ET Enterprises C646AFN2) which were used to supply high voltage to each dynode and output a signal.

Each coupled PMT and scintillator was secured to a wooden base plate using polyethylene pipe clips and positioned within a 230mm x 300mm x 80mm ABS en-

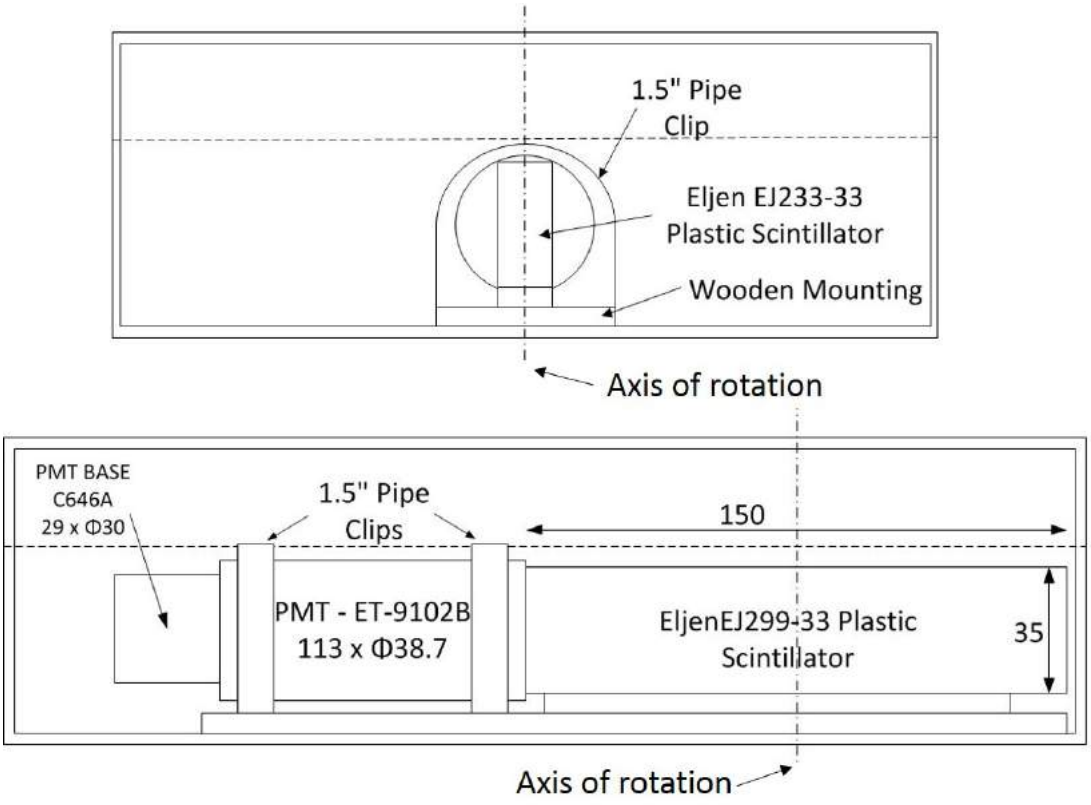

Figure 4.8: Side projections of detector element showing PMT, scintillator and mounting.

closure. Each wooden base plate was then secured to the inside of its corresponding enclosure with adhesive tape as shown in Figure 4.8. A 12mm hole was drilled in the top and bottom of each enclosure at the axis of rotation that corresponded to the centre of each detector element.

Two 10mm holes were drilled in the end of each enclosure and were fitted with an SHV and a BNC socket for the high voltage and signal respectively. These sockets were then connected to the signal, HV and earth terminals of the PMT socket by soldering short lengths of wire between the appropriate points. Figure 4.9 shows a completed stack element with the enclosure lid removed to show the detector components. For testing the enclosure lid for each unit was screwed to its respective body and black PVC tape was wrapped around the joint to minimise any remaining light leakage.

4.2.2.1 Detector Stack Construction

Although the detector was designed for use while stationary it was necessary to calibrate it prior to use. This involved rotating the complete detector stack relative to a radiation source in order to build up a separate set of cSRCs for each detector. This

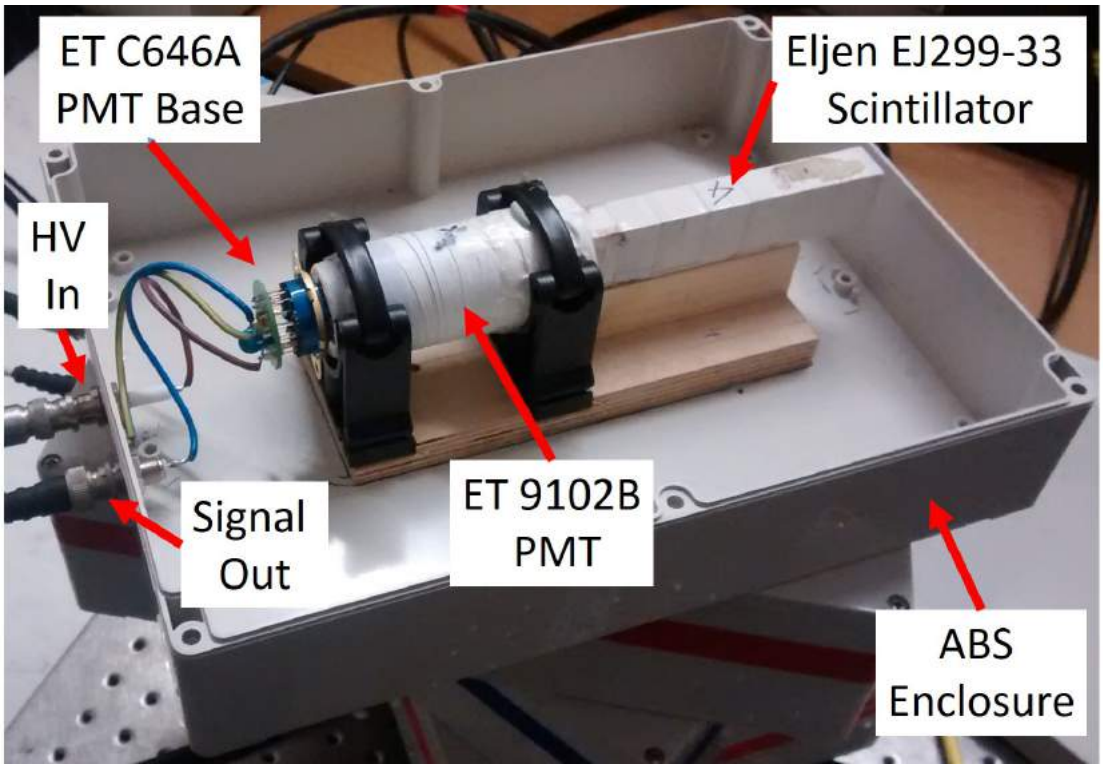

Figure 4.9: Completed stack element with container lid removed to show PMT and scintillator.

data can be used to compare the relative detection efficiency of each detector. Detected events from each stationary detector can then subsequently be compared to each cSRC, using the method described in Section 4.2.2, to determine the direction of the source. In order to easily generate these cSRCs the detector stack was built on top of a rotation stage so that the full unit could be rotated around a central axis.

The first element of the stack was mounted onto a rotating stage, Newport URS100BPP, to allow rotation around the central axis of the scintillator. This rotation stage was then connected to Newport ESP301 motion controller/driver to allow accurately controlled rotation of the detector via LabVIEW software. A second detector element was then bolted to the top of the first using the 12mm holes previously drilled in the top and bottom of each unit. The two remaining detector elements were then attached in the same manner, around the central axis, to build up a stack on top of the rotation stage. The four detector elements were then rotated precisely so that they were each separated by an angular offset of 30°, as shown in Figure 4.10, and secured in position using a strong adhesive. This offset was chosen based on the modelling described in Chapter 4.3.1. and allows localisation over a 90° field of view.

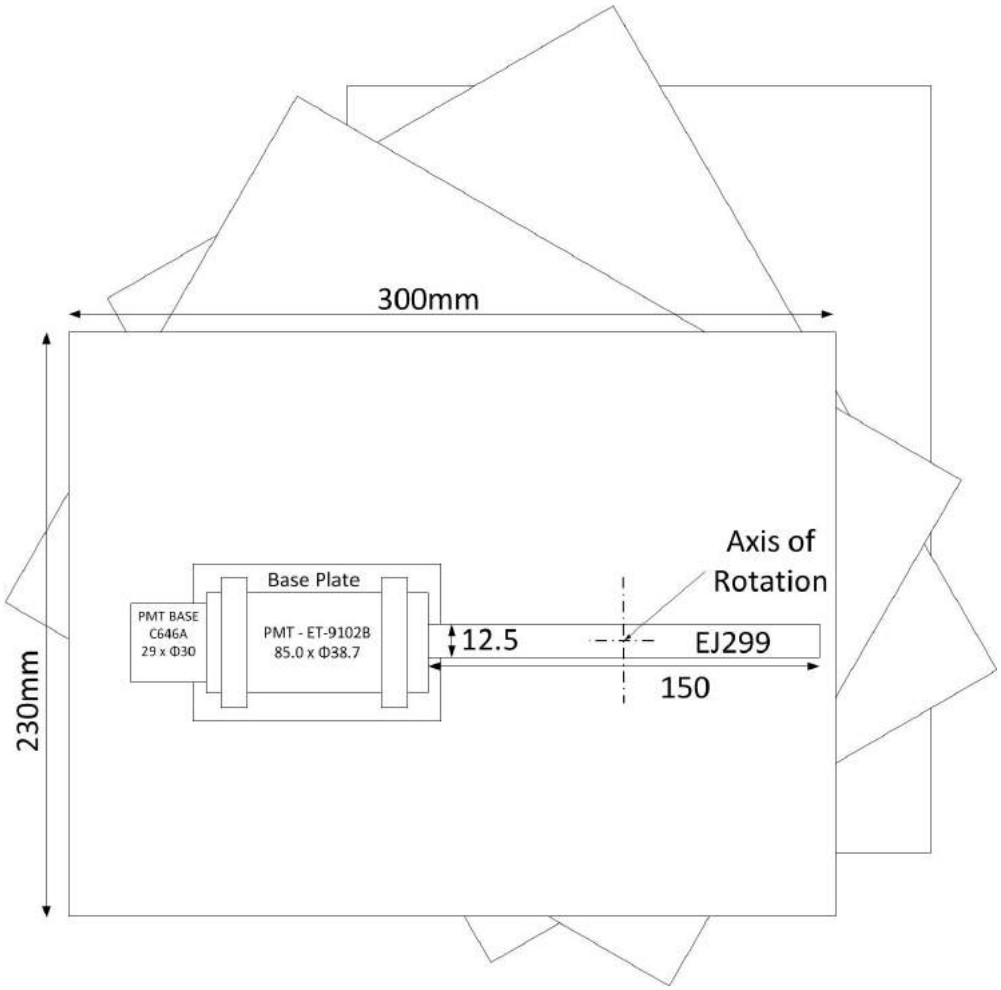

Figure 4.10: Detail plan of stack components

4.3 Data acquisition and Electronics

Each detector element was powered using a negative high voltage power supply and the signal was output to a digitiser (CAEN V1751) [98] which processed the pulses. A separate computer was used to analyse data from the digitiser and synchronise this with the controlled rotation of the system when acquiring cSRCs.

4.3.1 Choice of digitiser

A CAEN V1751 digitiser was used to process the pulses detected by the photomultipliers. This is a 1-unit wide VME module housing an 8 Channel 10 bit 1 GS/s Waveform Digitizer with 1 V peak to peak input dynamic range.

The MCX digitiser inputs were connected to the BNC detector outputs using a coaxial cable and appropriate connectors.

DPP-PSD (Digital Pulse Processing - Pulse Shape Discrimination) firmware [99]

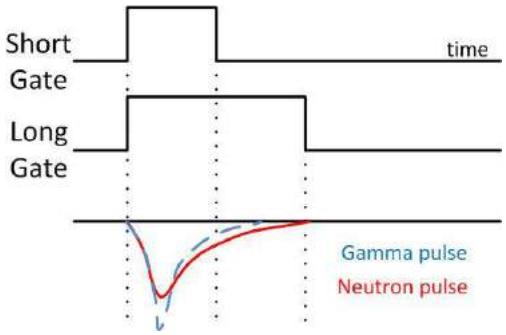

(a) Long and Short Gates Plotted with Respect to Input Pulses)

$$\text{PSD} = \frac{Q_{LONG} - Q_{SHORT}}{Q_{LONG}}$$

(b) PSD Equation

Figure 4.11: PSD Number Retrieval Method

was installed on the digitiser. This allowed a PSD number to be retrieved by applying a long and short gate to each pulse and comparing the integrated charge within each as shown in Figure 4.11.

WaveDump [99] is an additional mode of operation provided. This mode involves saving the full waveform for each event in an ASCII or binary format. This requires a large amount of memory and is therefore not appropriate for the large amounts of data required by this project.

The DPP-PSD firmware is a much more memory efficient manner of retrieving the relevant information. For each event a timestamp was recorded along with energy of the event and the previously mentioned PSD number. A block diagram of the DPP-PSD firmware is shown in Figure 4.12.

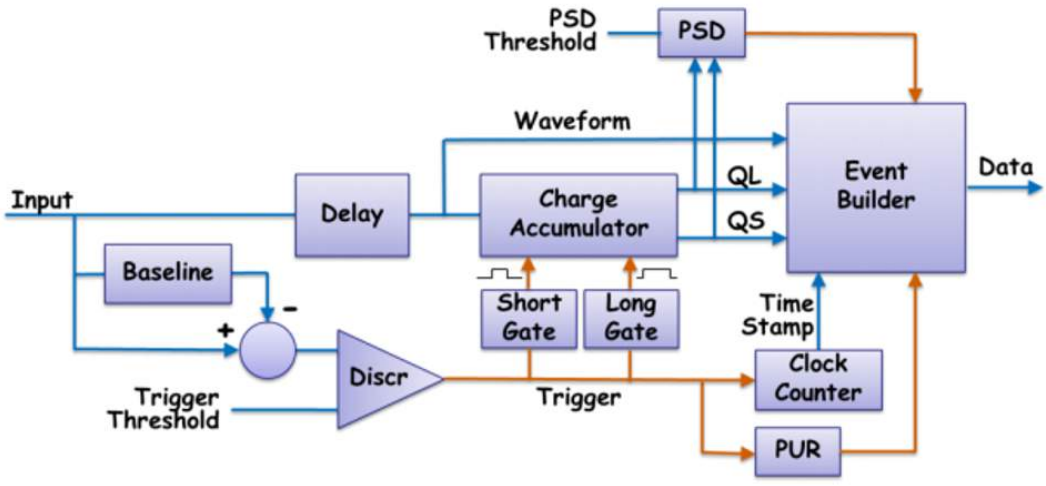

Figure 4.12: Flow diagram of DPP-PSD software (Caen)

Figure 4.13: CAEN digitiser installed in VME crate with USB bridge and Power Supply

4.3.2 Additional Electronics

A 6 channel, -4kV VME mounted power supply (CAEN V6533N) [98]was used to power each of the four photomultipliers and was able to supply up to 3mA of current up to a maximum power of 9W. Each channel can be digitally controlled from the same PC that was rotating the detector and acquiring data from the digitiser. A VME-USB bridge (CAEN V1718) [100] was used to provide a link between the power supply, digitiser and the PC via a single USB connection.

All three units were housed in a 4 slot VME crate (CAEN 8004B) [101]. This setup is shown in Figure 4.13. A separate USB connects the Newport ESP301 [102] motion controller which was used to rotate the detector system for calibration purposes.

4.4 Summary of Final Detector Design

The active interrogation scenario, proposed by AWE, was described including flux conditions, interrogation geometry and detector locations. This data was combined with the modelling and experiments, previously described in Chapter 2 and 3, to determine an optimum detector geometry for the proposed system. Using this geometry a detector was built and has been described in detail. The finished system involves a four element stack. Each stack element consists of a 12.7mm x 35mm x 150mm block of Eljen EJ299-33 plastic scintillator coupled to an ET Enterprises 9103B photomultiplier built inside an ABS enclosure. The four elements were vertically stacked and positioned at a 30° angular offset around a central axis. The four detectors were powered by a 6 channel CAEN V6533N -4kV power supply and each signal was fed to an 8 channel CAEN V1751 digitiser which allows neutron identification through pulse shape discrimination

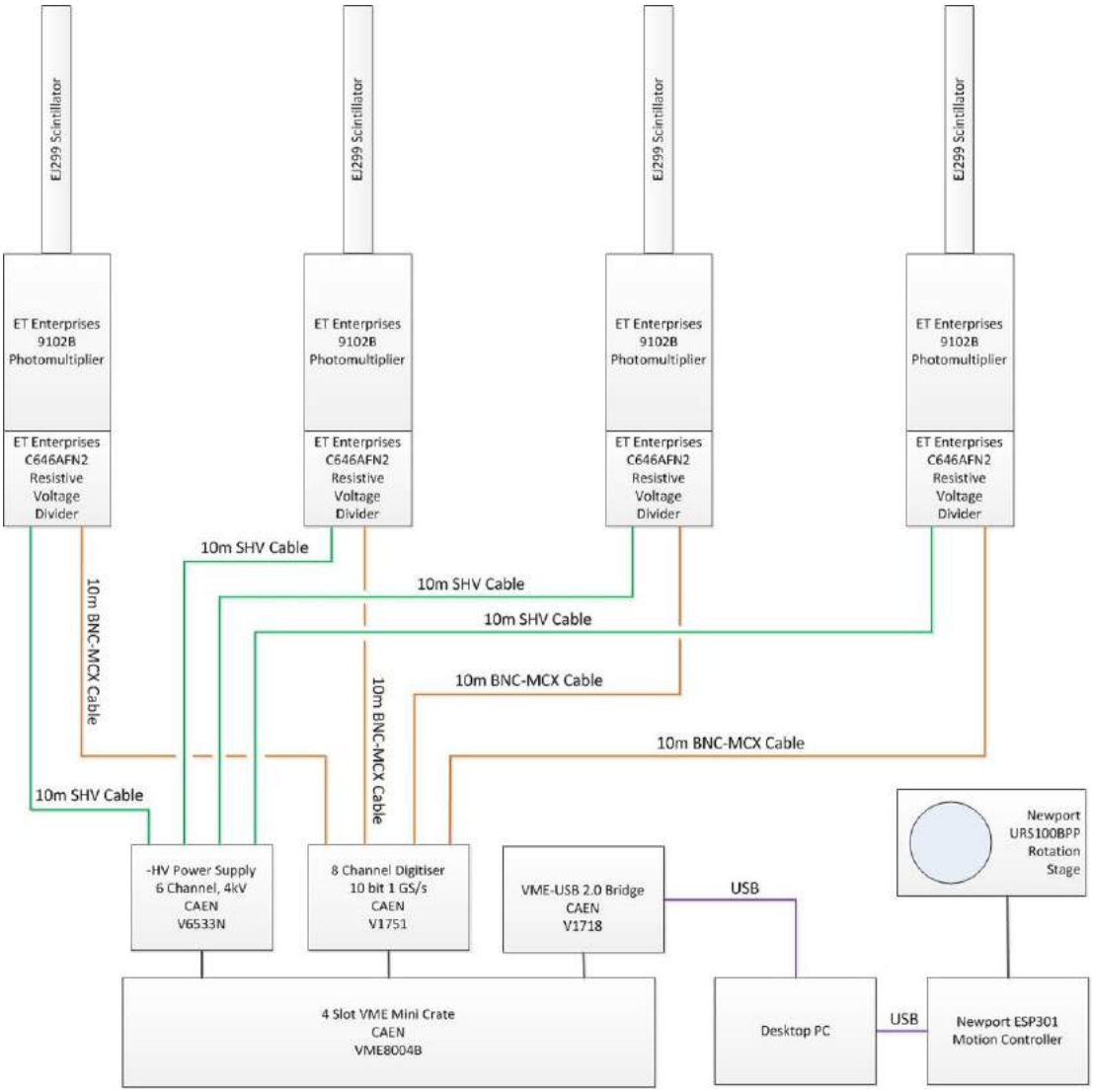

Figure 4.14: Flow chart of complete system setup.

techniques. A flow chart of the complete setup is shown in Figure 4.14. The entire detector stack was mounted onto a Newport URS100BPP rotation stage which allowed the detector to be rotated in order to produce the cSRCs required for source localisation. The complete system was subsequently evaluated using a variety of gamma and neutron sources. This is described in detail in Chapter 5.

Chapter 5

Evaluation of the RadICAL Stack Detector

This chapter describes the work undertaken to evaluate the performance of the RadICAL stack detector for use in an active interrogation environment. This detector was designed to provide localisation of a neutron source within a high flux gamma background and consists of a stack of four stationary slabs of Eljen EJ299-33 plastic scintillator coupled to photomultipliers and mounted at an angular offset of 30° to each other around a central axis. The detector works by fitting the different count rate from each detector element to a previously acquired calibration Standard Response Curve (cSRC). By using Pulse Shape Discrimination (PSD) techniques it is possible to separately localise neutron and gamma events within a mixed field environment.

The detector was initially calibrated by acquiring cSRCs using a variety of gamma and neutron isotope sources as well as monoenergetic neutrons produced by a Van der Graaf Generator. PSD techniques were used to generate and compare separate cSRCs for each event type. The localisation technique was then tested by using the stationary detector to determine the direction of gamma and neutron isotope sources in a number of different positions.

5.1 Experimental Setup

The RadICAL Stack detector was set up for testing in two separate environments: the UCL Radiation Laboratory and the Neutron Metrology Group at the National Physical Laboratory. These two facilities provided a range of gamma and neutron sources and are described on the next page.

Figure 5.1: The RadICAL Stack detector setup in the UCL Radiation Physics laboratory.

5.1.1 UCL Radiation Laboratory

The detector was initially set up for testing within the UCL radiation laboratory. This allowed the detector to be calibrated and tested in a variety of configurations whilst exposed to a number of different low activity gamma sources over long periods of time.

In each configuration the detector was mounted by bolting the Newport URS100BPP rotation stage, attached to the bottom of the detector stack, to an optical bench. All cables and auxiliary equipment were positioned outside of the detectors 90 degree field of view, which left an area of around 3m x 3m for source positioning. This setup is shown in Figure 5.1. The source positions are not shown and are located to the left of the image.

5.1.2 National Physical Laboratory

Further experiments were conducted at the Neutron Metrology Group at the National Physical Laboratory (NPL) in Teddington over a limited period of time. This facility provided a number of different high activity gamma and neutron isotope sources as well as the use of a 3.5 MV Van der Graaff accelerator all within a low scatter environment. The facility is based around a central position that can be used as a radiation source via either an isotope or an accelerator target. This position is located at least 6m away from the floor, ceiling or the nearest wall with just lightly constructed supports designed to minimise the scatter of any measured photons or neutrons. Four mechanical arms are

positioned around the source location and can be used to precisely mount detectors and other equipment. Two moveable platforms allow access to the arms and can be used to mount auxiliary equipment. This facility is shown in Figure 5.2.

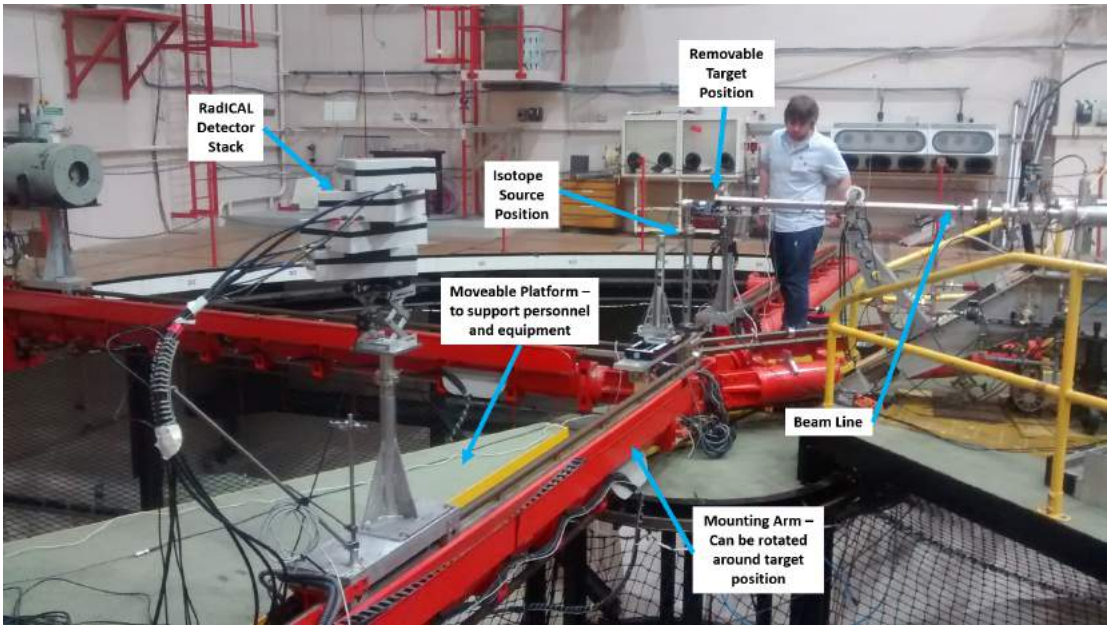

Figure 5.2: The NPL Neutron Metrology Groups low scatter facility.

The Van der Graaff accelerator is capable of providing mono-energetic fields covering the greater part of the energy range 50 keV to 5 MeV through charged particle interactions with a series of different targets. The neutron energy produced depends on the target material, the charged particle type and the angle at which the detector is located, relative to the particle beam. The available reactions are shown in Table 5.1.

Neutron Energy (MeV)	Reaction	Approximate Maximum Rates at 1m	
		Fluence $(cm^{-2}s^{-1})$	Ambient Dose Equivalent (μSvh^{-1})
0.144	$^{7}Li(p,n)\,^{7}Be$	1000	450
0.25	$^{7}Li(p,n)\,^{7}Be$	600	440
0.565	$^{7}Li(p,n)\,^{7}Be$	1600	2000
1.2	$T(p,n)^{3}He$	200	300
2.5	$T(p,n)^{3}He$	600	900
5	$D(d,n)^{3}He$	600	880

Table 5.1: Neutron reactions energies available at NPL.

The detector was mounted by bolting the Newport URS100BPP rotation stage at its base, via an adjustable stand, to one of the four mechanical arms which can be moved between precise positions within the environment. The stand was adjusted so that the

centre of the detector was vertically aligned with the set position for the isotope source or accelerator target. All cables and auxiliary equipment were placed on the outside of the detector, relative to the isotope or accelerator target position, to allow safe operation and minimise effects of unwanted attenuation and scatter. A wired connection between the control room and the equipment allowed for safe operation through remote control. A photograph of this setup is shown in Figure 5.3.

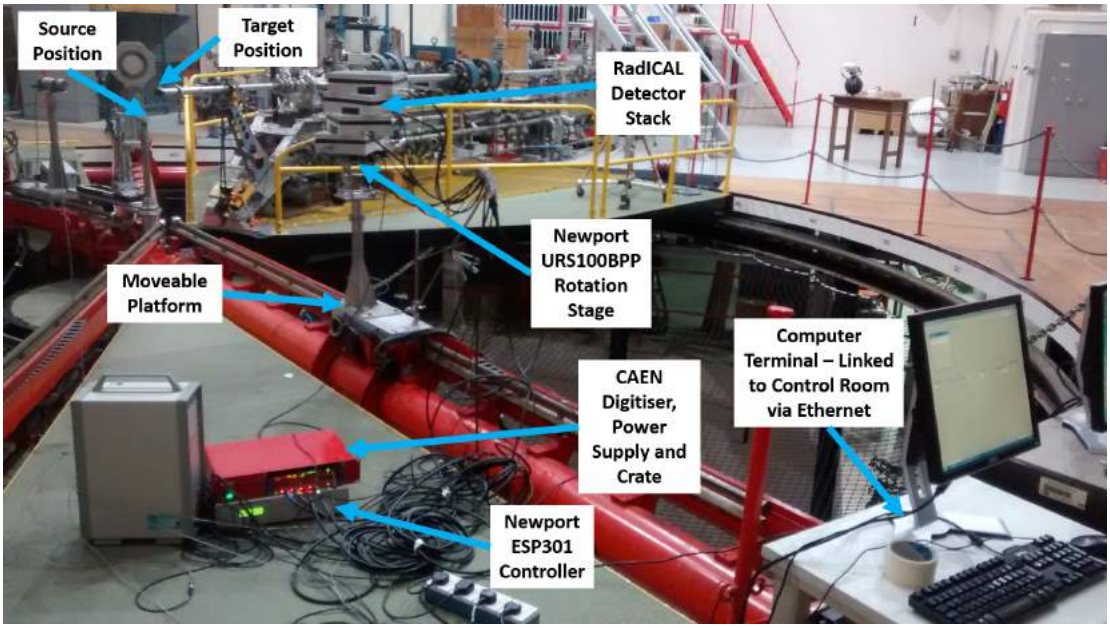

Figure 5.3: Experimental setup at NPL including detector, mounted on rotating stage, and isotope source on central mounting in low scatter environment.

5.2 Standard Response Curve Collection

Initial tests, conducted at both UCL and at NPL, involved positioning an isotope source, relative to a detector, so that a Standard Response Curve (SRC) was produced as the detector was rotated. This SRC could then be directly compared and used for subsequent source localisation investigations. Each acquisition was left for the longest practical time to minimise the effects of noise. This time varied depending on the activity of the sources and the time available for exposure.

In each case the source was kept vertically level with the central point of the detector. The detector was then rotated, in discrete steps, through a 270 degree sweep allowing each detector to acquire an SRC with at least 90 degrees either side of the minimum point. This allowed an equivalent 180 degree section of SRC in each case that could be directly compared.

A summary of the SRCs collected is shown in Table 5.2.

Source	^{137}Cs	^{241}Am	^{252}Cf	^{241}AmBe
Location	UCL	UCL	NPL	NPL
Date Started	30/12/2014	05/01/2015	20/01/2015	21/01/2015
Approx. Activity	3.7 MBq	70 MBq	150 MBq	370 GBq
Neutron Emission Rate	0	0	$1.80x10^7 s^{-1}$	$2.04x10^7 s^{-1}$
Distance from Detector	1.5 ± 0.01m	1.5 ± 0.01m	2.5 ± 0.01m	2.5 ± 0.01m
Step Angle	$0.5 \pm 0.18^\circ$	$1.0 \pm 0.18^\circ$	$1.0 \pm 0.18^\circ$	$1.0 \pm 0.18^\circ$
Live Time per Step	360s	180s	210s	210s
Max Counts per Step	$2.8x10^4$	$9.1x10^3$	$2.2x10^5$	$5.4x10^4$
Estimated Noise	167.3	95.4	469.0	232.4

Table 5.2: Details of SRC acquisitions and sources

5.2.1 Standard Response Curve Collection Method

5.2.1.1 Gamma Isotope SRC Collection

The sources initially used within the UCL laboratory were ^{137}Cs and ^{241}Am. With every step each detector acquired a full set of photon counts and energies.

The ^{137}Cs source had an activity of 3.7 MBq and was positioned 1.5 ± 0.01m from the central axis of the rotating detector. As this acquisition was conducted within the UCL Radiation Physics laboratory, and because the source was of relatively low activity, it was possible to acquire data over a longer period of time, with a smaller step angle, than with other sources. A total of 540 separate acquisitions were taken in 0.5 ± 0.18 degree steps and a live time of 360s was set for each step. This resulted in a total acquisition time of approximately 54 hours.

An ^{241}Am source of activity 70 MBq was positioned in the same location 1.5 ± 0.01m away relative to the central axis of the detector. Due to its high activity this source was housed within a lead container. The opening in the lead container was pointed directly at the central axis of rotation of the detector. 270 separate acquisitions were taken in 1 ± 0.18 degree steps and a live time of 180s was set for each step. This resulted in a total acquisition time of approximately 13.5 hours. Although the activity of this source was much higher than that of the ^{137}Cs used for the previous acquisition a much larger proportion of the emitted gammas were attenuated by the detector casing due to their low energy. This resulted in fewer counts per step than were seen in the ^{137}Cs acquisition.

5.2.1.2 High Activity Neutron/Gamma Isotope SRC Collection

Further SRCs were acquired using ^{241}Cf and ^{241}AmBe conducted at the National Physical Laboratory in Teddington in January 2015. Along with a time stamp and pulse height data, that corresponds to energy, each event was recorded with a PSD parameter, as described in Chapter 4.4.1, which could subsequently be used to distinguish neutrons from gamma events. The higher activity sources used at NPL, and the greater laboratory space available, allowed the detector to be placed at a greater distance of 2.5 ± 0.01m whilst maintaining a significant count rate, of more than 250 counts per second, on the detectors.

For each set of results SRCs from each of the four detectors were compared. All detector elements were designed to be identical but a difference in counting efficiency is likely due to imperfections in coupling the scintillator to the PMT. For each set of results the maximum and minimum points of each SRC were logged. These data were used to combine each result into a single SRC to which points could be fitted. This was done separately for each isotope response to allow for energy and particle dependent differences in SRC shape. Different photon energies have been predicted to result in a range of different SRC shapes for certain scintillator materials, as was previously discussed in Chapter 2.1.2. Neutrons may also result in a range of energy dependent SRC shapes due to the different mechanisms through which these particles interact with the scintillator.

5.2.2 Standard Response Curve Results

For each of the sets of data listed in Table 5.1 a set of 4 SRCs, corresponding with each of the stack detector elements, were plotted. These were the angle of each detector, relative to its starting position, plotted against its count rate in each position. These SRCs were initially used for direct comparison of each detector element under different experimental conditions. They were later used as calibration curves for fitting stationary detector count rates.

5.2.2.1 Comparison of Detector Elements

For each acquisition a slightly different overall counting rate was observed in each detector element. This was due to differences in detection efficiency due to imperfections in the manufacturing and coupling process. An example of the ^{137}Cs result is shown in

Figure 5.4.

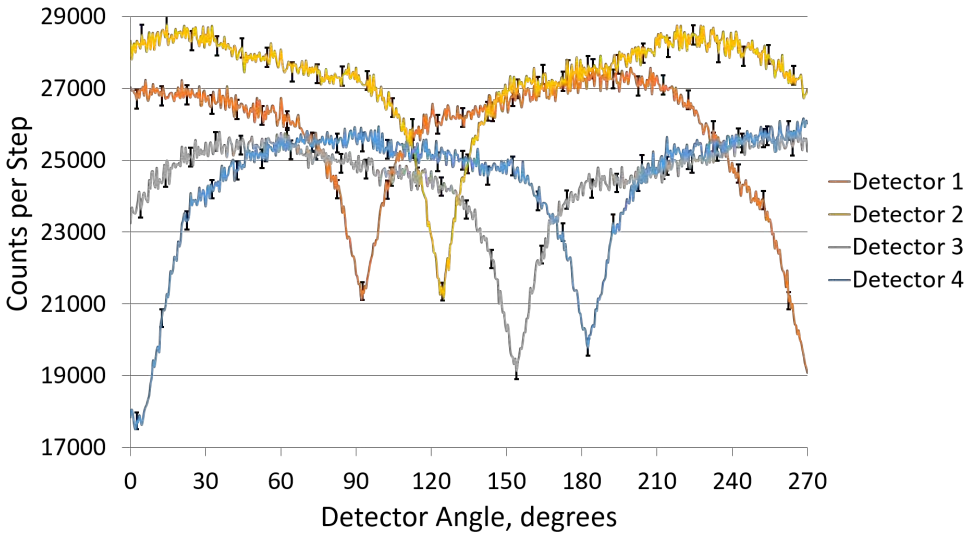

Figure 5.4: SRC for the 4 element stack exposed to 3.7MBq ^{137}Cs source positioned 1.5m from detector.

By comparing the count rate at each detector when exposed to the same source a scaling factor can be determined to provide a measure of the relative efficiency of each detector. These scaling factors can subsequently be used when fitting stationary detector points to a fixed curve.

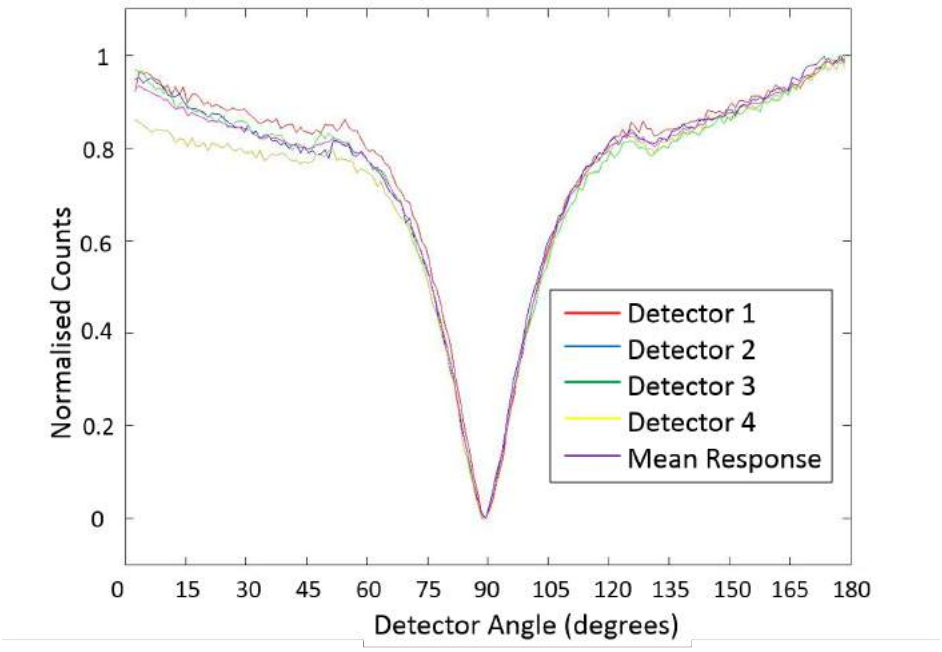

Figure 5.5: Normalised and aligned Standard Response Curves for all detector elements exposed to ^{252}Cf source.

Figure 5.5 shows the SRC, based on total undiscriminated events, of each detector exposed to the ^{252}Cf source. Each SRC has been normalised between its maximum and minimum points. The angular distributions have been aligned so that each SRC shows an equivalent 180 degree distribution centred around its minimum point. It can be seen that the normalised curves follow the same overall shape. Mean values of these results are shown on the plot. These values were later used as cSRCs for curve fitting.

Detector 4 shows a slightly lower count rate between 0 and 40 degrees. This is likely to do with slight attenuation of the power and signal cables as they pass between the detector and source.

5.2.2.2 Comparison of Results from Different Isotopes

As well as the difference in detection efficiency, which is consistent between multiple acquisitions and so easy to adjust for, there is an isotope dependent difference between the maximum and minimum point on each curve. This was previously discussed in Chapter 3 and is to do with the energy dependence of the paths that photons take as they travel through the detector. Table 5.3 shows a comparison of the average undiscriminated (n+γ) maximum and minimum counts for all of the detectors exposed to the sources summarised in Table 5.2.

Isotope	Max Counts per step	Min Counts per step	Max/Min
^{137}Cs	27097 ± 165	20320 ± 143	1.33 ± 0.02
^{241}AmBe	48626 ± 221	34477 ± 186	1.41 ± 0.01
^{252}Cf	90117 ± 300	62321 ± 250	1.45 ± 0.01
^{241}Am	8134 ± 90	4764 ± 69	1.71 ± 0.04

Table 5.3: Maximum and minimum average count rates (undiscriminated γ+n) for all detectors when exposed to each isotope.

It can be observed that, for undiscriminated events, the ratio of maximum and minimum, and therefore the shape of the curve, is different for each of the sources. The greatest similarity in this ratio is seen between the two neutron sources. A smaller ratio is observed at the higher energy ^{137}Cs source and a significantly larger ratio observed when the detector is exposed to the low energy ^{241}Am source.

Figure 5.6 shows the energy spectra from detector element 3 exposed to each of three different sources. This data was taken at NPL using the high activity ^{242}Cf and ^{241}AmBe sources described in Table 5.2 and a less active 161 kBq ^{137}Cs test source

positioned on the front of this detector. In each case the first 80,000 counts were used for a direct comparison of energy spectra. These values are not discriminated and so include both gamma energy and gamma equivalent neutron energy.

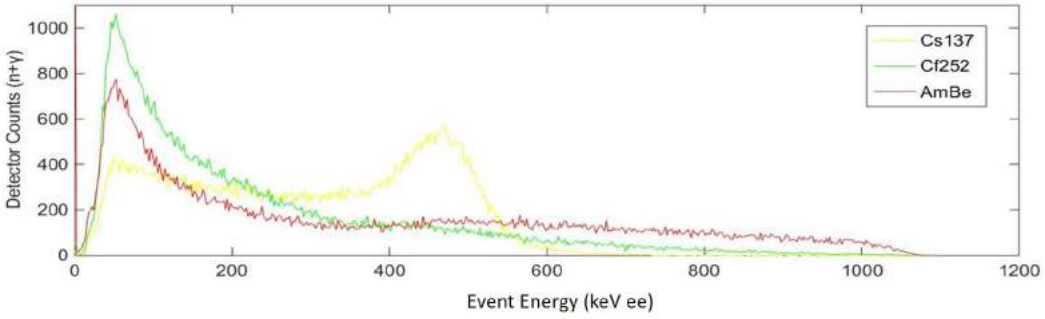

Figure 5.6: Energy spectra comparison for Detector Element 3 exposed to ^{137}Cs, ^{252}Cf and ^{241}AmBe sources.

The ^{137}Cs spectrum shows a clear Compton edge at 476 keV that was used for the energy calibration. The ^{252}Cf and ^{241}AmBe spectra are more complicated and both consist of a mixture of gammas and neutrons. The ^{252}Cf source produces neutrons and gammas predominantly through alpha decay. Neutrons are produced by this source at energies up to around 10 MeV but with a spectrum that peaks between 0.5 and 1 MeV. A number of high energy prompt gamma rays are also produced by this source [38]. The ^{241}AmBe source produces neutrons up to approximately 10 MeV with a peak energy of around 4 MeV and fewer gammas than those produced by the ^{252}Cf [103]. These distributions are seen in the spectra.

Figure 5.7 shows a comparison of SRCs from the bottom detector element exposed to each of the four sources. The count rate of each detector has been scaled for direct comparison. The energy dependent curve shapes can be clearly seen with the smallest difference in count rate observed in the high energy ^{137}Cs and the greatest seen in the ^{241}Am. This can be explained by a high proportion of the low energy photons attenuating in a small thickness of detector. At higher energies a greater proportion pass directly through and so the changing depth of attenuation, that counters the effect of changing exposed surface, becomes more significant.

Figure 5.8 shows these results normalised between a maximum and minimum value. It can be observed that, other than the different max-min ratios, the curve shapes closely match. The ^{241}Am count rate can be seen to drop slightly between 0 and 60

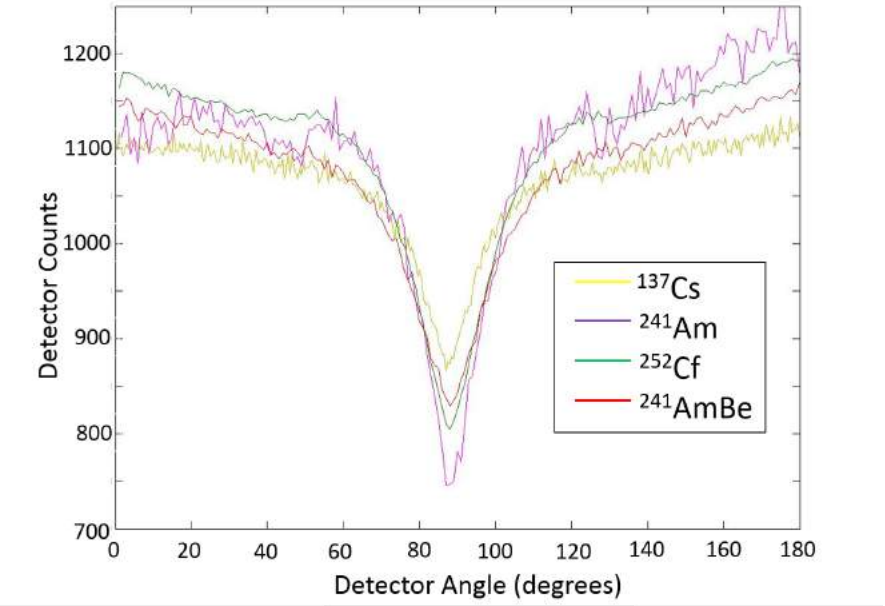

Figure 5.7: Standard Response Curves of Detector Element 1 exposed to ^{137}Cs, ^{241}AmB, ^{252}Cf and ^{241}AmBe sources.

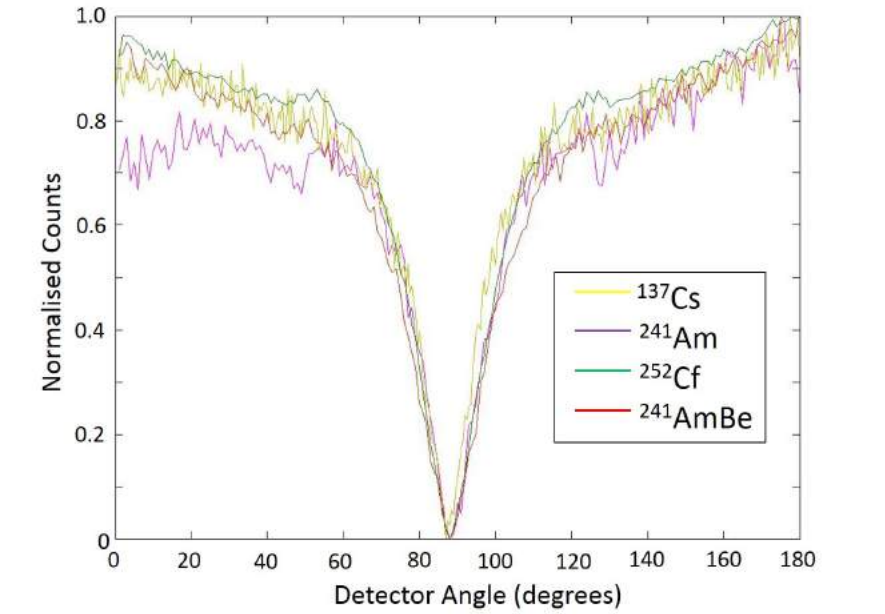

Figure 5.8: Normalised Standard Response Curves of Detector Element 1 exposed to ^{137}Cs, ^{241}Am, ^{252}Cf and ^{241}AmBe sources.

degrees in a manner similar to that seen in Figure 5.5. This can again be explained by the trailing cables passing between the source and detector at this point. The effect can be seen to be more significant due to the increased attenuation of the low energy photons.

5.3 Neutron/Gamma Discrimination Method

For the neutron data, taken at NPL, a CAEN 1751 digitiser was used with its associated Digital Pulse Processing for Pulse Shape Discrimination (DPP-PSD) software. By running the detectors through this digitiser and software each event is logged with a timestamp, pulse height and 'PSD number' which can subsequently be used to discriminate between neutrons and gamma events. This PSD number is achieved by assigning a long and a short timing gate to each event and finding the ratio between the integrated charge in the tail and total pulse as described in Chapter 4.

When pulse height, proportional to event energy, is plotted against PSD for each event from a mixed neutron/gamma field two clear plumes are formed as seen in Figure 5.9. These two plumes represent neutron and gamma events as labelled. Although some overlap is seen between plumes, particularly at lower energies, a cut-off value can be assigned at each energy based on a profile of the two plumes.

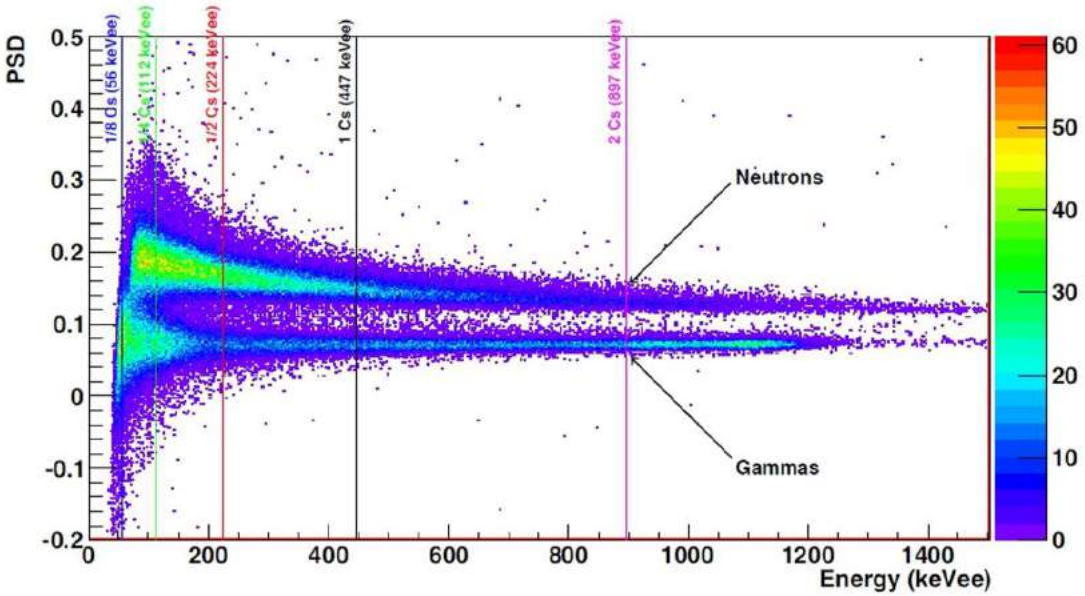

Figure 5.9: 2D plot of Energy vs PSD using BC501-A liquid scintillator and an ^{241}AmBe source at 2 kcounts/s. The data was acquired at Duke University (TUNL/CAEN website [98]).

5.3.1 Pulse Shape Discrimination Data Collection

A range of neutron and gamma only isotope sources were investigated at NPL. A plot of Energy versus PSD number is shown in Figure 5.10 for ^{137}Cs, ^{241}AmBe and ^{252}Cf isotope sources. For the ^{241}AmBe and ^{252}Cf neutron sources two clear plumes are

evident, these represent gamma and neutron events. Gamma only ^{137}Cs events are included to highlight the difference. A clear upwards trend shows in the plot as the event energy is raised. This is possibly due to nonlinearities in the light yield or may be a result of the high energy pulses exceeding the maximum dynamic range of the digitiser. Due to the limited time available for testing with neutron sources this was accepted but could possibly be addressed in the future by selecting an alternative PMT or running at a lower voltage.

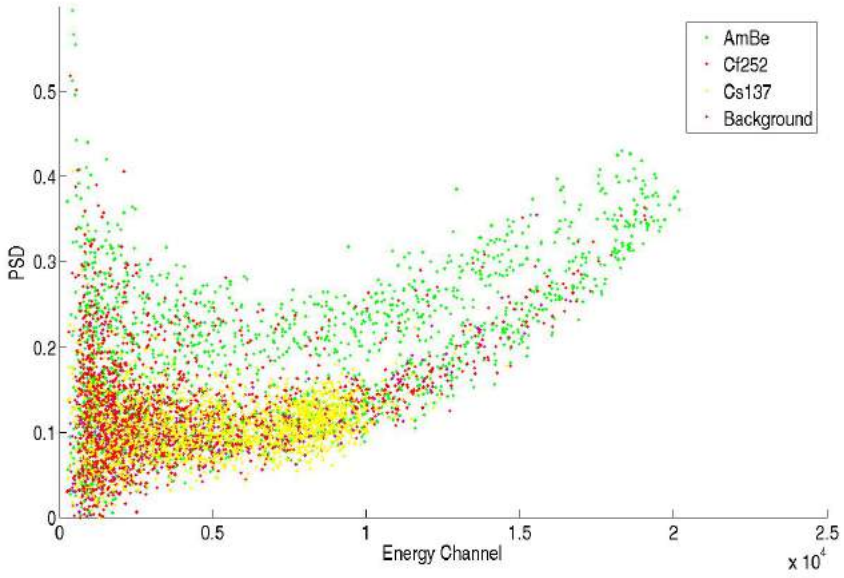

Figure 5.10: PSD-Energy plot for separate ^{137}Cs, ^{252}Cf and ^{241}AmBe results.

5.3.2 Determination of Discrimination Level

In order to discriminate separate neutron and gamma events it was necessary to determine an appropriate PSD number above which events could be assumed to be neutrons. This process was complicated by an observed overlap between neutron and gamma plumes, particularly at lower energies, and by curved shape of the plots apparent at higher energies.

Figure 5.11(a) shows a PSD-Energy intensity plot for detector 2 exposed to the same ^{252}Cf source over a long period of time. An intense gamma plume can be seen, with smaller neutron plume alongside. Figure 5.11(b) denotes a single energy profile cut through the plot as shown by the straight red line in figure 5.11(a). Profiles of this kind can be assumed to be a combination of two Gaussian distribution representing the separate plumes of gammas and neutrons.

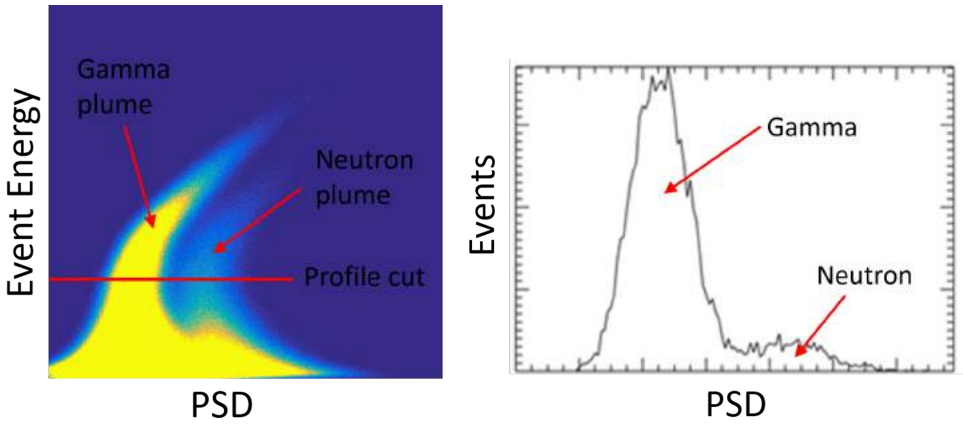

(a) Energy-PSD plot for mixed field. **(b)** PSD profile for single energy cut.

Figure 5.11: PSD vs Energy plot, for detector 2 exposed to ^{252}Cf, showing the two plumes associated with neutrons and gammas and intensity across red line shown.

For each detector the complete set of ^{252}Cf data was separated into energy bins to produce a large set of profiles similar to that shown in Figure 5.11(b). A Gaussian distribution was fitted to the dominant plume in each profile and the maximum position and standard deviation (sigma) were logged, in terms of PSD numbers.

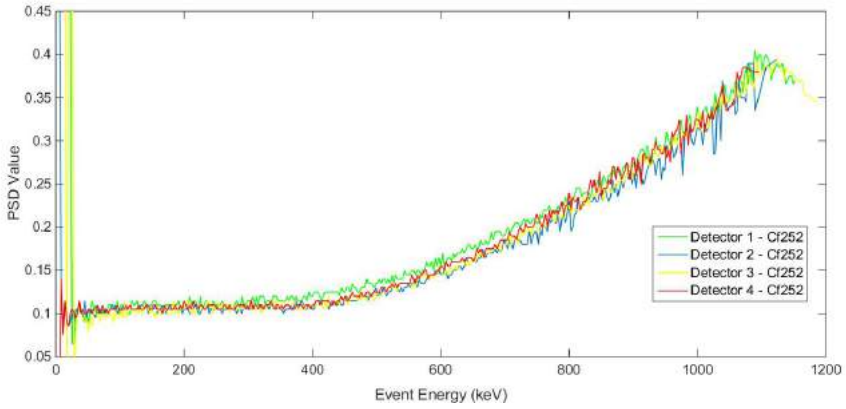

Figure 5.12: Maximum PSD value energy plot for ^{252}Cf results.

This process was repeated for each detector element exposed to the ^{252}Cf and ^{241}AmBe sources. Figure 5.12 shows each energy plotted against the maximum (most prevalent PSD) value for each detector element exposed to the ^{252}Cf source. A close agreement can be distinguished in each case. Slightly higher PSD values are observed between 300 and 700 keV for detector 1 than for the other three detectors. An equivalent plot was generated for the ^{241}AmBe source and is shown in Figure 5.13. This plot displays similar behaviour, with the occasional anomalous value resulting from incorrectly identified neutron plumes.

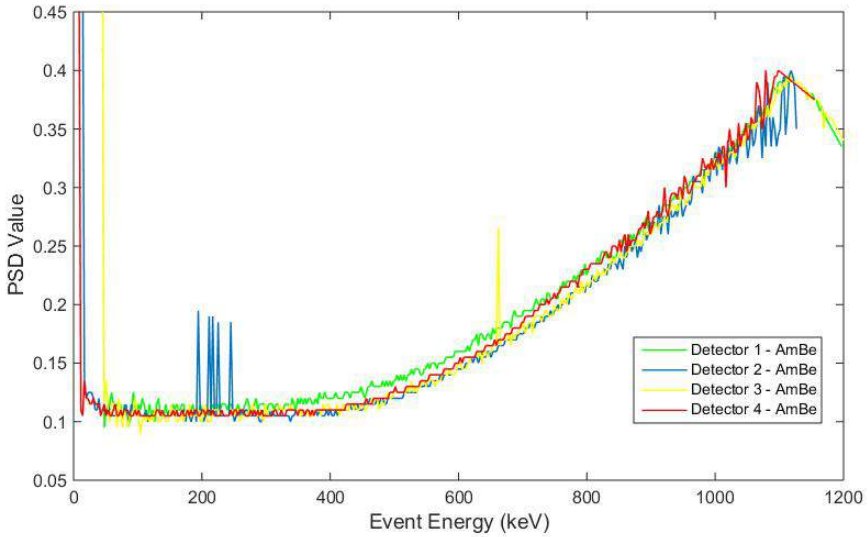

Figure 5.13: Maximum PSD value energy plot for ^{241}AmBe results.

Figure 5.14 shows an equivalent plot for detector Element 4 exposed to the ^{252}Cf and ^{241}AmBe sources. A close agreement can be observed for the two sources. The same agreement can be observed between the two sources for each of the four detector elements, including the same slight difference in PSD values observed between 300 and 700 keV in detector 1.

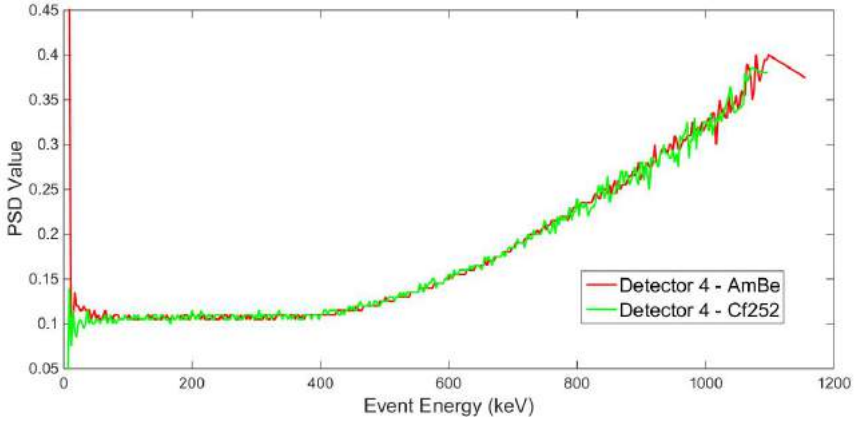

Figure 5.14: Maximum PSD value energy plot for detector 4 exposed to ^{252}Cf and ^{241}AmBe.

To determine an n/gamma discrimination value for each energy the maximum value was added to a set number of standard deviations. This variation was due to the overlap of neutron and gamma plumes and the specific multiple of sigma was chosen depending on the proportion of falsely identified neutrons considered acceptable. Figure 5.15 shows the results of Detector 1 exposed to the ^{241}AmBe source. Neutrons

and gamma regions are labelled separately with a 1 sigma separation point shown.

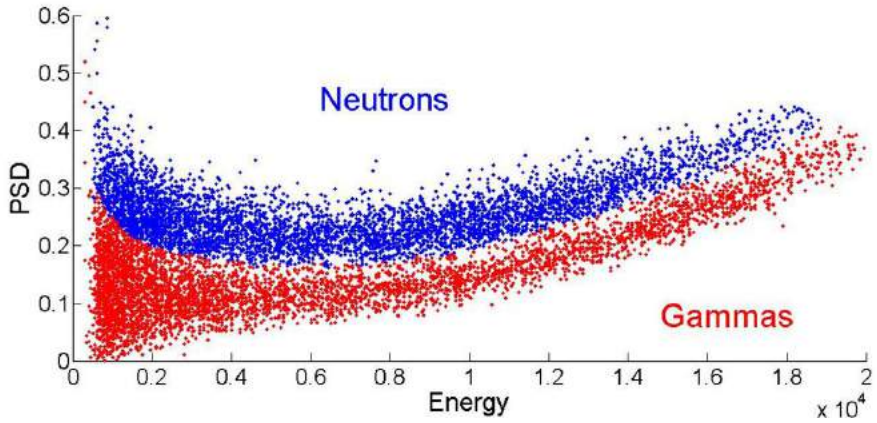

Figure 5.15: PSD plot of ^{241}AmBe source with 1 sigma separation point set and separate regions labelled

5.3.3 Discriminated Spectra

This technique was used to generate separate energy spectra for neutron and gamma events. Figure 5.16 shows a comparison of these spectra for detector 1 exposed to the ^{241}AmBe source based on a 1 sigma separation. This separation resulted in approximately 37.6 % of all events recorded as neutrons. The 1 sigma discriminated neutron plot of shows a peak at approximately 60 keV, this is likely to be due to misidentified gammas.

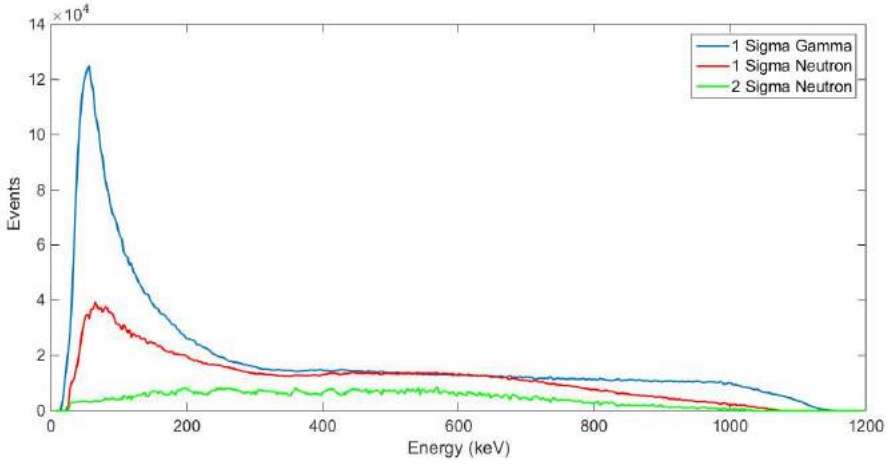

Figure 5.16: Energy spectra for discriminated neutrons and gammas from detector 1 exposed to ^{241}AmBe source with 1 sigma and 3 sigma separations

Neutrons from the same acquisition based on a 2 sigma separation are included on the same plot. These represent around 13.7 % of the total events. These results show

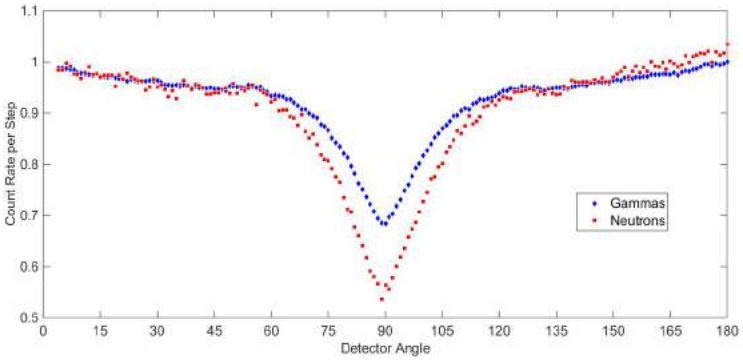

Figure 5.17: SRC discriminated neutrons and gammas from detector 1 exposed to ^{252}Cf source with 3 sigma separation

a wide distribution of gamma equivalent energies between 0 and 1 MeV that peaks around 400 keV.

5.3.4 Discriminated SRC Results

The same technique was used to generate separate sets of gamma and neutron SRCs for each set of results. Figure 5.17 shows separate gamma and neutron SRCs for the ^{252}Cf acquisition, described previously in Table 5.2. Each SRC was scaled to its maximum count rate for direct comparison. These results were based on a 3 sigma separation.

Based on this discrimination approximately 7.5 % of total events are identified as neutrons. Other than the different count rates the major difference observed between the two SRCs is that the ratio of the maximum and minimum neutron count rates observed in the 0 and 90 degree positions respectively is approximately 1.96:1 whereas the ratio of the gamma counts for the equivalent positions is approximately 1.43:1.

5.3.5 Neutron SRC in High Gamma Background

A further test was conducted using separate gamma and neutron isotope sources at the NPL Neutron Metrology Facility. This involved acquiring a response curve for neutron only events in a high gamma flux environment and will allow the localisation of a neutron source within a high flux gamma background.

5.3.5.1 Experimental Procedure

The same 150 MBq ^{252}Cf source as previously used was positioned 2.5m from the rotating axis of the detector stack. As with previous acquisitions the source was vertically aligned with the centre of the detector stack.

A second 370kBq ^{137}Cs source was positioned 25cm directly below the bottom detector enclosure, in line with the central axis of rotation. This resulted a high additional gamma flux on each of the detector elements which only changed a small amount as the detector rotated. This setup is seen in Figure 5.18.

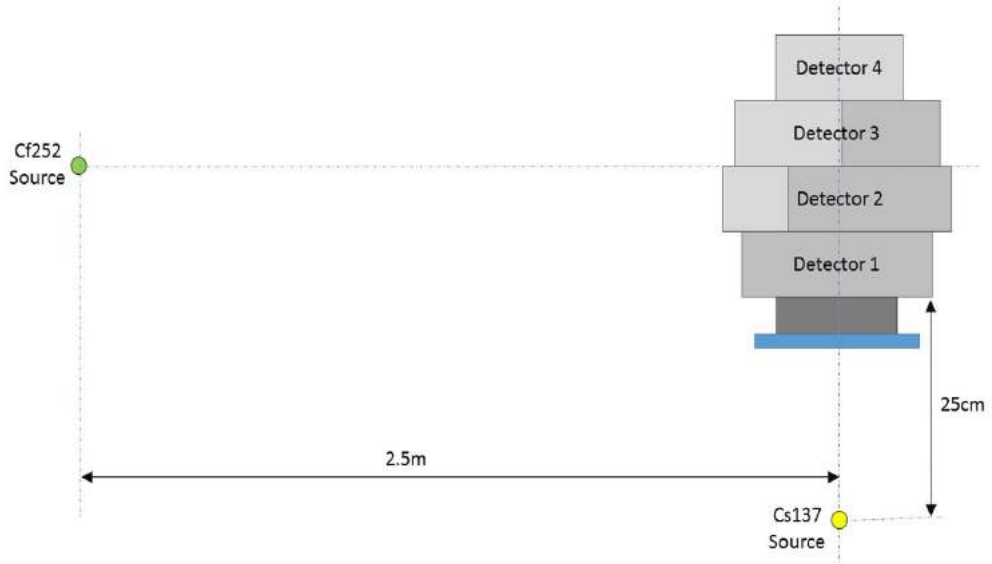

Figure 5.18: ^{252}Cf and ^{137}Cs source positions for finding neutron SRC in high gamma background.

With the sources in these positions the detector stack was rotated in 1 ± 0.18 degree steps around a total of 270 degrees. In each detector position an acquisition of 25s was taken with each element of the stack. This allowed the collection of an SRC from the ^{252}Cf source, as previously described, but with a separate gamma flux also detected from a different position.

5.3.5.2 Neutron in High Gamma Background SRC Results

By applying the neutron/gamma discrimination methods to these data it was possible to generate 2 sets of very different SRCs. A 2 sigma separation was used to reduce the occurrence of misidentified gamma events. A comparison of the neutron only, and undiscriminated, data for the bottom detector element (Detector 1) is shown in Figure 5.19. Both sets of results have been normalised between their maximum and minimum count rates to allow direct comparison of the curve shapes.

The neutron only data results in a curve shape similar to that seen in Figure 5.17. Direct comparison is difficult due to the high noise level that results from the limited counting time.

The undiscriminated data results in a far less predictable SRC with the extra gamma background causing major distortions in the shape of the curve.

The difference in these curve shapes suggests that by applying the discrimination method it is possible to locate a neutron source within a high gamma flux.

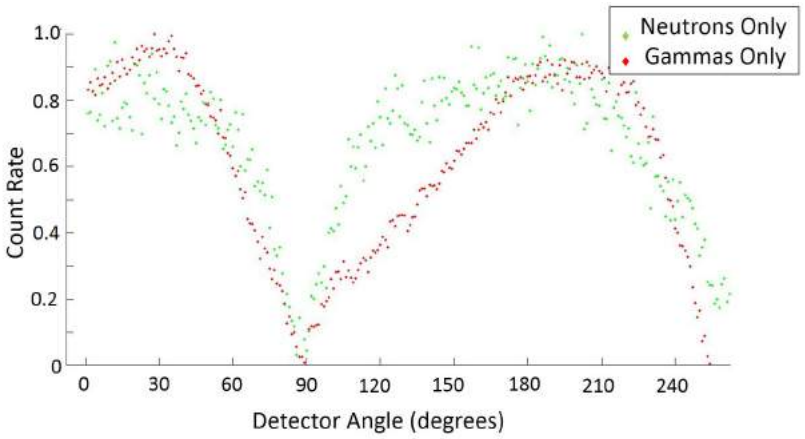

Figure 5.19: Gamma and neutron only SRCs for ^{252}Cf source in high gamma background.

5.3.6 Neutron Only Accelerator Investigation

In addition to the variety of gamma and neutron emitting isotope sources discussed earlier the Neutron Metrology department at the National Physical Laboratory also provided the use of a 3.5 MV Van der Graaff generator. By using this accelerator to bombard a variety of different targets with either protons or deuterons it was possible to produce a high, monoenergetic, flux of intermediate and fast neutrons at energies between 50 keV and 5 MeV with a relatively low gamma background. A wider range of precisely calibrated energies were accessible by adjusting the angle of the detector, relative to the direction of the charged particle beam.

5.3.6.1 Accelerator Investigation Method

The detector stack was positioned 3.10 ± 0.01 m from the target and by using different combinations of targets and angles it was possible to achieve precise monoenergetic neutron flux at energies of 1.3 MeV, 1.8 MeV, 2.0 MeV and 3.8 MeV in order to cover a range of the neutron energies available. The reaction type and the angle at which the detector was positioned, relative to the incident charged particle beam on the target, that corresponded to each energy is shown in Table 5.4. As with previous isotope investigations the detector was positioned so that its vertically central point was alligned

Reaction	Angle (Detector-Incident Beam)	Neutron Energy
T(p,n) ^{3}He	60 degrees	1.295 MeV
T(p,n) ^{3}He	30 degrees	1.789 MeV
T(p,n) ^{3}He	0 degrees	2.005 MeV
D(d,n) ^{3}He	60 degrees	3.809 MeV

Table 5.4: Neutron energies achieved at using Van der Graaf accelerator at NPL.

with the the neutron target. For each energy the detector stack was moved in 1 ± 0.18 degree steps of 6 second duration around a total rotation of 310 degrees. This allowed the collection of neutron SRCs over a total acquisition time of 31 minutes for each energy.

5.3.6.2 Neutron Only Accelerator PSD Results

Figures 5.20 show PSD plots for the 2 lower, 1.30 MeV and 1.79 MeV neutron energies that were investigated. This data can be used to provide a neutron energy calibration and to gain a better understanding of the optimum position for the n/gamma separation point. In each image there is just a small plume of gamma events showing, relative to the more intense neutron plume.

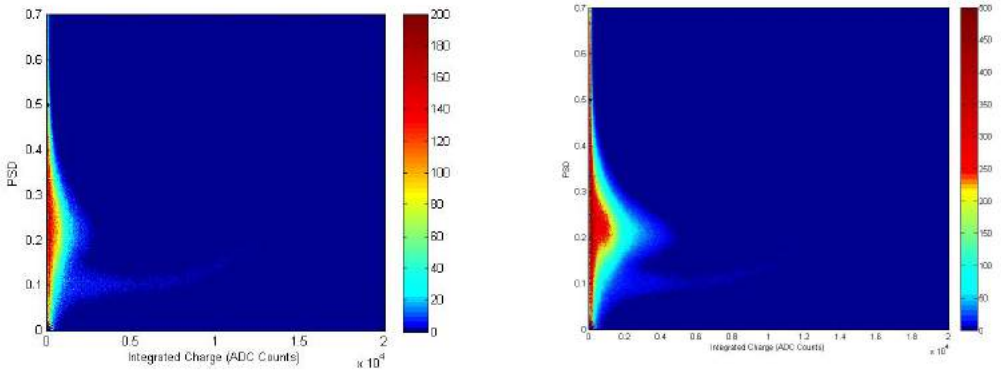

(a) 1.295 MeV Neutrons **(b)** 1.7888 MeV Neutrons

Figure 5.20: Monoenergetic neutrons from accelerator Source

Figure 5.21 shows the higher, 2.00 MeV and 3.81 MeV, energies that were investigated. Gamma plumes are apparent in each plot but this component is much more intense in the 3.81 MeV plot.

Figure 5.22 shows a scatter distribution of energy against PSD number for each of these four results. The energy deposited by each neutron source can be seen in four

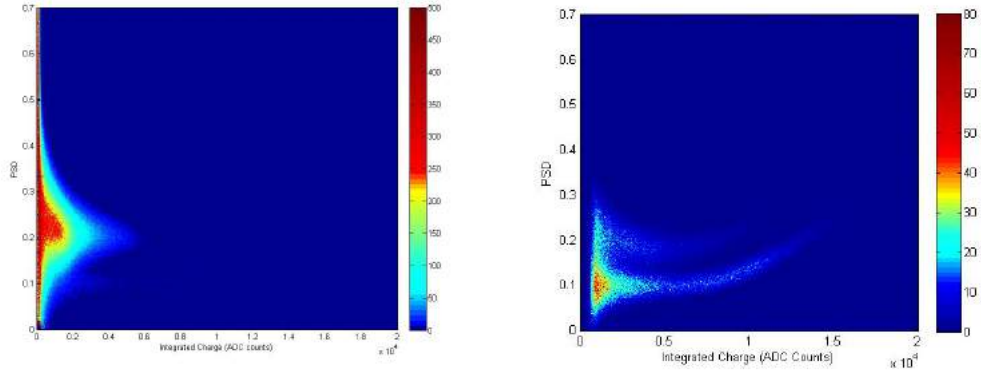

(a) 2.0046 MeV Neutrons **(b)** 3.809 MeV Neutrons

Figure 5.21: Monoenergetic neutrons from accelerator source

different regions. In each case the gamma plume is seen to follow a similar distribution.

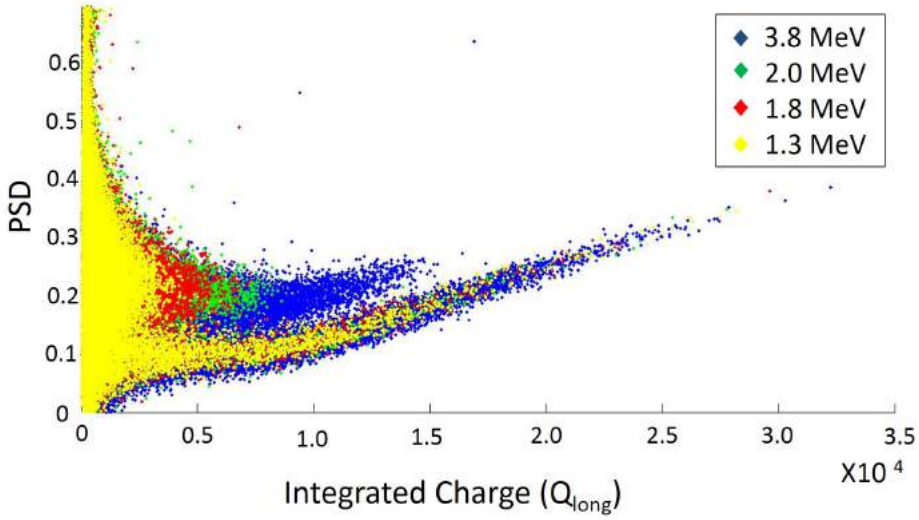

Figure 5.22: PSD-Energy plot comparison of 4 different monoenergetic neutron sources.

5.3.6.3 Standard Response Curves for Accelerator Data

Standard response curves were plotted for each detector in the stack at a each incident neutron energy. This resulted in 16 separate SRCs. Figure 5.23 shows the result of detector 2 exposed to 1.8 MeV neutrons.

Due to the limited amount of time available for use of the Van der Graaf generator it was not possible to achieve less noisy results. In each result there is also a sudden drop in count rate as seen between 140 and 150 degrees on Figure 5.23. This phenomena occurs for the same time on each of the four detectors and so is likely to be a result of a fault with the generator, rather than the detection system.

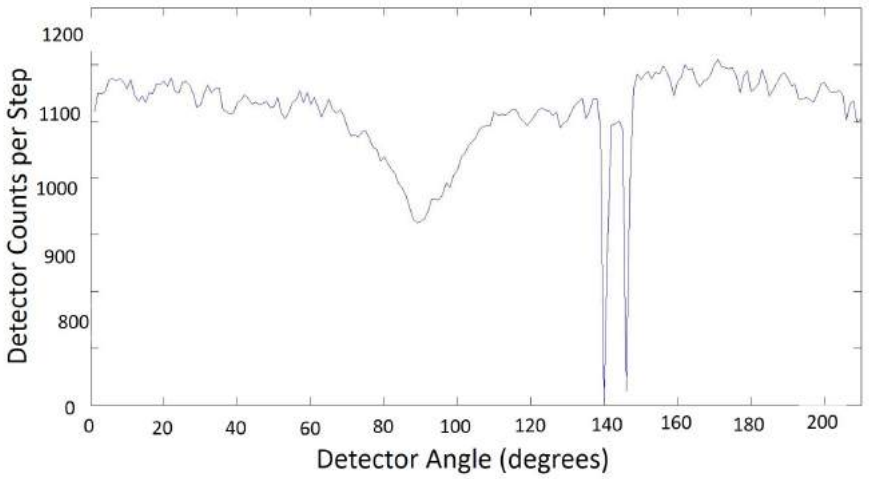

Figure 5.23: SRC for detector 2 exposed to 1.8 MeV neutrons

Figure 5.24 shows a comparison of SRCs for the undiscriminated 1.8 MeV accelerator source neutrons and the discriminated neutron only data from the ^{252}Cf source, based on 3 sigma separation.

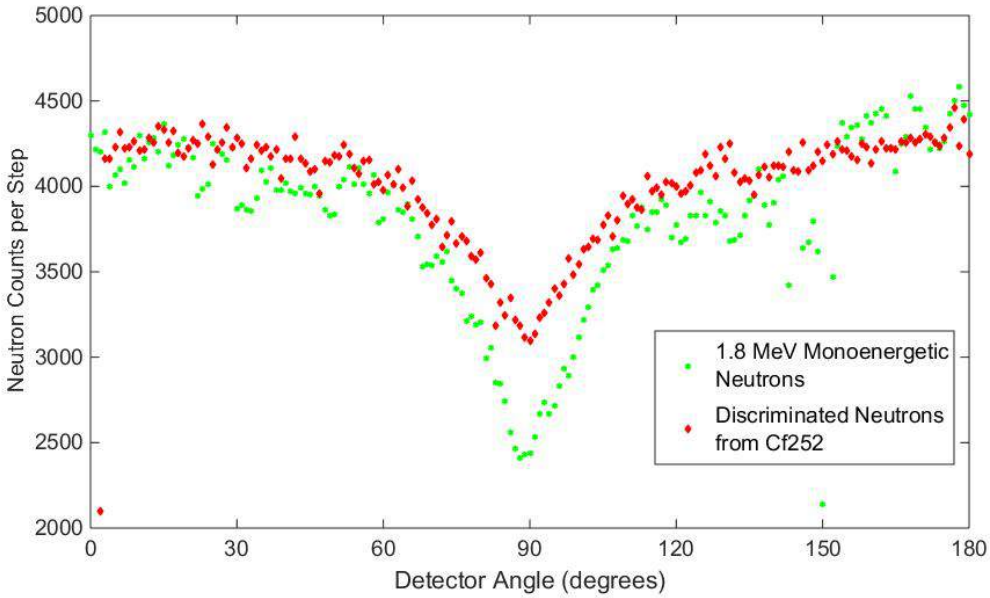

Figure 5.24: Comparison of SRC for detector element 2 from 1.8 MeV neutrons from accelerator and discriminated neutrons from ^{252}Cf.

5.4 Source Localisation

A localisation method was developed to determine the direction of the source using the SRCs previously acquired. This is described on the next page.

5.4.1 Source Localisation Curve Fitting Method

The localisation method was tested by fitting the cSRCs recorded in Section 5.2 to count rates determined for each source location. This method was a variation of that described in section 4.2.1 but with consideration made for the different efficiency of each detector. The method is described below:

- Counts rates were multiplied by a scaling factor that corresponded to the counting efficiency of each detector, as determined in Section 5.2.2.1, to allow them to be directly compared.
- These four adjusted count rates were then scaled to fit the count rate of the cSRC. This was done by using the detector with the maximum detected counts to estimate the maximum point on the curve and the max/min ratio of the cSRC to estimate the minimum point.
- These scaled detector points were then plotted on top the cSRC, separated at angles that correspond to the angular separation of detectors as shown in Figure 5.25.
- These positions were moved along the x-axis of the plot and the closest fit was found, using a least squares method, in order to find the direction of the source.

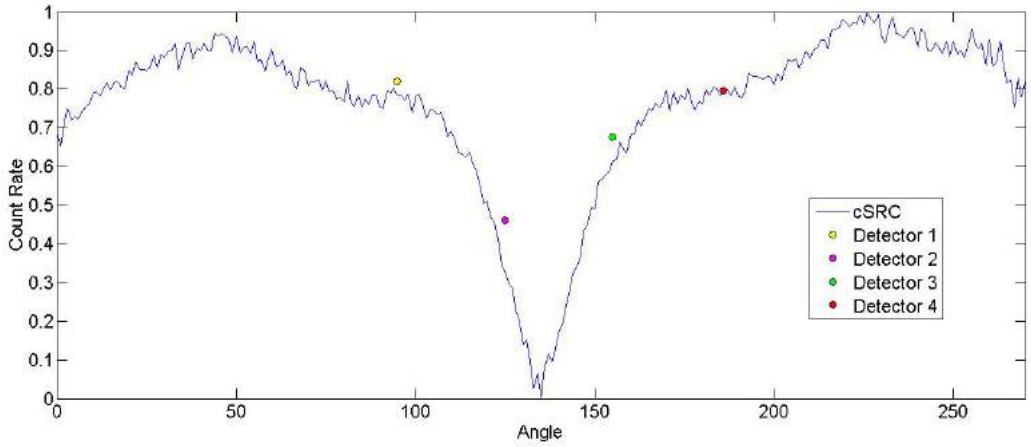

Figure 5.25: Normalised standard response of rotating detector and fitted points.

5.4.2 Low Activity Gamma Source Localisation

In order to test the method of source localisation using the stationary stack of detectors it was necessary to move each source to various positions within the field of view of

the stationary detector and compare the detected angle of the source with the physically measured position. The stack detector was initially tested within the UCL radiation laboratory using a ^{137}Cs source.

5.4.2.1 Low Activity Gamma Source Localisation Test Procedure

The detector stack was kept stationary, in a known position, and the same 3.7 MBq ^{137}Cs source used for SRC collection was moved between 24 different locations within the detector's field of view. These positions are shown in Figure 5.26. In each position the source was held vertically level with the centre of the detector on a perspex platform in order to minimise scatter.

For each acquisition the source was kept stationary and each of the detectors took a 10, 100 and 1000 second acquisition so that the effect of different counting statistics could be compared.

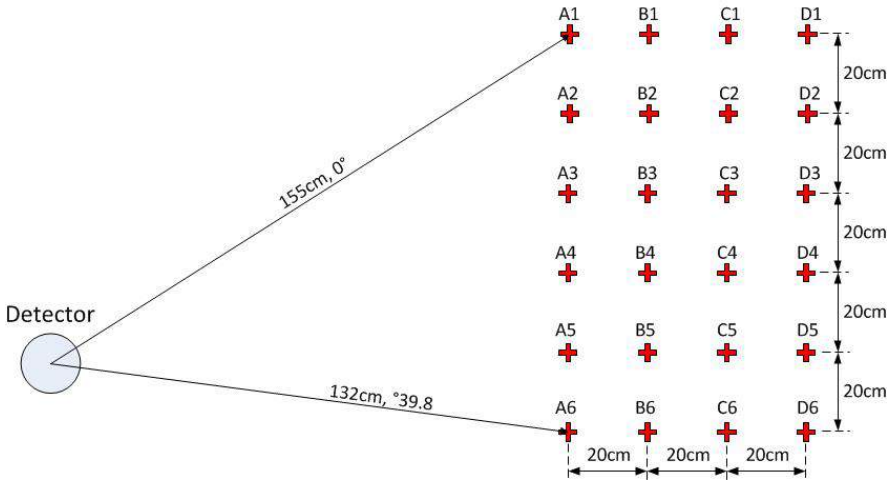

Figure 5.26: Position of 137Cs source, relative to stationary detector.

For each source position and time bin the stationary detector counts were compared to the cSRC using the method described in Section 5.5.1.

5.4.2.2 Low Activity Gamma Localisation Investigation Results

The curve fitting technique described above resulted in a predicted position for each source location and time bin. These positions could then be directly compared to the measured source locations. These results are shown in Table 5.5.

These results showed the localisation ability of the stack detector for the first time and was able to achieve an angular resolution of 4.4 ± 0.3 degrees in between 100s and 1000s which translates as around 500-5000 registered events per detector element.

Source Position	Measured Position (Source to Detector Centre)		Predicted Differece to Measured Angle (degrees)		
	Angle	Distance	10s	100s	1000s
A1	$0.0 \pm 0.4°$	155 ± 1cm	$10.6 \pm 0.4°$	$9.4 \pm 0.4°$	$8.4 \pm 0.4°$
A2	$6.7 \pm 0.4°$	145 ± 1cm	$16.1 \pm 0.4°$	$0.1 \pm 0.4°$	$1.9 \pm 0.4°$
A3	$14.2 \pm 0.4°$	138 ± 1cm	$22.6 \pm 0.4°$	$1.6 \pm 0.4°$	$2.6 \pm 0.4°$
A4	$22.4 \pm 0.4°$	133 ± 1cm	$4.8 \pm 0.4°$	$23.2 \pm 0.4°$	$3.8 \pm 0.4°$
A5	$31.1 \pm 0.4°$	131 ± 1cm	$48.5 \pm 0.4°$	$5.5 \pm 0.4°$	$8.5 \pm 0.4°$
A6	$39.8 \pm 0.4°$	132 ± 1cm	$0.2 \pm 0.4°$	$1.8 \pm 0.4°$	$2.2 \pm 0.4°$
B1	$4.3 \pm 0.3°$	174 ± 1cm	$5.3 \pm 0.3°$	$11.7 \pm 0.3°$	$7.7 \pm 0.3°$
B2	$10.3 \pm 0.3°$	164 ± 1cm	$14.3 \pm 0.3°$	$4.7 \pm 0.3°$	$0.3 \pm 0.3°$
B3	$17.1 \pm 0.4°$	158 ± 1cm	$0.5 \pm 0.4°$	$0.5 \pm 0.4°$	$6.5 \pm 0.4°$
B4	$24.1 \pm 0.4°$	153 ± 1cm	$13.5 \pm 0.4°$	$5.5 \pm 0.4°$	$5.5 \pm 0.4°$
B5	$31.9 \pm 0.4°$	152 ± 1cm	$2.7 \pm 0.4°$	$8.3 \pm 0.4°$	$6.7 \pm 0.4°$
B6	$39.0 \pm 0.4°$	152 ± 1cm	$17.4 \pm 0.4°$	$0.6 \pm 0.4°$	$2.4 \pm 0.4°$
C1	$6.8 \pm 0.3°$	191 ± 1cm	$15.8 \pm 0.3°$	$2.8 \pm 0.3°$	$3.8 \pm 0.3°$
C2	$12.6 \pm 0.3°$	183 ± 1cm	$4.0 \pm 0.3°$	$1.0 \pm 0.3°$	$2.0 \pm 0.3°$
C3	$18.9 \pm 0.3°$	177 ± 1cm	$3.7 \pm 0.3°$	$7.3 \pm 0.3°$	$2.3 \pm 0.3°$
C4	$25.1 \pm 0.3°$	173 ± 1cm	$16.5 \pm 0.3°$	$5.5 \pm 0.3°$	$6.5 \pm 0.3°$
C5	$32.0 \pm 0.3°$	172 ± 1cm	$8.4 \pm 0.3°$	$8.6 \pm 0.3°$	$7.6 \pm 0.3°$
C6	$38.6 \pm 0.3°$	172 ± 1cm	$2.5 \pm 0.3°$	$1.0 \pm 0.3°$	$0 \pm 0.3°$
D1	$9.4 \pm 0.3°$	210 ± 1cm	$28.2 \pm 0.3°$	$2.2 \pm 0.3°$	$0.2 \pm 0.3°$
D2	$14.0 \pm 0.3°$	202 ± 1cm	$6.4 \pm 0.3°$	$3.4 \pm 0.3°$	$1.6 \pm 0.3°$
D3	$20.3 \pm 0.3°$	196 ± 1cm	$0.7 \pm 0.3°$	$22.3 \pm 0.3°$	$2.7 \pm 0.3°$
D4	$26.0 \pm 0.3°$	193 ± 1cm	$14.6 \pm 0.3°$	$7.4 \pm 0.3°$	$13.6 \pm 0.3°$
D5	$32.3 \pm 0.3°$	191 ± 1cm	$11.7 \pm 0.3°$	$8.7 \pm 0.3°$	$7.3 \pm 0.3°$
D6	$38.4 \pm 0.3°$	192 ± 1cm	$16.8 \pm 0.3°$	$3.2 \pm 0.3°$	$1.2 \pm 0.3°$
Mean Difference (degrees)			$11.9 \pm 0.3°$	$6.1 \pm 0.3°$	$4.4 \pm 0.3°$

Table 5.5: Undiscriminated gamma localisation results for 1.76 MBq ^{137}Cs source exposed to detector. 24 source locations and 3 acquisition times shown.

5.4.3 Neutron/Gamma Source Localisation

Using a combination of the curve fitting method described in Section 5.5.1 and the discrimination method described in Section 5.3 it was possible to locate neutron and gamma sources separately.

5.4.3.1 Neutron/Gamma Localisation Curve Fitting Method

The same curve fitting method described in Section 5.5.1 was used for localising a neutron source within a mixed field. Discriminated neutron cSRCs, such as that shown in Figure 5.17, were used to fit discriminated neutron counts from each stationary detector stack element. The same discrimination levels, as described in Section 5.3.2 were used

for each detector throughout the investigation.

5.4.3.2 N/Gamma Localisation Investigation

An experimental procedure, similar to that described in Section 5.5.2, was conducted at the National Physical Laboratory's Neutron Facility using the 150MBq ^{252}Cf source.

Within the NPL neutron laboratory it was not practical, or safe, to continuously move the sources around the test area relative to the detector. Instead the source was left in position on its central mounting and the detector was moved up and down along the length of the mechanical arm, on which it was mounted, and was rotated into various different fixed positions.

This allowed for individual count rates to be taken in the same manner as if the source had been moved. Each resulting isotope position, relative to the detector, is shown in Figure 5.27. The Cf-252 source was used for these acquisitions and a total of 10 different source positions were investigated. Each event was logged with a timestamp, energy and PSD number. The event timestamps were then used to separate each acquisition into time bins of 0.1, 1, 10, 100 and 1000 seconds. The total number of counts from each detector, within each of these time bins, provided five separate data sets for analysis which could then be compared.

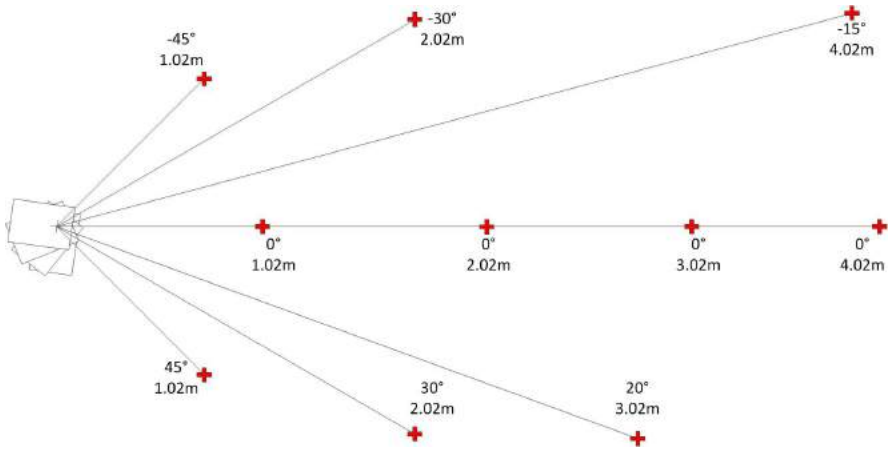

Figure 5.27: Plan of source positions, relative to stationary detector.

The PSD and curve fitting methods were then used to separate the neutrons and gamma events. Each set of data was then used separately to determine the direction of the source.

5.4.3.3 N/Gamma Localisation Results

The results from this investigation are shown in Table 5.6 below. These were determined by comparing the neutron only data to the neutron only cSRC and the undiscriminated events to the original cSRC (n + gamma). A PSD separation point of 3 sigma was used, for both the cSRC and the stationary positions, to discriminate and minimise the false identification of neutrons.

Distance (m)	Angle (degrees)	Accuracy of Predicted Position - Angular Difference in Detected and Measured Position (Degrees)					
		Total Events			Neutrons		
		0.1s	10s	1000s	0.1s	10s	1000s
1 ±0.01	0 ±0.57	11 ±0.57	0 ±0.57	0 ±0.57	21 ±0.57	1 ±0.57	1 ±0.57
1 ±0.01	-45 ±0.57	3 ±0.57	14 ±0.57	4 ±0.57	39 ±0.57	3 ±0.57	2 ±0.57
1 ±0.01	45 ±0.57	20 ±0.57	7 ±0.57	10 ±0.57	26.5 ±0.57	0 ±0.57	3 ±0.57
2 ±0.01	0 ±0.29	4 ±0.29	2 ±0.29	0 ±0.29	0 ±0.29	5 ±0.29	2 ±0.29
2 ±0.01	-30 ±0.29	9 ±0.29	3 ±0.29	3 ±0.29	32 ±0.29	8 ±0.29	2 ±0.29
2 ±0.01	30 ±0.29	15 ±0.29	3 ±0.29	9 ±0.29	19.5 ±0.29	12.5 ±0.29	9 ±0.29
3 ±0.01	0 ±0.19	8 ±0.19	8 ±0.19	0 ±0.19	10 ±0.19	1 ±0.19	1 ±0.19
3 ±0.01	20 ±0.19	15 ±0.19	9 ±0.19	2 ±0.19	13 ±0.19	10 ±0.19	4.5 ±0.19
4 ±0.01	0 ±0.14	14.5 ±0.14	0 ±0.14	6 ±0.14	17 ±0.14	9 ±0.14	1 ±0.14
4 ±0.01	-15 ±0.14	6 ±0.14	6 ±0.14	5 ±0.14	26 ±0.14	11 ±0.14	4 ±0.14
Mean Difference		10.55 ±0.32	5.20 ±0.32	3.90 ±0.32	20.90 ±0.32	5.75 ±0.32	2.95 ±0.32

Table 5.6: Undiscriminated and discriminated neutron only localisation results for 1.76 MBq ^{252}Cf source exposed to detector. 10 source locations and 3 acquisition times shown.

The results show that neutron only imaging is possible and positional accuracy of 2.95 ± 0.32 degrees was achievable for the event rate shown. For the shorter acquisition time greater accuracy was shown for mixed gamma and neutron events. As the acquisition time was increased the accuracy of the neutron only events began to surpass that of the undiscriminated field. This is due to the effect of the more pronounced curve shape

becoming more significant as counting statistics decrease.

5.5 Summary

SRCs have been obtained for the detector stack exposed to a variety of different gamma and neutron sources. These take on a shape that is determined by the dimensions and the type of the scintillator. The count rate is dependent upon the type and energy of incident flux and the location of the source.

Pulse shape discrimination techniques have been used to separate neutron and gamma events within detector elements. A clear separation is seen between gamma and neutron events when the PSD is plotted against the event energy, although some overlap is observed particularly at low energies. Plots of this type have been obtained from a variety of isotope and accelerator sources.

An imaging technique has been developed to determine the direction of a source using discriminated gamma and neutron events. The detector has been used to locate a 1.76 MBq ^{137}Cs source to within $4.4 \pm 0.3^{\circ}$ at distances of 1.52-2.10m using gamma events. The same detector has been used to locate a 150 MBq ^{252}Cf source at distances of 1.02-4.02m to within $2.95 \pm 0.32^{\circ}$ using neutron only events and to within $3.90 \pm 0.32^{\circ}$ using combined gamma and neutron events. This offers an alternative to the, previously discussed, RadICAL technique that may be suitable for source localisation during Active Interrogation.

Chapter 6

Conclusions and Future Work

The methods and results of a study into the development of a directional detection system suitable for use in mixed field environments is presented in this thesis. The project's aim was to develop a detector capable of locating a source of neutrons within a high flux, mixed field, active interrogation environment using pulse shape discrimination techniques.

6.1 General Conclusions

6.1.1 Modelling

The initial modelling results, described in Section 2.1, predicted that a rotating slab of scintillator will produce a characteristic response curve that can be used to determine the direction of a gamma source.

The shape of this response curve will depend on the shape and material of the detector and the energy of the incident photons. The major factors effecting the shape of the response curve are the dimensions of the scintillator. Assuming that the scintillator forms a rectangular slab the shape of the response curve, and therefore the directional ability of the detector, is governed by the aspect ratio between the large and small dimensions of the crystal. The other factors that influence the shape of the response curve is the attenuation coefficient of the detector material. This is determined by a combination of the detector material and the energy of the photons being detected. For a given detector geometry and material the SRC shape converges to a specific shape below a specific energy threshold. This corresponds to all events interacting within the detector regardless of the angle so that the dominant factor that determines the SRC

shape is the solid angle subtended by the slab. Above a high energy threshold the SRC shape again begins to converge. This corresponds to a large majority of incident gammas passing directly through the detector with the signal determined by just a small proportion. Above this value changes in attenuation depth only result in a small change in signal, relative to changing solid angle. Between these thresholds the attenuation depth, that changes as the detector rotates, becomes a significant factor in determining the shape of the SRC.

Further models involved Monte Carlo simulations using the Geant4 code. These showed close correlation with the previously described simple model. This code was then used to investigate how the SRC shape changes as the detector is moved closer to the source. This demonstrated a minimum distance, between the detector and the source above which the incident flux can be considered to be a parallel beam and the SRC shape remains uniform.

Subsequent models introduced the production of optical photons through the scintillation process and their transport to a photodetector. This modelling was used to determine an optimum position for mounting the photodetector, in terms of light collection and to minimise the spread of optical photon path lengths that could adversely effect the PSD abilities of the detector. This work was used to determine an optimum position for the photodetector.

6.1.2 The RadICAL Detector

Three separate detector systems were built based around the RadICAL detector concept using different geometries of CsI(Na) and Eljen EJ200 plastic scintillator. These were tested using a variety of different gamma sources and were demonstrated to produce response curves similar to those shown in the model.

Each detector was then assessed for energy resolution, source direction accuracy and source direction precision. The energy resolution for each detector depended upon the material and geometry of the scintillator. The 100x100x5mm CsI(Na) crystal was shown to possess an energy resolution of 18-19 % at 662 keV and the smaller 40x40x3mm CsI(Na) crystal demonstrated an energy resolution of approximately 15-16 % at the same energy. The difference in energy resolution may be due to the different size of each detector or may also be due to the degradation of each detector due to dif-

ferent times spent exposed to air. The 140x150x12.7 Eljen EJ200 detector does not possess any measurable energy resolution.

For each detector the SRC was compared to that generated by the models. In each case the experimental results demonstrate a similar shape to that seen in the models but show a smaller count rate in the 0° (maximum) position and greater in the 90° (minimum) position. Differences may be due to poor detector efficiency, inefficient light collection, background radiation and light leakage.

The 5x100x100mm CsI(Na) detector was then used to locate a 500MBq Cs137 source over a variety of different positions within a 7 x 13m area. It was possible to locate the source to within a mean angle of $1.58 \pm 1.12°$.

A similar investigation was then conducted using 2 separate detectors to locate a source within a 60cmx60cm 2-dimensional plain. It was shown that the two detectors could locate a source to $45 \pm 29.1mm$.

A further investigation involved locating separate sources simultaneously by examining counts within different energy windows using a single detector. Using this method it was possible to locate each source to within a mean difference of $0.63 \pm 2.60°$.

A final set of experiments involved converting one of the RadICAL detectors for current mode operation. When exposed to a single gamma source the detector was shown to produce comparable results, within 6% of the maximum value for each step, to those demonstrated from pulse mode operation. This suggests that current mode may offer a simple alternative to pulse mode for applications where examining individual pulses is not necessary. Current mode is inappropriate for applications where the height, or shape, of individual pulses is used to determine properties such as the energy deposited or the type of interaction. The current mode configuration was then exposed to a high intensity photon flux from a 63kV X-ray source. Clear response curves were produced that could be used to determine the direction of the source using the same method as that used in pulse mode. This demonstrated that a RadICAL detector can be used for locating high activity sources that may cause dead time problems for a pulse counting detector.

6.1.3 The RadICAL Stack Detector

Prior to the design and build of the RadICAL Stack detector the SRC fitting code was developed and evaluated using modelled data. This suggested that a 4 element stack, with each element separated by 30° could be used to determine the direction of a source to the required accuracy.

Standard Response Curves obtained from the RadICAL Stack detector elements demonstrated similar shapes to those produced by the original RadICAL detectors. The RadICAL Stack demonstrated less uniform SRC's than those produced by the RadICAL detectors. This was due to attenuation of the incident gammas as they pass through the detector casing. The count rate of each detector element was different due to differences in detection efficiency. When normalised the SRC from each detector element follows the same overall shape.

The stack elements produced slightly different undiscriminated SRC shapes when exposed to each isotope. For each element the ratio of maximum to minimum counts decreasing as the average event energy increases. When normalised between a maximum and minimum value these SRCs closely match.

Effective Pulse Shape Discrimination was demonstrated using the stack elements. Significant overlap was observed between gamma and neutron plumes, particularly at energies below approximately 200 keV. It was not possible to discriminate conclusively between events in this region but falsely identified neutrons can be minimized by applying an appropriate discrimination threshold at each energy.

When the PSD technique was used to produce separate discriminated gamma and neutron SRCs a clear difference in curve shape can be seen. The ratio of maximum and minimum count rates for the neutron only events is $1.96 \pm 0.03 : 1$ as opposed to the equivalent ratio of $1.43 \pm 0.01 : 1$ for the gamma only events. These data are based on 50,000 maximum detected counts per step from a $^{241}AmBe$ source with a 1 sigma separation applied, as described in Section 5.3.3.

Further tests showed that it was possible to pick out a neutron only SRC from a high flux, distributed, gamma background.

By exposing the detector to monoenergetic neutrons from a Van der Graaf accelerator it was possible to gain a better understanding of the detectors response to neutrons and generate neutron only SRCs for direct comparison with the discriminated data.

The curve fitting method developed for use with the RadICAL Stack was demonstrated to be an effective method for determining the direction of a 1.76 MBq ^{137}Cs source to within $4.4 \pm 0.3^{\circ}$ at distances of 1.52-2.10m using gamma events. When combined with pulse shape discrimination techniques it was possible to locate a source using gamma and neutron only events separately. The detector has been used to locate a 150 MBq ^{252}Cf source at distances of 1.02-4.02m to within $2.95 \pm 0.32^{\circ}$ using neutron only events and to within $3.90 \pm 0.32^{\circ}$ using combined gamma and neutron events.

6.2 Predicted Performance and Discussion

6.2.1 The RadICAL Detector

The RadICAL detector system was demonstrated to be an effective method of source localisation. Precise measures of accuracy, precision and energy resolution depend on a number of different factors. These include:

- The material and geometry of the detector.
- The location, activity and energy of the source being detected.
- The acquisition time.

Potential benefits offered by this detection system involve its reduced size and weight, compared to heavier collimated systems and the potential to build similar systems for a low cost, compared to other directional detectors. A further benefit is the 360° field of view around which a source can be detected.

A major drawback of this detector, compared to other imaging detectors, is that it has only been shown to determine the direction of limited numbers of simple point sources and has not been shown to be capable of imaging complex distributions of sources. A further drawback of the detector is that, when operated over a 360° field of view, the source direction is determined to be in a single plane that passes through the central axis of the detector. As a result it is not possible to determine which side of the detector on which a source sits without making changes to the current design.

Due to safety and security concerns associated with determining the position of a radioactive source at a distance within a busy lab there was limited time available for taking the range of data required to produce a clear picture of the accuracy and

precision of each of the detectors. This was particularly true of the data taken using the 500MBq Cs137 source as described in Chapter 3.2.7 and the two dimensional source location described in Chapter 3.2.8.

6.2.2 RadICAL Stack Detector

The RadICAL stack curve fitting method was demonstrated to offer an effective alternative to the RadICAL detection method. The method has been demonstrated to be effective with as few as three detector elements with improved performance observed as the number elements increases. As with the RadICAL detector specific measures of accuracy and precision depend on a number of different factors. These include:

- The material and geometry of each detector element.
- The number of detector elements.
- The angular offset of each detector.
- The field of view required.
- The location, activity and energy of the source being detected.
- The acquisition time.

This method of source localisation offers many of the same benefits offered by the RadICAL detector. By removing the need for the detector to rotate a further range of benefits were introduced. These include:

- The ability to localize the source of a rapidly changing flux - such as those encountered in active interrogation.
- The ability to directly couple the scintillator to the photodetector. This improves light collection and removes any degradation in the pulse shape that can potentially cause problems with PSD techniques.
- No need for moving parts that may cause problems with the reliability of the detector.

The RadICAL Stack was also used to successfully localise a neutron source. By using Pulse Shape Discrimination techniques it was possible to separate neutron and

gamma events from a mixed field. The geometry required for the imaging technique did not cause significant degradation in the PSD performance of the detector.

The localisation was less accurate and precise than the RadICAL concept but scope remains for considerable improvement. An improvement in performance may be observed with a greater number of detector elements, improved coupling between each scintillator slab and its photodetector, a case that provides rotationally symmetrical levels of attenuation and improvements to the fitting method.

A significant factor to be considered is the energy dependence of the SRCs. The shape of an SRC changes with the energy of incident event, as described in Chapter 2.1.2, in a manner which may be detrimental to the source localisation technique. All localisations detailed in this report have involved a known source energy but this should be investigated further.

6.3 Future Work

The prototype described in this thesis offers a design that could potentially be used for localising neutron events within mixed field environments. To develop a more effective design a number of issues should be addressed.

6.3.1 Energy Dependence of SRC Shape

The modelling described in Chapter 2.1.2 describes how the shape of a Standard Response Curve is dependent on the energy of incident events. For the detector to be effective when detecting a source of unknown energy it may be necessary to investigate a number of different methods of addressing this problem:

- Determine the energy of each event and chose an appropriate SRC. A range of calibration SRCs can be recorded for each different energy. The energy of the events can then be used to pick the appropriate SRC for curve fitting. This is more likely to be effective with high energy resolution detectors but can be investigated with a wide range of different scintillators, including the EJ299-33 used for Pulse Shape Discrimination.

- Introduce an additional energy resolving detector. If the energy resolution of the stack detectors proves insufficient for picking an appropriate SRC a further, energy resolving, detector could be introduced. This could be used to precisely

determine the appropriate SRC for curve fitting. The major drawback of this method is that it would be inappropriate for picking out neutron only events from a mixed field unless it also possessed PSD properties.

- Increase the size of each detector element - By increasing the size of the detector it is possible to increase the proportion of events that are completely stopped in the scintillator. As the size of the detector is increased the energy above which all events are detected is increased. Below this energy the shape of the SRC doesn't change. This technique is impractical above certain energies due to the size of detector required.

6.3.2 Gating System for High Flux Environments

The original aim of this collaborative project was to combine the directional detector system with a gating system to protect the detector during the high flux phase of an active interrogation pulse. The gating system was developed by Lancaster University. A further stage for this project would be to combine the two systems.

Appendix A

Curve Fitting Code for Source Localisation in MATLAB

A.1 Curve Fitting Code Using Single Detector

Chapter 4.1.1 describes the method used for determining the direction of a source using a limited number of acquisitions from a single detector. Sections of MATLAB code were specially designed to achieve the least-square fit required for this method. An example of this code, written for 4 detector elements and separated by 45°, is detailed below.

```
% Input counts for each detector element. These counts are then
normalised between 0 and 1 so that they can be plotted directly
on top of the SRC. The meanMax and SRCRatio have be determined
experimentally from SRCs.

allCA = [D1CA D2CA D3CA D4CA];
meanMax = 0.8764;
SRCRatio = 0.6918031018;
maxCA = max(allCA);
minCA = maxCA*SRCRatio;
NormCA = meanMax*(allCA-minCA)/(maxCA-minCA);
D1CB = NormCA(1,1);
D2CB = NormCA(1,2);
```

```
D3CB = NormCA(1,3);
D4CB = NormCA(1,4);

% Open the SRC and plot each normalised count rate directly on
top at the appropriate angular separation.

load SRCmean.mat;
srcx = [0:1:180];

for X = 1:181;
D4X = X; %adjust for angular offset of each detector
D3X = X + 30;
D2X = X + 60;
D1X = X + 90;
if D1X > 180;
D1X = D1X - 180;
end
if D2X > 180;
D2X = D2X - 180;
end
if D3X > 180;
D3X = D3X - 180;
end
if D4X > 180;
D4X = D4X - 180;
end

%Find minimum distance between detected point and each SRC point.

for x = 1:181;
dist1=[D1X/180,D1CB; (srcx(1, x))/180,SRCmean(1,x)];
d1=pdist(dist1,'euclidean');
```

```
dist2=[D2X/180,D2CB; (srcx(1, x))/180,SRCmean(1,x)];
d2=pdist(dist2,'euclidean');
dist3=[D3X/180,D3CB; (srcx(1, x))/180,SRCmean(1,x)];
d3=pdist(dist3,'euclidean');
dist4=[D4X/180,D4CB; (srcx(1, x))/180,SRCmean(1,x)];
d4=pdist(dist4,'euclidean');
point1(x,:)= d1;
point2(x,:)= d2;
point3(x,:)= d3;
point4(x,:)= d4;
end

p1m = min(point1);
p2m = min(point2);
p3m = min(point3);
p4m = min(point4);

%Find angle of detectors that correspond to closest fit.

least(X,:)=(p1m^2)+(p2m^2)+(p3m^2)+(p4m^2);
end
minls = min(least);
angle = find(least==minls);
plot(srcx, SRCmean); %Plot SRC
hold;
dx1 = plot(D1X+angle, D1CB, 'ko'); %plot detected points over SRC
dx2 = plot(D2X+angle, D2CB, 'ko');
dx3 = plot(D3X+angle, D3CB, 'ko');
dx4 = plot(D4X+angle, D4CB, 'ko');
angle; % Output angle of best fit.
```

For the stationary detector stack a similar code to that described in Appendix A1

was developed. The major difference was that each count rate was multiplied by an additional figure. This figure corresponded to the efficiency of each respective detector and was determined experimentally.

A.2 PSD Event Sorting

Chapter 5.3.2 describes how the discrimination level was set for each detector. This was done by processing data from the CAEN digitiser. This data was output with each row representing a different event and columns 1-3 representing a time stamp, pulse height that corresponds to the energy of the event and a PSD number respectively. This data was then used to generate a discrimination level using the code below.

```
%removes all events with PSD <0 or >1
idx=(Data(:,3)>0);
Data=Data(idx,:);
idx=(Data(:,3)<0.999);
Data=Data(idx,:);

%saves mode PSD value for each energy
Energy=unique(Data(:,2));
x=0:0.005:0.5;
for i = 1:length(Energy);
    %Logs mode PSD value for each energy
        H=hist(Data(Data(:,2)==Energy(i),3),x);
        [num idx] =  max (H);
        x_above= x(H> (max(H)/2));
        if length(x_above) > 1
        fwhm= x_above(end)- x_above(1);
        %Y = 3 columns are max energy counts, corresponding
         energy bin and FWHM of peak
        Y(i,1:3) = [num (idx*0.005) fwhm];
        else
        Y(i,1:3) = [num (idx*0.005) 0];
```

```
end

%Discrimination level is determined by adding desired multiple of
FWHM to the mode PSD value for each energy.  Sigma discrimination
shown.

Discrimation = Y(:,2) + Y(:,3)/2.3548;
```

Bibliography

[1] George Randall. *'RadICAL' - A New Concept in Detector Development*. Msc project report, University College London, 2011.

[2] Dennis R. Slaughter, Mark R. Accatino, Adam Bernstein, Arden D. Dougan, James M. Hall, Alex Loshak, Doug R. Manatt, Bert a. Pohl, Rosemary S. Walling, Dave L. Weirup, and Staney G. Prussin. The "nuclear car wash": A scanner to detect illicit special nuclear material in cargo containers. *IEEE Sensors Journal*, 5(4):560–564, 2005.

[3] E. R. Siciliano, J. H. Ely, R. T. Kouzes, B. D. Milbrath, J. E. Schweppe, and D. C. Stromswold. Comparison of PVT and NaI(Tl) scintillators for vehicle portal monitor applications. *Nuclear Instruments and Methods in Physics Research, Section A: Accelerators, Spectrometers, Detectors and Associated Equipment*, 550(3):647–674, 2005.

[4] Dennis Slaughter, Mark Accatino, and a Bernstein. Detection of special nuclear material in cargo containers using neutron interrogation. *Lawrence Livermore National Laboratory*, August 2003.

[5] Robert C. Runkle, David L. Chichester, and Scott J. Thompson. Rattling nucleons: New developments in active interrogation of special nuclear material. *Nuclear Instruments and Methods in Physics Research, Section A: Accelerators, Spectrometers, Detectors and Associated Equipment*, 663(1):75–95, 2012.

[6] Natalia Zaitseva, Benjamin L. Rupert, Iwona Paweczak, Andrew Glenn, H. Paul Martinez, Leslie Carman, Michelle Faust, Nerine Cherepy, and Stephen Payne. Plastic scintillators with efficient neutron/gamma pulse shape discrimination.

Nuclear Instruments and Methods in Physics Research, Section A: Accelerators, Spectrometers, Detectors and Associated Equipment, 668:88–93, 2012.

[7] D. Schriefer. *Safeguards, security, safety and the nuclear fuel cycle*. Woodhead Publishing Limited, 2012.

[8] United States Nuclear Regulatory Commision. Nuclear Materials, 2015.

[9] US Nuclear Regulstory Commission. Nuclear Regulatory Legislation 112th Congress ; 2nd Session. 1(10), 2013.

[10] IAEA. *SAFEGUARDS 2001 Edition*. Number 3. 2001.

[11] Joseph P Indusi and Jonathan B Sanborn. Nuclear Safeguards. *Encyclopedia of Physical Science and Technology (Third Edition)*.

[12] World Nuclear Association. Plutonium, 2016.

[13] Charles Meade and Roger C. Molander. CENTER FOR TERRORISM For More Information. *Risk Management*, 2006.

[14] George A. Alexander. *Dirty Bomb (Radiological Dispersal Device)*. Elsevier Inc., 2 edition, 2016.

[15] M.I. Ojovan. Naturally Occurring Radionuclides. pages 31–39, 2014.

[16] Ian Hore-Lacy. *Uranium for nuclear power*. Elsevier Ltd, 2016.

[17] Key Lake, Rabbit Lake, Mcarthur River, and Cigar Lake. The Front End of the Nuclear Fuel Cycle. pages 1–14, 1972.

[18] IAEA. Nuclear Fuel Cycle Information System, 2012.

[19] Arjun Makhijani and D Ph. Just Plain Facts to Fuel an Informed Debate on Nuclear Proliferation and Nuclear Power. (October), 2004.

[20] H M Sapolsky. Nuclear weapons. *Lancet*, 1(8380):796, 1984.

[21] D Greneche and M Chhor. *Development of the thorium fuel cycle*. Woodhead Publishing Limited, 2012.

[22] O. J. Wick. *Plutonium handbook. A guide to Technology. Vol. 1*. The American Nuclear Society, 1980.

[23] H.S. Kamath and D.S.C. Purushotham. Encyclopedia of Materials: Science and Technology. *Encyclopedia of Materials: Science and Technology*, pages 5687–5689, 2001.

[24] United States General Accounting Office. Nuclear nonproliferation U.S. efforts to help other countries combat nuclear smuggling need strengthened coordination and planning. (May), 2002.

[25] World Nuclear Association. Uranium Enrichment, 2016.

[26] Serena Albright, David; Kelleher-Vergantini. Military Highly Enriched Uranium and Plutonium Stocks in Acknowledged Nuclear Weapon States. *Institute for Science and International Security*, 2015.

[27] Serena Albright, David; Kelleher-Vergantini. Civil HEU Watch - Tracking Inventories of Civil Highly Enriched Uranium. *Institute for Science and International Security*, (August), 2015.

[28] International Atomic Energy Agency and V Authors. Thorium fuel cyclePotential benefits and challenges. *IAEATECDOC-1450, International Atomic Energy* . . . , (May):113, 2005.

[29] Robert Alvarez. Managing the Uranium-233 Stockpile of the United States, 2012.

[30] Daniel Albright, David; Kelleher-Vergantini, Serena; Schnur. Civil Plutonium Stocks Worldwide. *Institute for Science and International Security*, 2003(updated 2005):1–23, 2015.

[31] IAEA. Iaea Incident and Trafficking Database (Itdb). 2015.

[32] R.T. Kouzes. Detecting Illicit Nuclear Materials. *American Scientist*, 93(5):422–427, 2005.

[33] IAEA. Promoting Nuclear Security : What the IAEA is doing. 2006.

[34] National Nuclear Security Administration. Megaports Initiative. 2010.

[35] Richard T. Kouzes. Challenges for interdiction of nuclear threats at borders. *ANIMMA 2009 - 2009 1st International Conference on Advancements in Nuclear Instrumentation, Measurement Methods and their Applications*, pages 5–7, 2009.

[36] Richard T. Kouzes, Edward R. Siciliano, James H. Ely, Paul E. Keller, and Ronald J. McConn. Passive neutron detection for interdiction of nuclear material at borders. *Nuclear Instruments and Methods in Physics Research, Section A: Accelerators, Spectrometers, Detectors and Associated Equipment*, 584(2-3):383–400, 2008.

[37] R.T. Kouzes. American Scientist. *American Scientist*, 93(5):422–427, 2003.

[38] G.F. Knoll. *Radiation Detection and Measurements*. John Wiley and Sons Inc., 3rd edition, 2000.

[39] Richard T. Kouzes, James H. Ely, Luke E. Erikson, Warnick J. Kernan, Azaree T. Lintereur, Edward R. Siciliano, Daniel L. Stephens, David C. Stromswold, Renee M. Van Ginhoven, and Mitchell L. Woodring. Neutron detection alternatives to 3He for national security applications. *Nuclear Instruments and Methods in Physics Research, Section A: Accelerators, Spectrometers, Detectors and Associated Equipment*, 623(3):1035–1045, 2010.

[40] Konstantin N. Borozdin, Gary E. Hogan, Christopher Morris, William C. Priedhorsky, Alexander Saunders, Larry J. Schultz, and Margaret E. Teasdale. Surveillance: Radiographic imaging with cosmic-ray muons. *Nature*, 422(March):277, 2003.

[41] Elena Guardincerri, Jeffrey Bacon, Konstantin Borozdin, J. Matthew Durham, Joseph Fabritius, Adam Hecht, Edward C. Milner, Haruo Miyadera, Christopher L. Morris, John Perry, and Daniel Poulson. Detecting special nuclear material using muon-induced neutron emission. *Nuclear Instruments and Methods in Physics Research, Section A: Accelerators, Spectrometers, Detectors and Associated Equipment*, 789:109–113, 2015.

[42] Tsahi Gozani. Fission signatures for nuclear material detection. *IEEE Transactions on Nuclear Science*, 56(3):736–741, 2009.

[43] D. R. Slaughter, M. R. Accatino, a. Bernstein, J. a. Church, M. a. Descalle, T. B. Gosnell, J. M. Hall, a. Loshak, D. R. Manatt, G. J. Mauger, T. L. Moore, E. B. Norman, B. a. Pohl, J. a. Pruet, D. C. Petersen, R. S. Walling, D. L. Weirup, S. G. Prussin, and M. McDowell. Preliminary results utilizing high-energy fission product γ-rays to detect fissionable material in cargo. *Nuclear Instruments and Methods in Physics Research, Section B: Beam Interactions with Materials and Atoms*, 241(1-4):777–781, 2005.

[44] C. Hill, et. al,. Active detection of special nuclear material - Recommendations for interrogation source approach for UK prototype active detection system. *IEEE Nuclear Science Symposium Conference Record*, pages 732–737, 2012.

[45] C. Hill, et. al,. Photofission for Active SNM Detection I : Intense pulsed 8Me V Bremsstrahlung Source. pages 1424–1429, 2012.

[46] P. Mistry, et. al,. Photofission for active SNM detection II: Intense pulsed 19F(p,$\alpha\gamma$)16O characteristic γ source. *IEEE Nuclear Science Symposium Conference Record*, pages 24–31, 2012.

[47] C. Clemett, et. al,. Neutrons for active detection of special nuclear material : an intense pulsed 7 Li (p , n) 7 Be source. pages 44–50, 2012.

[48] Thomas M. Miller, Bruce W. Patton, Brandon R. Grogan, James J. Henkel, Brian D. Murphy, Jeffrey O. Johnson, and John T. Mihalczo. Investigations of active interrogation techniques to detect special nuclear material in maritime environments: Standoff interrogation of small- and medium-sized cargo ships. *Nuclear Instruments and Methods in Physics Research, Section B: Beam Interactions with Materials and Atoms*, 316:94–104, 2013.

[49] Brandon R. Grogan, James J. Henkel, Jeffrey O. Johnson, John T. Mihalczo, Thomas M. Miller, and Bruce W. Patton. Investigation of active interrogation techniques to detect special nuclear material in maritime environments: Boarded

search of a cargo container ship. *Nuclear Instruments and Methods in Physics Research, Section B: Beam Interactions with Materials and Atoms*, 316:62–70, 2013.

[50] C. E. Moss. Linear Accelerator-Based Active Interrogation For Detection of Highly Enriched Uranium. *AIP Conference Proceedings*, 680(1):900–904, 2003.

[51] Daniel H. Morse, Arlyn J. Antolak, and Barney L. Doyle. Photofission in uranium by nuclear reaction gamma-rays. *Nuclear Instruments and Methods in Physics Research, Section B: Beam Interactions with Materials and Atoms*, 261(1-2 SPEC. ISS.):378–381, 2007.

[52] C. Moss, et. al,. Comparison of active interrogation techniques. *IEEE Nuclear Science Symposium Conference Record*, 1(4):329–332, 2005.

[53] Areg Danagoulian, William Bertozzi, Curtis L. Hicks, Alexei V. Klimenko, Stephen E. Korbly, Robert J. Ledoux, and Cody M. Wilson. Prompt neutrons from photofission and its use in homeland security applications. *2010 IEEE International Conference on Technologies for Homeland Security, HST 2010*, pages 379–384, 2010.

[54] E. T E Reedy, S. J. Thompson, and A. W. Hunt. The detection of delayed ??-rays between intense bremsstrahlung pulses for discriminating fissionable from non-fissionable materials. *Nuclear Instruments and Methods in Physics Research, Section A: Accelerators, Spectrometers, Detectors and Associated Equipment*, 606(3):811–815, 2009.

[55] a. Fessler, T. N. Massey, B. J. Micklich, and D. L. Smith. Thick target photon yields and angular distributions for the 19F(p,γ)16O source reaction at incident proton energies between 1.5 and 4.0 MeV. *Nuclear Instruments and Methods in Physics Research, Section A: Accelerators, Spectrometers, Detectors and Associated Equipment*, 450(2):353–359, 2000.

[56] B. J. Micklich, D. L. Smith, T. N. Massey, C. L. Fink, and D. Ingram. Measurement of thick-target high-energy γ-ray yields from the 19F(p,γ)16O reaction.

Nuclear Instruments and Methods in Physics Research, Section A: Accelerators, Spectrometers, Detectors and Associated Equipment, 505(1-2):1–4, 2003.

[57] Brandon Blackburn, James Jones, Scott Watson, James Johnson, David Gerts, Cal Moss, Laurie Waters, Kiril Ianakiev, John Mihalczo, Paul Hausladen, Sara Pozzi, Marek Fiaska, Shaun Clarke, Alan Hunt, Scott Thompson, and Matt Kinlaw. Detection of special nuclear material by means of promptly emitted radiation following photonuclear stimulation. *IEEE Nuclear Science Symposium Conference Record*, 1:192–198, 2007.

[58] László Lakosi and Cong Tam Nguyen. Neutron interrogation of high-enriched uranium by a 4 MeV linac. *Nuclear Instruments and Methods in Physics Research, Section B: Beam Interactions with Materials and Atoms*, 266(14):3295–3301, 2008.

[59] V.L Chakhlov, Z.W Bell, V.M Golovkov, and M.M Shtein. Photoneutron source based on a compact 10MeV betatron. *Nuclear Instruments and Methods in Physics Research Section A: Accelerators, Spectrometers, Detectors and Associated Equipment*, 422(1-3):5–9, 1999.

[60] F.A. Smith. *A Primer in Applied Radiation Physics*. World Scientific Publishing, 1st edition, 2000.

[61] Dan Dietrich, Chris Hagmann, Phil Kerr, Les Nakae, Mark Rowland, Neal Snyderman, Wolfgang Stoeffl, and Robert Hamm. A kinematically beamed, low energy pulsed neutron source for active interrogation. *Nuclear Instruments and Methods in Physics Research, Section B: Beam Interactions with Materials and Atoms*, 241(1-4):826–830, 2005.

[62] E H Chichester, D L; Seabury. Active Neutron Interrogation to Detect Shielded Fissionable Material. *International Topical Meeting on Nuclear Research Applications and Utilization of Accelerators*, pages 1–9, 2009.

[63] B W Blackburn, J L Jones, C E Moss, J T Mihalczo, A W Hunt, F Harmon, S M Watson, and J T Johnson. Utilization of Actively Induced, Prompt Radi-

ation Emission for Nonproliferation Applications. *Conference on Accelerator Applications in Research and Industry*, 2006.

[64] G L Randall, E Iglesis, H F Wong, and R S Speller. A method of providing directionality for ionising radiation detectors RadICAL. *Journal of Instrumentation*, 9(10):P10011–P10011, 2014.

[65] F.H. Attix. *Introduction to Radiological Physics and Radiation Dosimetry*. 1986.

[66] F.D. Brooks. Development of organic scintillators. *Nuclear Instruments and Methods*, 162(1-3):477–505, 1979.

[67] L.M. Bollinger and G.E. Thomas. Measurement of the Time Dependence of Scintillation Intensity by a Delayed-Coincidence Method. *Review of Scientific Instruments*, 32(9):1044–1050, 1961.

[68] S. a. Pozzi, M. M. Bourne, and S. D. Clarke. Pulse shape discrimination in the plastic scintillator EJ-299-33. *Nuclear Instruments and Methods in Physics Research, Section A: Accelerators, Spectrometers, Detectors and Associated Equipment*, 723:19–23, 2013.

[69] N.P. Hawkes and G.C. Taylor. Analysis of the pulse shape mechanism in a plastic scintillator with efficient neutron/gamma pulse shape discrimination. *Nuclear Instruments and Methods in Physics Research Section A: Accelerators, Spectrometers, Detectors and Associated Equipment*, 729:522–526, November 2013.

[70] Ashley Richard Jones and Malcolm Joyce. *Pulse-shape discrimination in organic scintillators using the rising edge*, pages 1–3. IEEE, 2013. IEEE Advancements in Nuclear instrumentation, Measurement Methods and Analysis, Marseille, June 2013.

[71] National Institute for Science and Technology. X-Ray Mass Attenuation Coefficients.

[72] P Rinard. Neutron interactions with matter. *Passive Nondestructive Assay of Nuclear Materials, Los Alamos Technical Report NUREG/CR-5550, LA-UR-90-732*, pages 357–377, 1991.

[73] Richard S. Woolf, Anthony L. Hutcheson, Chul Gwon, Bernard F. Phlips, and Eric a. Wulf. Comparing the response of PSD-capable plastic scintillator to standard liquid scintillator. *Nuclear Instruments and Methods in Physics Research Section A: Accelerators, Spectrometers, Detectors and Associated Equipment*, 784:80–87, 2014.

[74] William R. Leo. *Techniques for nuclear and particle physics experiments : a how-to approach*. Springer, 2 edition, 1994.

[75] P. Buzhan, B. Dolgoshein, L. Filatov, a. Ilyin, V. Kantzerov, V. Kaplin, a. Karakash, F. Kayumov, S. Klemin, E. Popova, and S. Smirnov. Silicon photomultiplier and its possible applications. *Nuclear Instruments and Methods in Physics Research, Section A: Accelerators, Spectrometers, Detectors and Associated Equipment*, 504(1-3):48–52, 2003.

[76] H.O. Anger. A New Instrument for Mapping Gamma-Ray Emitters. *Biology and Medicine Quarterly Report*, 1957.

[77] W.R. Hendee and E.R. Ritenour. *Medical Imaging Physics*. Wiley-Blackwall, 4th edition, 2002.

[78] R.A. Powsner and E.R. Powsner. *Essential Nuclear Medicine Physics*. Wiley-Blackwall, 2nd edition, 2006.

[79] R. W. Todd, J. M. Nightingale, and D. B. Everett. A proposed γ camera. *Nature*, 251(5471):132–134, 1974.

[80] Gary W. Phillips. Gamma-ray imaging with Compton cameras. *Nuclear Instruments and Methods in Physics Research Section B: Beam Interactions with Materials and Atoms*, 99(1-4):674–677, 1995.

[81] Commission Recommendation of 8 June 2000, 2000.

[82] a. Baeza, J. a. del Puerto, M. del Rio, C. Miro, F. Ortiz, and M. Paniagua. Development and operativity of a real-time radiological monitoring network centred on the nuclear power plant of Almaraz (Spain). *IEEE Transactions on Nuclear Science*, 40(6 pt 2):2014–2020, 1993.

[83] Y. Shirakawa. Development of a direction finding gamma-ray detector. *Nuclear Instruments and Methods in Physics Research, Section B: Beam Interactions with Materials and Atoms*, 263(1 SPEC. ISS.):58–62, October 2007.

[84] Yoshiyuki Shirakawa, Toshiya Yamano, and Yusuke Kobayashi. Remote sensing of nuclear accidents using a direction finding detector. *IECON Proceedings (Industrial Electronics Conference)*, pages 1917–1922, 2009.

[85] O Gal, F Jean, F Laink, C Lkvcque, Cea-technologies Avancces, Yvette Cedex, Eurisys Mesures, Cogema Group, Division Systemes, and Bretonneux Cedex. The CARTOGAM Portable Gamma Imaging. 00(c):725–729, 2000.

[86] J.T. Santo, M. Maul, R. Lucero, M. Clapham, and B. Battle. Application of remote gamma imaging surveys at the turkey point PWR reactor facility, 2006.

[87] Serkan Akkoyun. A method for determination of gamma-ray direction in space. *Acta Astronautica*, 87:147–152, 2013.

[88] Hubbell J.H. Seltzer S.M. Chang J. Coursey J.S. Sukumar R. Zucker D.S. Berger, M.J. and K. Olsen. XCOM: Photon Cross Section Database (version 1.5), 2010.

[89] Eljen. EJ-200 GAMMA ATTENUATION COEFFICIENTS.

[90] Mark Ellis, Carlo Tintori, Paul Schotanus, Kirk Duroe, Paul a. Kendall, and Giuliano Mini. The effect of detector geometry on EJ-309 pulse shape discrimination performance. *IEEE Nuclear Science Symposium Conference Record*, 2013.

[91] S. Agostinelli, et. al,. GEANT4 - A simulation toolkit. *Nuclear Instruments and Methods in Physics Research, Section A: Accelerators, Spectrometers, Detectors and Associated Equipment*, 506(3):250–303, 2003.

[92] Zachary S. Hartwig and Peter Gumplinger. Simulating response functions and pulse shape discrimination for organic scintillation detectors with Geant4. *Nuclear Instruments and Methods in Physics Research, Section A: Accelerators, Spectrometers, Detectors and Associated Equipment*, 737:155–162, 2014.

[93] S. Webb. *The Physics of Medical Imaging*. IOP Publishing Ltd, 1st edition, 1988.

[94] Electron Tubes. 9531 PMT Data Sheet.

[95] Saint-Gobain. CsI(Na) Sodium activated Cesium Iodide Data Sheet, 2016.

[96] James A. Yang, Pin; Harmon, Charles D.; Doty, F. Patrick; Ohlhausen. Effect of Humidity on Scintillation Performance in Na and Tl Activated CsI Crystals. *IEEE Transactions on Nuclear Science*, 2014.

[97] J.T. Bushberg, J.A. Seibert, Leidholdt E.M., and J.M. Boone. *The Essential Physics of Medical Imaging*. Lippincott, Williams and Wilkins, 3rd edition, 2012.

[98] CAEN. Technical Information Manual. *Memory*, (July):1–36, 2010.

[99] Sue Cooke. Electronic instrumentation. *Electronic Systems News*, 1986(2):32, 1986.

[100] CAEN. V1718 Information. (June), 2009.

[101] CAEN. VME8004 Mini Crate. (January 2015), 2015.

[102] Newport Instruments. ESP301 Integrated 3-Axis Motion Controller/Driver. (July), 2010.

[103] Joseph Glaser, Taner Uckan, Jose March-Leuba, Danny Powell, and James D. White. AmBe Sealed Neutron Source Assessment Studies for the Fissile Mass Flow Monitor. (July), 2003.